



**PAF1c drives MYC-mediated immune evasion in pancreatic ductal
adenocarcinoma**

**PAF1c treibt die MYC-vermittelte Immunevasion im duktalem
Adenokarzinom der Bauchspeicheldrüse an**

Doctoral thesis for a doctoral degree
at the Graduate School of Life Sciences,
Julius-Maximilians-Universität Würzburg,
Section: Biomedicine

submitted by

Abdallah Hatem Hassan Hosny Ahmed Gaballa

From Sharkia, Egypt

Würzburg 2023

Submitted on: 02.10.2023

Members of the Thesis Committee

Chairperson: Prof. Dr. Alexander Buchberger

Primary Supervisor: Prof. Dr. Martin Eilers

Supervisor (Second): Prof. Dr. Stefan Gaubatz

Supervisor (Third): Prof. Dr. Martin Sos

Date of Public Defense:

Date of Receipt of Certificates:

Table of Contents

Summary	7
Zusammenfassung	8
1 Introduction	10
1.1 Tumor immunosurveillance	10
1.2 Transcription-replication conflicts (TRCs).....	12
1.2.1 Types of TRCs	12
1.2.2 Mechanisms for limiting TRCs or their subsequent genomic instability	13
1.2.3 MYC and transcription-replication coordination	13
1.3 MYC oncoproteins	14
1.3.1 Structure and canonical function of MYC	15
1.3.2 Models of MYC function	16
1.3.3 MYC multimerization	17
1.4 PAF1c and MYC	17
1.5 MYC as a regulator of immune evasion.....	19
1.6 Aim of the thesis	20
2 Materials.....	22
2.1 Bacterial strains and cell lines.....	22
2.1.1 Bacterial strains	22
2.1.2 Mammalian Cell lines.....	22
2.2 Cultivation media and supplements	22
2.2.1 Media and antibiotics for bacterial culture.....	22
2.2.2 Cultivation media for cell culture.....	23
2.2.3 Compound used for cell culture.....	23
2.3 Antibodies.....	24
2.3.1 Primary antibodies.....	24
2.3.2 Secondary antibodies.....	26
2.4 Nucleic acids.....	27

2.4.1	shRNAs	27
2.4.2	Primers.....	28
2.4.3	Plasmids	30
2.5	Solutions and buffers.....	30
2.6	Enzymes, standards and kits	34
2.6.1	Enzymes	34
2.6.2	Standards	35
2.6.3	Kits	35
2.7	Consumables	36
2.8	Software.....	37
2.9	Equipment.....	38
3	Methods.....	40
3.1	Cell culture methods	40
3.1.1	Cell cultivation, splitting, freezing and thawing.....	40
3.1.2	Lentiviral Infection	41
3.1.3	siRNA transfection	41
3.2	Cell biology methods	42
3.2.1	Immunofluorescence staining.....	42
3.2.2	Proximity ligation assay	42
3.2.3	Live cell imaging.....	43
3.2.4	siRNA screen	43
3.3	Molecular and biochemical methods	44
3.3.1	Chromatin immunoprecipitation (ChIP).....	44
3.3.2	RNA extraction and cDNA synthesis	45
3.3.3	Real-time quantitative PCR (RT-qPCR)	46
3.3.4	Preparation of whole cell lysate and determination of protein concentration	47
3.3.5	Immunoblotting	47
3.3.6	Transformation of competent bacteria with DNA plasmid.....	48
3.3.7	Bacterial plasmid DNA preparation for analysis (miniprep)	48
3.3.8	Plasmid DNA Isolation (Maxiprep)	48
3.4	Next generation sequencing methods	49

3.4.1	ChIP-sequencing	49
3.4.2	CUT&RUN-sequencing	49
3.4.3	mRNA-sequencing.....	50
3.4.4	BLISS.....	50
3.4.5	4sU sequencing	52
3.5	Bioinformatics	53
3.6	Immunohistochemistry	54
4	Results	56
4.1	MYC prevents transcription-replication conflicts in PDAC cells	56
4.1.1	MYC is required for genomic stability during S-phase	56
4.1.2	MYC prevents transcription-replication conflicts	57
4.2	An siRNA screen identifies the PAF1c as a regulator of genomic stability	60
4.2.1	Target selection strategy for the siRNA library.	60
4.2.2	Set-up of the siRNA screen	61
4.2.3	Hits of the siRNA screen.....	62
4.2.4	PAF1c maintains genomic stability during replication stress.....	64
4.3	PAF1c is a downstream factor of MYC but is largely dispensable for the regulation of MYC target genes.....	66
4.3.1	siRNA screen targeting factors downstream of PAF1c	66
4.3.2	MYC-dependent recruitment of CTR9 to the RNAPII is largely dispensable for the regulation of MYC target genes	67
4.4	PAF1c is required for the transcription of long DNA repair genes.....	69
4.4.1	PAF1c-dependent expression of DNA repair genes	69
4.4.2	PAF1c promotes full-length transcription of long genes	70
4.5	PAF1c-dependent sequestration of SPT6 on long genes represses the expression of MHC class I genes.....	73
4.5.1	PAF1c represses the expression of MHC class I genes.....	73
4.5.2	SPT6 binds MHC class I genes after CTR9 depletion	74
4.5.3	SPT6 recruitment to MHC class I genes is required for their expression upon CTR9 depletion	76
4.5.4	SPT6 localization at the transcription end site is gene length dependent and correlates with gene expression upon CTR9 depletion.....	78

4.6	PAF1c-dependent repression of MHC class I genes is conserved in multiple PDAC cell lines	80
4.7	CTR9 is required for PDAC maintenance <i>in vivo</i>	82
4.7.1	CTR9 depletion enables long-term survival of PDAC-bearing mice	82
4.7.2	Survival benefit of CTR9 or MYC depletion is independent of ATR inhibition	84
4.8	PAF1c mediates immune evasion in PDAC	86
4.8.1	CTR9 depletion reshapes the tumor microenvironment	86
4.8.2	CTR9 mediates immune evasion in PDAC	87
5	<i>Discussion</i>	88
5.1	MYC as a regulator of genomic stability	88
5.2	Functions of MYC-dependent PAF1c recruitment to the RNAPII	89
5.3	PAF1c-dependent occupancy of transcription elongation factors	91
5.4	PAF1c: a novel therapeutic target in PDAC	92
5.5	The hard-wired link between genomic stability and immune evasion in cancer	93
5.5.1	Importance of gene-length-dependent transcription in cancer	93
5.5.2	A new model linking genomic stability and immune evasion	94
5.6	Conclusions	95
6	<i>References</i>	97
7	<i>Appendix</i>	108
7.1	Table of figures	108
7.2	Summary of the siRNA screen	110
7.3	Acknowledgement	113
7.4	Publications	114
7.5	Affidavit	115
7.6	Curriculum vitae	116

Summary

The expression of the MYC proto-oncogene is elevated in a large proportion of patients with pancreatic ductal adenocarcinoma (PDAC). Previous findings in PDAC have shown that this increased MYC expression mediates immune evasion and promotes S-phase progression. How these functions are mediated and whether a downstream factor of MYC mediates these functions has remained elusive. Recent studies identifying the MYC interactome revealed a complex network of interaction partners, highlighting the need to identify the oncogenic pathway of MYC in an unbiased manner.

In this work, we have shown that MYC ensures genomic stability during S-phase and prevents transcription-replication conflicts. Depletion of MYC and inhibition of ATR kinase showed a synergistic effect to induce DNA damage. A targeted siRNA screen targeting downstream factors of MYC revealed that PAF1c is required for DNA repair and S-phase progression. Recruitment of PAF1c to RNAPII was shown to be MYC dependent. PAF1c was shown to be largely dispensable for cell proliferation and regulation of MYC target genes.

Depletion of CTR9, a subunit of PAF1c, caused strong tumor regression in a pancreatic ductal adenocarcinoma model, with long-term survival in a subset of mice. This effect was not due to induction of DNA damage, but to restoration of tumor immune surveillance.

Depletion of PAF1c resulted in the release of RNAPII with transcription elongation factors, including SPT6, from the bodies of long genes, promoting full-length transcription of short genes. This resulted in the downregulation of long DNA repair genes and the concomitant upregulation of short genes, including MHC class I genes. These data demonstrate that a balance between long and short gene transcription is essential for tumor progression and that interference with PAF1c levels shifts this balance toward a tumor-suppressive transcriptional program. It also directly links MYC-mediated S-phase progression to immune evasion. Unlike MYC, PAF1c has a stable, known folded structure; therefore, the development of a small molecule targeting PAF1c may disrupt the immune evasive function of MYC while sparing its physiological functions in cellular growth.

Zusammenfassung

Die Expression des MYC-Proto-Onkogens ist bei einem großen Teil der Patienten mit duktalem Adenokarzinom der Bauchspeicheldrüse (PDAC) erhöht. Bisherige Erkenntnisse in der Erforschung des Pankreaskarzinoms zeigen, dass die erhöhte MYC-Expression die Umgehung des Immunsystems bewirkt und die Progression der S-Phase fördert. Wie diese Funktionen vermittelt werden und ob ein nachgeschalteter Faktor von MYC für diese Funktion verantwortlich ist, blieb jedoch bisher ungeklärt. Jüngste Studien zur Identifizierung des MYC-Interaktoms haben ein sehr komplexes Netzwerk an Interaktionspartnern von MYC aufgedeckt, was die Notwendigkeit unterstreicht, die onkogenen Eigenschaften von MYC und seinen Interaktionspartnern unvoreingenommen und genau zu untersuchen.

In dieser Arbeit konnte gezeigt werden, dass MYC die genomische Stabilität während der S-Phase herstellt und Konflikte zwischen Transkription und Replikation verhindert. Die Depletion von MYC und die Hemmung der ATR-Kinase zeigten bei der Induktion von DNA Schäden eine synergistische Wirkung. Ein siRNA-Screen, der Gene beinhaltete, die MYC nachgeschaltet sind, ergab, dass PAF1c für die DNA-Reparatur und die S-Phasen-Progression erforderlich ist. Es zeigte sich außerdem, dass die Rekrutierung von PAF1c an RNAPII von MYC abhängig ist. Für die Zellproliferation und die Regulierung von MYC-Zielgenen ist PAF1c jedoch weitgehend entbehrlich.

Es konnte gezeigt werden, dass die Depletion von CTR9, einer Untereinheit von PAF1c, in einem murinen Modell des duktales Adenokarzinoms der Bauchspeicheldrüse zu einer starken Tumorregression mit langfristigem Überleben einiger Mäuse führte. Diese Wirkung war nicht auf die Induktion von DNA-Schäden zurückzuführen, sondern auf die Wiederherstellung der Immunüberwachung des Tumors.

Die Deletion von PAF1c führte zu einer Umverteilung von RNAPII und Transkriptionselongationsfaktoren wie SPT6, von langen Genen hin zu kurzen Genen. Dadurch wurden lange Gene wie zum Beispiel DNA Reparaturgene nicht vollständig transkribiert, kurze Gene wie MHC-Klasse-I-Gene hingegen schon. Diese Daten zeigen,

dass ein Gleichgewicht zwischen der Transkription langer und kurzer Gene für die Tumorprogression wichtig ist und dass eine Verminderung der PAF1c-Konzentration dieses Gleichgewicht in Richtung eines tumorsuppressiven Transkriptionsprogramms verschiebt. Außerdem besteht ein direkter Zusammenhang zwischen der MYC-vermittelten S-Phasen-Progression und der Umgehung des Immunsystems. Im Gegensatz zu MYC verfügt PAF1c über eine stabile und gut bekannte gefaltete Struktur. Daher könnte die Entwicklung eines kleinen Moleküls, das PAF1c hemmt, die Funktion von MYC zur Umgehung des Immunsystems stören und gleichzeitig seine physiologischen Funktionen für das Zellwachstum nicht beeinträchtigen.

1 Introduction

1.1 Tumor immunosurveillance

Thanks to tumor immunosurveillance, the lifetime risk of developing cancer is only 40% and not more (Dersh *et al*, 2021). Tumor immunosurveillance is a well-characterized process that is dictated by many factors, including: tumor immunogenicity, immune cell infiltration, T cell priming, T cell checkpoints, and the tumor microenvironment (Dersh *et al.*, 2021). Tumor growth is triggered by mutations that activate oncogenes and inactivate tumor suppressor genes. These mutations give tumors a selective advantage in proliferation. However, this comes at the risk of being recognized as a foreign cell by the host immune system.

The role of the anti-tumor immune response has been underestimated for decades due to the ability of tumors to evade the immune response. Upregulation of negative regulatory elements or checkpoints on T cells, such as cytotoxic T lymphocyte protein 4 (CTLA4) or programmed cell death protein 1 (PD-1), is an important mechanism of immune escape (Sharma & Allison, 2015). CTLA4 is a negative regulator of T cell activation that competes with the co-stimulatory CD28 for binding to the common ligands CD80 and CD86 (Chen & Mellman, 2017). PD-1 is a cell surface receptor on T cells that, when bound to its ligand PD-L1, which can be expressed by many cancer cells, generates an inhibitory signal and attenuates T cell activity.

Antigen processing and presentation is another important process in tumor immunosurveillance. The two types of glycoproteins that are associated with antigen presentation are major histocompatibility (MHC) class I and class II molecules, which present peptides to CD8+ and CD4+ T cells, respectively. All nucleated cells express or can be induced to express MHC class I molecules. Peptides resulting from protein turnover are presented on MHC class I molecules and provide a representation of the

Introduction

cell's proteome (Pishesha *et al*, 2022). During their development in the thymus, T cells learn to tolerate these self-peptides presented on MHC molecules. When a T cell encounters an unrecognized presented peptide, as in the case of infection or somatic mutations, it is activated (Pishesha *et al.*, 2022).

Genetic mutations that accumulate in cancer cells lead to the production of neoantigens or tumor-specific antigens that can be presented by MHC class I molecules on tumor cells (Xie *et al*, 2023). Once neoantigens are presented by MHC class I molecules on cancer cells, CD8⁺ T cells can recognize and attack these cells. Thus, during tumorigenesis, cancer cells that are able to downregulate MHC class I gene expression have a selective growth advantage, resulting in a large number of tumors having low levels of MHC class I gene expression (Garrido & Aptsiauri, 2019).

There are several published mechanisms by which cancer cells can downregulate MHC class I gene expression (Dersh *et al.*, 2021). Epigenetic dysregulation is one of the proposed mechanisms with strong evidence (Burr *et al*, 2019; Khan *et al*, 2008; Sun *et al*, 2019; Woan *et al*, 2015). For example, CRISPR screening has identified the histone methyltransferase Polycomb repressive complex 2 (PCR2) as a repressor of the transcription of MHC class I genes (Burr *et al.*, 2019). Reversal of this repression in a small cell lung cancer (SCLC) cell line using an inhibitor of EZH2, the catalytic core of PCR2, increased MHC class I protein levels and increased T cell-mediated killing. This suggests that reversing the suppression of MHC class I gene expression may be beneficial for the anti-tumor immune response.

In 2022, genome instability and evasion of immune destruction were classified as hallmarks of cancer (Hanahan, 2022). Interestingly, some work has linked these two processes. For example, cyclic GMP-AMP synthase (cGAS) surveillance of micronuclei was shown to link genomic instability to innate immune activation (Mackenzie *et al*, 2017). Further evidence for this link was provided by the inhibition of cyclin-dependent kinase 7 (CDK7) (Zhang *et al*, 2020), where its inhibition in small cell lung cancer (SCLC) induced DNA replication stress and genomic instability that triggered immune response signaling. Recent evidence suggests that cytoplasmic RNA-DNA hybrids (R-loops) are capable of

activating the innate immune response (Crossley *et al*, 2023). Mechanistically, perturbation of nuclear R-loops leads to an increase in cytoplasmic R-loops that bind to the pattern recognition receptors cGAS and TLR3. This binding is sufficient to induce an innate immune response. These studies demonstrate that the accumulation of aberrant nucleic acid species can be sensed by specialized receptors, thereby activating an innate immune response. One source of threat to genomic stability that, if uncontrolled, can lead to the accumulation of such aberrant nucleic acids is transcription-replication conflicts (Gomez-Gonzalez & Aguilera, 2019).

1.2 Transcription-replication conflicts (TRCs)

During the S-phase of the cell cycle, a complete duplication of the genome is required for cells to proliferate and obtain the complete genetic information for each of the daughter cells. This process is known as DNA replication. At the same time, transcription during S-phase is important for the expression of genes that are important for S-phase progression or that are too long to be transcribed in the G1-phase, and their transcription extends into S-phase (Lalonde *et al*, 2021). Transcription and replication share the same DNA template, raising the possibility of conflicts between the machinery of these two processes.

1.2.1 Types of TRCs

Depending on the relative direction of transcription and replication, either co-directional or head-on collisions can occur. In both bacteria and eukaryotes, head-on collisions have been shown to pose a greater threat to genomic stability than co-directional conflicts (Mirkin & Mirkin, 2005; Prado & Aguilera, 2005; Srivatsan *et al*, 2010). This may be due to positive DNA supercoiling between the converging machinery of transcription and replication, which impedes DNA unwinding and thus inhibits both processes (Bermejo *et al*, 2012; Hamperl & Cimprich, 2016). It was also shown that head-on collisions activate ATR kinase and increase R-loop levels, whereas co-directional collisions activate ATM kinase and decrease R-loop levels (Hamperl *et al*, 2017).

1.2.2 Mechanisms for limiting TRCs or their subsequent genomic instability

1.2.2.1 Direction of transcription

Transcription-replication conflicts (TRCs) are a threat to genomic stability, so cells must have mechanisms to prevent their occurrence, or at least to limit the deleterious consequences when they do occur. For example, in bacteria, highly expressed ribosomal genes are co-directed with replication (Rocha, 2004), and reversing this bias by inducing head-on transcription impairs replication and causes genomic instability (Srivatsan *et al.*, 2010).

1.2.2.2 Prevention of R-loop formation

R-loops are RNA/DNA hybrids that form co-transcriptionally and can pose a threat to genomic integrity. Several proteins function to limit the accumulation of R-loops, which can impede replication fork progression (Hamperl & Cimprich, 2016). One example is TFIIIS, which stimulates transcript cleavage when RNAPII backtracks and allows transcription to restart (Izban & Luse, 1992). Expression of a mutant TFIIIS has been shown to increase R-loop levels and induce genomic instability (Zatreanu *et al.*, 2019). Other proteins such as Aquarius or Senataxin have also been shown to resolve R-loops, thereby limiting DNA damage and TRCs (Hamperl & Cimprich, 2016).

Other co-transcriptional mechanisms that limit TRCs have been observed, such as transcription-coupled nucleotide excision repair, control of RNAPII elongation rate, and transcription termination (Hamperl & Cimprich, 2016). In addition, other replication-associated mechanisms have also been shown to be important for limiting TRCs (Hamperl & Cimprich, 2016).

1.2.3 MYC and transcription-replication coordination

To limit conflicts between the transcription and replication machinery, MYCN activates Aurora-A (Roeschert *et al.*, 2021). Mechanistically, MYCN activates Aurora-A kinase,

which phosphorylates H3S10, thereby preventing co-transcriptional R-loop accumulation (Figure 1.1). This observation inspired an *in vivo* experiment in which MYCN-amplified neuroblastoma was treated with a combination of Aurora-A and ATR inhibitors, which cured a subset of mice. Another study showed that MYCN interacts with the nuclear RNA exosome and recruits it to its target genes (Papadopoulos *et al*, 2022), thereby preventing transcription-replication conflicts and allowing rapid proliferation of neuroendocrine tumor cells (Figure 1.1).

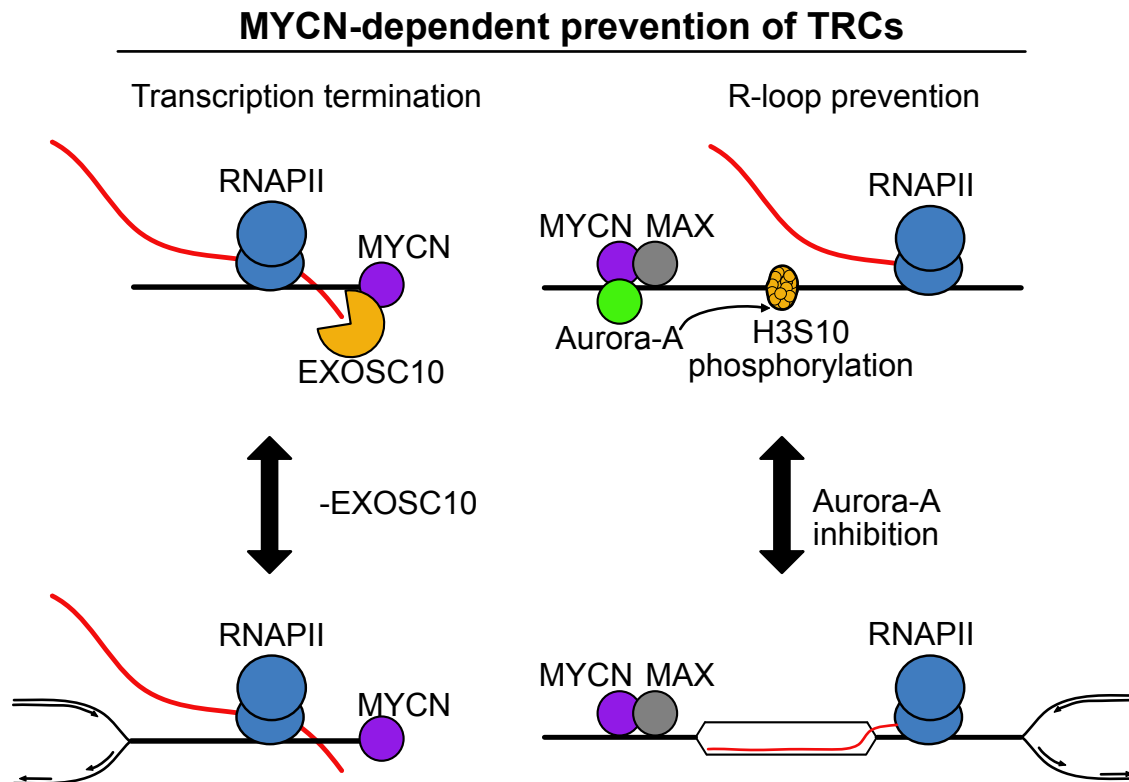


Figure 1. 1: Mechanisms describing how MYCN prevents TRCs.

1.3 MYC oncoproteins

The *MYC* gene is an oncogene that is frequently deregulated in human cancers (Dang, 2012; Kalkat *et al*, 2017; Schaub *et al*, 2018). MYC proteins are a group of oncoproteins consisting of three paralogs, namely MYC, MYCN and MYCL. Different MYC paralogs are deregulated in different tumors. Overexpression of MYC drives various hematological and solid tumors (Dang, 2012). While MYCN is upregulated in neural and neuroendocrine

Introduction

cancers, including medulloblastoma and neuroblastoma (Kohl *et al*, 1983; Rickman *et al*, 2018; Schwab *et al*, 1983), MYCL is known to be deregulated in small-cell lung cancer (Makela *et al*, 1991; Nau *et al*, 1985). On the one hand, overexpression of *Myc* in transgenic mice was sufficient to induce lymphoid malignancy (Adams *et al*, 1985). On the other hand, depletion of MYC abolishes tumorigenesis in many tumor models (Dhanasekaran *et al*, 2022; Sansom *et al*, 2007).

Because of its strong oncogenic potency, much effort has been devoted to studying and understanding its function with the goal of controlling tumor growth by targeting its oncogenic function.

1.3.1 Structure and canonical function of MYC

MYC proteins are transcription factors that form a heterodimeric DNA-binding complex with its partner protein MAX. This interaction is mediated by the helix-loop-helix-leucine zipper (HLH-LZ) domain of MYC, which allows promoter and enhancer binding (Balupuri *et al*, 2020; Blackwood & Eisenman, 1991). In addition to the HLH-LZ domain, MYC oncoproteins contain six highly conserved "boxes" that allow them to associate with various proteins (Figure 1.2). Some of these interactions have well-characterized functions. For example, proteasome-mediated degradation of MYC is controlled by MYC box I (Farrell & Sears, 2014). In addition, MYC box 0 and I bind Aurora-A kinase, antagonizing FBXW7 binding, and thereby stabilizing MYCN and MYC (Dauch *et al*, 2016; Richards *et al*, 2016).

Introduction

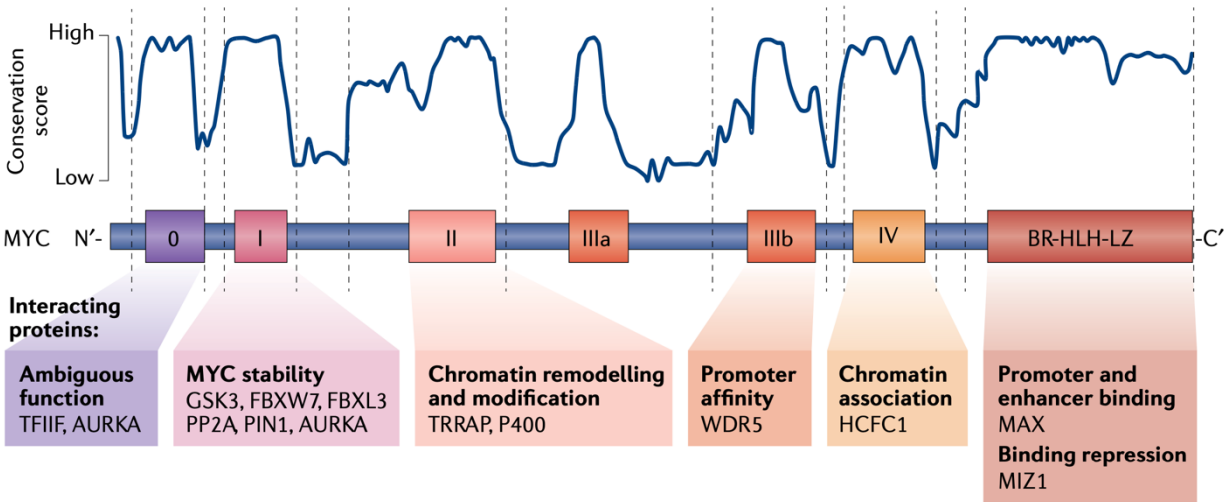


Figure 1. 2: Protein domains of MYC and their canonical function.

Conservation score is calculated based on amino acid sequence similarity with MYC proteins.

This figure was published in a similar form in (Balupuri *et al.*, 2020).

Notably, different paralogs of MYC may have distinct functions. For example, using a unique cellular CRISPR activation model, a study showed that MYC, in contrast to MYCN and MYCL, represses *BCL2* transcription by interacting with MIZ1 and DNMT3a (Dammert *et al.*, 2019). This repression drives sensitivity to inhibition of cell cycle control and increased apoptotic priming. In addition, the same study showed that activation of MYC leads to increased genotoxic stress and sensitivity to DNA damage checkpoint inhibitors.

1.3.2 Models of MYC function

Since its discovery in the early 1970s, MYC has been recognized as a driver of tumorigenesis, raising the question: How does MYC promote tumorigenesis or how does MYC exert its function in general? Several models of how MYC exerts its oncogenic function have been proposed (Balupuri *et al.*, 2020).

Recent advances in proteomics have led to several studies describing the MYC or MYCN interactome (Balupuri *et al.*, 2019; Buchel *et al.*, 2017; Kalkat *et al.*, 2018). These interactomes identified a broad and unexpected range of proteins that interact with MYC

or MYCN, including other transcription factors, transcription elongation factors, DNA replication and repair machinery, chromatin remodelers, and RNA splicing and processing factors. A model of MYC function that was based on these observations is the hand-over regulation model, in which MYC functions to recruit these factors to promoters where they can exert their functions.

1.3.3 MYC multimerization

The ability of MYC to form multimeric structures in response to various stress stimuli has recently been reported (Solvie *et al*, 2022). MYC multimers form in unperturbed U2OS cells and are enhanced by perturbation of transcription elongation, mRNA splicing, or inhibition of the proteasome. Multimerization of MYC blocks antisense transcription and stabilizes the association of DNA damage repair proteins on chromatin, limiting the occurrence of double-strand breaks. It is therefore thought to be a mechanism that allows tumor cells to proliferate under stressful conditions.

1.4 PAF1c and MYC

MYC interacts with the polymerase II-associated factor 1 complex (PAF1c) (Endres *et al*, 2021; Jaenicke *et al*, 2016), which is a highly conserved complex that travels with the RNAPII and is necessary for RNAPII elongation (Van Oss *et al*, 2017). In yeast, Paf1c consists of five subunits, Paf1, Ctr9, Cdc73, Rtf1, and Leo1. In other organisms, such as humans, an additional subunit, SKI8, has been identified (Zhu *et al*, 2005).

PAF1c has two opposing functions in the regulation of promoter proximal pausing of RNAPII (Chen *et al*, 2015; Yu *et al*, 2015). One study has shown that PAF1c in human monocytic leukemia cells (THP1) drives pause release of the RNAPII at more than 5800 genes (Yu *et al.*, 2015). This study showed a mutual recruitment dependence between the PAF1c and p-TEFb, thereby promoting the pause release of the RNAPII. In contrast, the other study showed that PAF1c promotes RNAPII pausing (Chen *et al.*, 2015). Using human colon cancer cells, this study showed that depletion of PAF1 caused a strong pause release of RNAPII into gene bodies. A model was proposed, in which PAF1c

Introduction

antagonizes p-TEFb recruitment and its depletion increases p-TEFb chromatin association, thereby promoting RNAPII pause release. The discrepancy between these two studies may be due to the different genetic backgrounds of the different cells used. In conclusion, the role of PAF1c in regulating RNAPII pause release is complex and may depend on the genetic background.

Chromatin structure is influenced by the PAF1c (Van Oss *et al.*, 2017; Van Oss *et al.*, 2016). RTF1, a subunit of PAF1c, has been shown to directly stimulate H2B ubiquitylation (H2Bub) through interaction with the ubiquitin conjugase RAD6 (Van Oss *et al.*, 2016). In addition, several studies have shown that PAF1c-dependent H2Bub modulates the elongation rate of RNAPII (Hou *et al.*, 2019; Wang *et al.*, 2022b).

Structural studies revealed that RFT1 affects the translocation of RNAPII, thereby allosterically stimulating RNAPII elongation (Vos *et al.*, 2020). Using rapid target depletion, the Cramer lab showed that PAF1 and CTR9 depletion had little effect on cellular RNA synthesis (Zumer *et al.*, 2021). In contrast, RTF1 depletion caused a decrease in RNAPII velocity. A model has been proposed in which there are two distinct barriers to early transcription elongation: the promoter-proximal pause site and the +1 nucleosome. It is most likely that the first barrier (promoter-proximal pause) allows the loading of factors, such as SPT6, that are needed to overcome the second barrier (+1 nucleosome). Recently, loss of SPT6 was shown to drive promoter-proximal pause release of the RNAPII through impaired recruitment of the PAF1c (Aoi *et al.*, 2022). While short genes show a release accompanied by an increase in mature transcripts upon SPT6 degradation, long genes are released but do not yield mature transcripts due to decreased processivity of RNAPII as a result of SPT6 and PAF1c loss.

The transfer of PAF1c from MYC to RNA polymerase II (RNAPII) requires ubiquitylation of MYC (Jaenicke *et al.*, 2016). This ubiquitylation is mediated by the E3 ligase HUWE1 and couples transcription elongation with double-strand break repair at active promoters (Endres *et al.*, 2021). The transfer of PAF1c from MYC to RNAPII is therefore important for maintaining the genomic integrity of MYC-driven tumor cells.

Introduction

In budding yeast, PAF1c has been shown to prevent transcription-replication conflicts (Poli *et al*, 2016). Upon exposure to the DNA damage inducing agent hydroxyurea (HU), PAF1c cooperates with INO80 and Mec1 to enhance the degradation of chromatin-bound RNAPII, allowing cells to recover from replication stress. In another study, UV irradiation induced loading of PAF1c on RNAPII by the transcription-coupled repair factor CSB (van den Heuvel *et al*, 2021). This allows transcriptional recovery in response to DNA damage. More recently, PAF1c has been shown to be directly involved in RNAPII chromatin removal upon DNA damage (Chen *et al*, 2022a). Using yeast as a model, it has been shown that upon DNA damage, Spt5 is dephosphorylated, weakening its interaction with Rtf1 and allowing the recruitment of Rad26 and the elongin-cullin E3 complex to stalled RNAPII, facilitating its removal.

1.5 MYC as a regulator of immune evasion

The ability of cancer to evade immune destruction was classified as an emerging hallmark of cancer in 2011 (Hanahan & Weinberg, 2011). Since then, sufficient evidence has emerged to reclassify “avoiding immune destruction” as a core hallmark of cancer (Hanahan, 2022). As a classical oncogene, many studies suggest that MYC plays a critical role in evading recognition and elimination of cancer cells by the host immune system (Dhanasekaran *et al.*, 2022).

MYCN amplification lead to downregulation of the expression of MHC class I genes (Bernards *et al*, 1986). Overexpression of the *N-myc* gene in rat neuroblastoma cells lead to downregulation of MHC class I antigens and was associated with increased *in vivo* growth rate and metastatic potential of these cells. A similar effect on the downregulation of MHC class I molecules has also been shown for MYC (Braun *et al*, 1992; Versteeg *et al*, 1988).

Numerous studies have linked deregulated MYC expression to cancer immune evasion (Dhanasekaran *et al.*, 2022). For example, MYC has been shown to regulate the expression of two important immune checkpoints, PD-L1 and CD47 (Casey *et al*, 2016). In a mouse model of lung adenocarcinoma, another study showed that MYC and RAS

Introduction

cooperate to induce an inflammatory phenotype and an immunosuppressive microenvironment (Kortlever *et al*, 2017). In this model, MYC-induced tumor progression was dependent on IL-23 and CCL9. Another study demonstrated the importance of MYC-MIZ1-mediated suppression of the type I interferon pathway (Muthalagu *et al*, 2020), and that interfering with this suppression allows B cell and NK cell infiltration of pancreatic tumors.

Our laboratory has recently proposed a novel mechanism by which MYC mediates immune escape in pancreatic ductal adenocarcinoma (PDAC) (Krenz *et al*, 2021). In this study, MYC depletion resulted in regression of established PDAC tumors and this regression was immune cell dependent. In addition, TANK-binding kinase 1 (TBK1) was implicated and its activation was shown to be required for tumor regression upon MYC depletion. Interestingly, MYC depletion delayed S-phase progression and decreased the rate of nucleotide incorporation during DNA replication. In summary, this study demonstrates two important findings: First, MYC mediates immune escape in PDAC, and second, MYC promotes S-phase progression.

1.6 Aim of the thesis

The role of MYC in mediating immune evasion has been demonstrated by our laboratory and others in many cancer entities. Several mechanisms have been proposed to explain how MYC mediates this function. However, targeting this oncogenic function of MYC while sparing its physiological functions has not been successful to date.

Recently, several interactomes of MYC have been published, with many of the interacting proteins appearing to be unexpected or previously unexplored (Balupuri *et al.*, 2019; Buchel *et al.*, 2017; Kalkat *et al.*, 2018). This raises the possibility that the oncogenic or immuno-evasive function of MYC may be mediated by one of its interactor proteins, and that the identification of this downstream factor may be dispensable for the physiological functions of MYC.

Introduction

This work builds on previous findings that MYC mediates immune evasion and promotes S-phase progression in PDAC (Krenz *et al.*, 2021). Testing the effect of depleting MYC-interacting proteins on S-phase progression was used as a strategy to search for proteins downstream of MYC that mediate this phenotype. Furthermore, the effect of depleting candidate proteins was tested *in vivo* in a mouse model of PDAC to evaluate their therapeutic relevance and whether they are important in driving MYC-mediated immune evasion.

2 Materials

2.1 Bacterial strains and cell lines

2.1.1 Bacterial strains

XL1-Blue

Escherichia coli strain, used for plasmid amplification and protein expression with the following genotype: *recA1, endA1, gyrA96, thi-1, hsdR17, supE44,relA1, lac [F' proAB lacIqZΔM15 Tn10 (Tetr)]*

2.1.2 Mammalian Cell lines

Cell line	RRID	description
KPC	NA	Murine PDAC cell line.
U2OS	CVCL_0042	Human osteosarcoma cell line
HEK293TN	CVCL_UL49	Human embryonic kidney cell line

KPC cells were provided by Jens Sieveke (2014). HEK293TN and U2OS cells were obtained from ATCC. Cells were regularly tested for mycoplasma contamination using standard methods (Arbeitsgemeinschaft Gentechnik, AM029).

2.2 Cultivation media and supplements

2.2.1 Media and antibiotics for bacterial culture

LB medium

10% Bacto tryptone, 0.5% Yeast extract, 1% NaCl

Materials

LB agar

LB medium with 1.2% Bacto-Agar Autoclaved, heated in a microwave oven, cooled to 50°C before adding specific antibiotics, approximately 10ml filled into 10 cm dishes.

Antibiotics

100 µg/ml ampicillin was added to the medium to select successfully transformed bacteria.

2.2.2 Cultivation media for cell culture

Mammalian cells were cultured in Dulbecco's Modified Eagle's Medium (DMEM) (Sigma-Aldrich) supplemented with 10% FBS (Biochrom and Sigma-Aldrich) and 1% penicillin-streptomycin (Sigma-Aldrich). Fetal bovine serum (FBS, Capricorn Scientific GmbH) was heat-inactivated at 56°C for 30 minutes.

Basal medium: DMEM, 10% FBS, 1% penicillin/streptomycin (Sigma)

Freezing medium: 50% basal medium, 40% FBS, 10% DMSO

Transfection Medium: DMEM, 2% FBS

2.2.3 Compound used for cell culture

Penicillin/streptomycin (100,000 U/ml, Sigma) was added to the culture media to avoid bacterial contamination. To select transfected or infected mammalian cells, 2 µg/ml puromycin (stock 10 mg/ml, InvivoGen) was added to the medium.

Doxycycline at a concentration of 1 µg/ml (stock 1 mg/ml, Sigma) was added for induction of the tetracycline-inducible shRNA system.

For infection of mammalian cells, 4 µg/ml Polybrene (Sigma-Aldrich) in sterile water was used.

2.3 Antibodies

2.3.1 Primary antibodies

Target protein	Supplier and catalog number	RRID	Dilution	Application
CD3	Abcam Cat# ab16669	AB_443425	1:100	Immunohistochemistry
CD4	Thermo Fisher Scientific Cat# 14-9766-82	AB_2573008	1:100	Immunohistochemistry
CD8	Lab Vision Cat# RB-9009-P1	AB_149750	1:100	Immunohistochemistry
F4/80	Abcam Cat# ab6640	AB_1140040	1:1,000	Immunohistochemistry
CD45R/B220	BD Biosciences Cat# 550286	AB_393581	1:50	Immunohistochemistry
KAP1 phospho-S824	Abcam Cat# ab70369	AB_1209417	1:500	Immunohistochemistry
γ -H2AX	Abcam Cat# ab2893	AB_303388	1:1,000	Immunohistochemistry
MYC	Abcam Cat# ab32072	AB_73165	1:5000	Immunoblotting
CTR9	Bethyl Cat# A301-395A	AB_960973	1:1000	Immunoblotting
CDC73	Cell Signaling Technology Cat# 3644	AB_2078386	1:1000	Immunoblotting
RTF1	Bethyl Cat# A300-179A	AB_2185963	1:1000	Immunoblotting

Materials

Vinculin	Sigma-Aldrich Cat# V9131	AB_477629	1:5000	Immunoblotting
Actin-beta	Sigma-Aldrich Cat# A5441	AB_476744	1:5000	Immunoblotting
KAP1 phospho- S824	Abcam Cat# ab70369	AB_1209417	1:5000	Immunoblotting
KAP1 phospho- S824	Abcam Cat# ab70369	AB_1209417	1:800	Immunofluorescence
Phospho- Histone H2A.X Ser139	Cell Signaling Technology Cat# 2577	AB_2118010	1:500	Immunofluorescence
total RNAPII	Santa Cruz Biotechnology Cat# sc-55492	AB_630203	1:1500	Proximity ligation
PCNA	Abcam Cat# ab92552	AB_10561973	1:1500	Proximity ligation
RAD9	Thermo Fisher Scientific Cat# PA5-21275	AB_11152972	1:500	Proximity ligation
RNAPII phospho Ser5	BioLegend Cat# 904001	AB_2565036	1:500	Proximity ligation
CTR9	Novus Cat# NB100-68205	AB_1108024	1:500	Proximity ligation
RNAPII	Santa Cruz Biotechnology Cat# sc-17798	AB_677355	15 µg 3 µg	ChIP-seq. ChIP-qPCR

Materials

SPT6	Novus Cat# NB100-2582	AB_2196402	10 µg 1.5 µg	ChIP-seq. ChIP-qPCR
SPT5	Santa Cruz Biotechnology Cat# sc-133217	AB_2196394	15 µg	ChIP-seq.
CTR9	Bethyl Cat# A301-395A	AB_960973	15 µg	ChIP-seq.
RTF1	Bethyl Cat# A300-179A	AB_2185963	3 µg	ChIP-qPCR
RNAPII phosphor- Ser2	Abcam Cat# ab5095	AB_304749	3 µg	ChIP-qPCR
SPT4	Cell Signaling Technology Cat# 64828	AB_2756442	1.5 µg	ChIP-qPCR

2.3.2 Secondary antibodies

Antibody	Host species	Supplier and catalog number	Application
Alexa Fluor® 488 anti-Mouse	Goat	A11017	Invitrogen
Alexa Fluor® 488 Goat Anti-Rabbit IgG (H+L)	goat	A-11008	Invitrogen
Alexa Fluor® 568 anti-Rabbit	Goat	A11036	Invitrogen
Alexa Fluor® 647 Goat Anti-Mouse IgG	goat	A-21235	Invitrogen

Materials

Alexa Fluor® 647 Goat Anti-Rabbit IgG (H+L)	goat	A-21244	Invitrogen
Anti-mouse IgG- HRP	Goat	Santa Cruz, sc- 2314	Immunoblotting
Anti-rabbit IgG- HRP	Goat	Santa Cruz, sc- 2314	Immunoblotting

2.4 Nucleic acids

2.4.1 shRNAs

All shRNA were designed using the algorithm published previously (Pelossof *et al*, 2017). Oligos were synthesized and obtained by Sigma-Aldrich and were purified by HPLC then stored at -20 °C. The shRNA targeting *Myc* was previously described in (Krenz *et al.*, 2021).

Target	Sequence of the 97mer
<i>Cdc73</i>	TGCTGTTGACAGTGAGCGAACTGATC TAGATGATGATATATAGTGAAGCCACA GATGTATATATCATCATCTAGATCAGT CTGCCTACTGCCTCGGA
<i>Ctr9</i>	TGCTGTTGACAGTGAGCGATGACACA GTTCTGATGTTTAATAGTGAAGCCACA GATGTATTAACATCAGAACTGTGTCA CTGCCTACTGCCTCGGA
<i>Rtf1</i>	TGCTGTTGACAGTGAGCGCAGCTCTC AATTATAAATTCAATAGTGAAGCCACA GATGTATTGAATTTATAATTGAGAGCT TTGCCTACTGCCTCGGA

Materials

Luciferase renilla	TGCTGTTGACAGTGAGCGCAGGAATT ATAATGCTTATCTATAGTGAAGCCACA GATGTATAGATAAGCATTATAATTCCT ATGCCTACTGCCTCGGA
--------------------	---

2.4.2 Primers

Primers were designed wither using either Primer3 or primer blast tool provided by the NCBI and were purchased from Sigma-Aldrich. qRT-PCR primers are designed as intron spanning to avoid false positive signals from genomic DNA.

2.4.2.1 Primers for mRNA detection

Target	Sequence of forward primer (5' to 3')	Sequence of reverse primer (3' to 5')
<i>Ctr9</i>	GCTCGAGGGCGACAAAATGG	CGGGTTAGTGCGCAATGCTT
<i>Supt6</i>	GAGGGCCCTTGCGGTGG	GCTGCTTCTCACAGCCTCCT
<i>H2-T23</i>	ATTCAGGTTCTCACAGACCC A	CGACAATGATGAACCGGGGC
<i>H2-D1</i>	ggaaaaggaggggactatgc	gcagctgtcttcacgcttta
<i>Vcl</i>	aggagactgcgaagacagg	gccgtcgccacttgttta

2.4.2.2 Primers for ChIP-qPCR

Target	Sequence of forward primer (5' to 3')	Sequence of reverse primer (3' to 5')
AG75_H2-D1 promoter	CGCTGGCAGGTCTCACTATCA	AGGCCGTTTCCCTCCCGA
AG76_H2-D1 distal#1	ACCCTGCTGACATCACCCCTG	CACCCACACCCTCCTTACCC
AG78_H2-K1 promoter	GTCTGAGTCGGAGCCAGGG	GCGCGATCACCAAGAACCAA
AG80_H2-K1 distal#2	GACAGAGCAGTGCAGGGACA	TGCCTGGAGTGGACTTGGTG
AG81_B2m promoter	CCGATTGGCTGTGAGTTCA	GCATACAGGCCGGTCAGTGA
AG83_B2m distal#2	CCGAGCCCAAGACCGTCTAC	GGTTCCTGGCCTGCTGTGTA
AG84_I <i>fi</i> 30 promoter	GGATGCTTGCGAAAGGGACG	ATGGGGCGTGGACTTAGTGG
AG85_I <i>fi</i> 30 distal#2	TTGCCTCCCAGTAACACCGG	AACAAACGTCAGGCCTCCCA

2.4.3 Plasmids

pLT3_GEPIR , lentiviral shRNA expression vector; Tet-on all in one system; puromycine resistance; PGK promoter; eGFP (inducible).

psPAX.2 (Addgene), plasmid for lentivirus production, encoding for virion packaging system.

pMD2.G (Addgene), Plasmid for lentivirus production, encoding for virion envelope.

2.5 Solutions and buffers

Buffers and solutions	Composition
Ammonium persulfate (APS; 10%)	100 mg/ml; aliquots stored at -20 °C
Annexin V binding buffer	10 mM HEPES, pH 7.4 140 mM NaCl 2.5 mM CaCl ₂
BCA buffer A	1% (w/v) BCA-Na ₂ 2% (w/v) Na ₂ CO ₃ x H ₂ O
BCA buffer B	4% (w/v) CuSO ₄
Bis-Tris (3.5 x)	1.25 M Bis-Tris, pH 6.7 Stored at 4 °C
Bis-Tris stacking gel	4% (v/v) acrylamide/bisacrylamide 1 x Bis-Tris 0.03% (v/v) APS 0.05% (v/v) TEMED
Bis-Tris separation gel	8 – 10% (v/v) acrylamide/bisacrylamide 1 x Bis-Tris 0.03% (v/v) APS 0.05% (v/v) TEMED
Blocking solution for ChIP	5 mg/ml BSA in PBS; sterile filtered with 0.45 µm vacuum filter, stored at 4 °C

Materials

Bradford reagent	0.01% (w/v) Coomassie Brilliant Blue G250 8.5% (v/v) phosphoric acid 4.75% (v/v) EtOH
ChIP elution buffer	50 mM Tris, pH 8.0 1 mM EDTA 1% SDS 50 mM NaHCO ₃ ; prepared immediately before use
ChIP elution buffer	1 % (v/v) SDS 0.1 M NaHCO ₃ prepared fresh in aqua dest
ChIP lysis buffer I	5 mM PIPES pH 8.0 85 mM KCl 0.5 % (v/v) NP40 protease inhibitor mix (1:1000, add fresh)
ChIP lysis buffer II	50 mM HEPES pH 7.9 140 mM NaCl 1 mM EDTA 1 % (v/v) TritonX-100 0.1 % (w/v) deoxycholic acid sodium salt 0.1 % (v/v) SDS protease inhibitor mix (1:1000, add fresh)
ChIP wash buffer I	20 mM Tris HCl pH 8.1 150 mM NaCl 2 mM EDTA 0.1 % (v/v) SDS 1 % (v/v) TritonX-100
ChIP wash buffer II	20 mM Tris HCl pH 8.1 500 mM NaCl 2 mM EDTA

Materials

	0.1 % (v/v) SDS 1 % (v/v) TritonX-100
ChIP wash buffer III	10 mM Tris HCl pH 8.1 250 mM LiCl 1 mM EDTA 1 % (v/v) NP40 1 % (v/v) deoxycholic acid sodium salt
DNA loading buffer (6 x)	10 mM EDTA, pH 8.0 0.2 % (w/v) Orange G 40 % (w/v) sucrose
Miniprep resuspension buffer	TE with RNaseA (1:1000, add fresh)
Miniprep lysis buffer	0.2 N NaOH 1 % SDS
Miniprep precipitation buffer	3 M KOAc, pH 5.2
NuPAGE transfer buffer (20 x)	500 mM Bis-Tris 500 mM Bicine 20.5 mM EDTA 0.1 mM chlorobutanol
NuPAGE transfer buffer (ready to use)	1x NuPAGE transfer buffer with 20 % methanol
MOPS running buffer (20 x)	1 M MOPS 1 M Tris 20 mM EDTA 2 % SDS
MOPS running buffer (ready to use)	1x MOPS running buffer with 5 mM sodium bisulfite
PBS	137 mM NaCl 2.7 mM KCl 10.1 mM Na ₂ HPO ₄ 1.76 mM KH ₂ PO ₄ autoclaved
RIPA lysis buffer	50 mM HEPES, pH 7.9 140 mM NaCl 1 mM EDTA 1 % Triton X-100 0.1 % Na-deoxycholate

Materials

	0.1 % SDS 1 mM PMSF (add fresh) protease and phosphatase inhibitors (1:1000, add fresh)
RNase A (10 mg/ml)	100 mg RNase A 27 µl 3 M sodium acetate, pH 5.2 9 ml ddH ₂ O boiled for 30 min at 100°C to inactivate DNases 50 µl 1 M Tris, pH 7.4 added per aliquot
TBS (20 x)	500 mM Tris base 2.8 M NaCl adjusted to pH 7.4 with concentrated HCl
TBS-T	1 x TBS 0.2 % Tween-20
TE	10 mM Tris, pH 7.4 1 mM EDTA, pH 8.0
Trypsin solution	0.25 % trypsin 5 mM EDTA 22.3 mM Tris, pH 7.4 125 mM NaCl
Laemmli Sample Buffer 6x	12% (w/v) SDS 60‰ (w/v) bromphenol blue 47% (v/v) glycerol 60 mM Tris/HCl, pH 6.8 9.3% (w/v) DTT Aliquoted and stored at -20 °C
Doxycycline 1 mg/ml	50 mg Doxycycline in 50 ml ethanol aliquoted and stored at -20 °C
Deoxynucleotide triphosphate (dNTP) mix (10 mM)	50 µl per dNTP (100 mM), fill up to 500 µl with water, stored at -20 °C

Materials

BSA/PBS	5 mg/ml BSA in PBS sterile filtered (0.2 µm), stored at 4 °C
Proteinase K	10 mg/ml in ddH ₂ O, aliquots stored at -20 °C
Polybrene stock	200 mg dissolved in 50 ml H ₂ O; sterile filtered with 0.2 µM syringe filter, aliquots stored at -20 °C

2.6 Enzymes, standards and kits

2.6.1 Enzymes

Benzonase nuclease	Merck
DNase I	Thermo Fisher Scientific
Gateway BP clonase II	Life Technologies
Gateway LR clonase II	Life Technologies
M-MLV Reverse Transcriptase	Promega
Phusion Hot Start II HF	Thermo Fisher Scientific
DNA polymerase Proteinase K	Roth
Restriction enzymes	Thermo Fisher Scientific
RNase A	Roth
SYBR®Green qPCR Mastermix	Thermo Fisher Scientific
Trypsine (sequencing-grade modified)	Promega
XhoI	Thermo Fisher Scientific
AsiSI	New England Biolabs
T4 DNA Ligase, concentrated	New England Biolabs
T4 RNA Ligase 2, truncated	New England Biolabs
M-MLV reverse transcriptase	Promega
Proteinase K	Roth

Materials

2.6.2 Standards

1 kb DNA Ladder	New England Biolabs
HiMark pre-stained HMW STD	Thermo Fisher Scientific
1 kb DNA Ladder	Agilent

2.6.3 Kits

Agencourt AMPure® XP Beads	Beckman Coulter
Agencourt RNAClean XP Beads	Beckman Coulter
Click-iTTM EdU Cell Proliferation Kit for Imaging, Alexa Fluor™ 647 dye	Thermo Fisher Scientific
Duolink® In Situ PLA® Probe Anti-Rabbit PLUS	Sigma
Duolink® In Situ PLA® Probe Anti-Rabbit PLUS	Sigma
Duolink® In Situ PLA® Probe Anti-Mouse MINUS	Sigma
Duolink® In Situ Detection Reagents Red	Sigma
Dynabeads® Protein A	Thermo Fisher Scientific
Dynabeads® Protein G	Thermo Fisher Scientific
Dynabeads™ MyOne™ streptavidin T1 beads	Invitrogen
Immobilon Western Substrate	Millipore
MAXtract high-density tubes	Qiagen
miRNeasy Mini Kit	Qiagen
NEBNext® rRNA Depletion Kit	New England Biolabs
NEBNext® Ultra II Directional RNA Library Prep Kit for Illumina	New England Biolabs
NEBNext® Multiplex Oligos for Illumina®	New England Biolabs

Materials

NEBNext® RNA Sample Purification Beads	New England Biolabs
NEBNext® Sample Purification Beads	New England Biolabs
NEBNext® Ultra II DNA Library Prep Kit for Illumina	New England Biolabs
NEBNext® Oligo d(T)25 Magnetic Beads	New England Biolabs
NextSeq® 500/550 High Output Kit v2.5 (75 cycles)	Illumina
NGS Fragment High Sensitivity Analysis Kit, 1-6,000 bp, 500 samples	Agilent
PowerUp™ SYBR® Green Master Mix	Thermo Fisher Scientific
PureLink® HiPure Plasmid Maxiprep Kit	Life Technologies
QIAquick PCR Purification Kit	Qiagen
QIAquick Gel Extraction Kit	Qiagen
QIAzol Lysis Reagent	Qiagen
Quant-iT PicoGreen dsDNA assay	Thermo Fisher Scientific
Quant-iT™ RiboGreen® RNA Assay Kit	Thermo Fisher Scientific
Quick Blunting Kit	New England Biolabs
Random Primer	Sigma/Roche
RNeasy Mini Kit	Qiagen
RNeasy MinElute Cleanup Kit	Qiagen
SuperScript III Reverse Transcriptase Kit	Thermo Fisher Scientific
TURBO™ DNase (2 U/μL)	Thermo Fisher Scientific

2.7 Consumables

Supplies including reaction tubes, cell culture dishes, and other plastic products from Applied Biosystems, B. Braun, Eppendorf, Greiner, Kimberly-Clark, Eppendorf, Greiner, Nunc, Sarstedt, GLScience, Thermo Scientific, VWR and Millipore were used.

2.8 Software

FastQC v0.11.3	https://www.bioinformatics.babraham.ac.uk/projects/fastqc/
Bowtie2 v2.3.4.1 (Langmead & Salzberg, 2012)	http://bowtie-bio.sourceforge.net/bowtie2/index.shtml
MACS2 v2.1.2 (Zhang <i>et al</i> , 2008)	https://github.com/macs3-project/MACS
SAMtools v1.9 (Li <i>et al</i> , 2009)	http://www.htslib.org/
Integrated Genome Browser v9.1.10 (Freese <i>et al</i> , 2016)	https://bioviz.org/
GraphPad Prism v8.2.1 for Mac GraphPad software	https://www.graphpad.com/scientific-software/prism/
Harmony High Content Imaging and Analysis Software PerkinElmer	http://www.perkinelmer.de/product/harmony-4-8-office-hh17000001
StepOne software v2.3 StepOne	https://www.thermofisher.com/de/de/home/technical-resources/software-downloads/StepOne-and-StepOnePlus-Real-Time-PCR-System.html
enrichR v3.1 (Xie <i>et al</i> , 2021)	https://cran.r-project.org/web/packages/enrichR/vignettes/enrichR.html
GOstats v2.64.0 (Falcon & Gentleman, 2007)	https://bioconductor.org/packages/release/bioc/html/GOstats.html
Rsubread v2.12.2 (Liao <i>et al</i> , 2019)	https://bioconductor.org/packages/release/bioc/html/Rsubread.html
R version v4.2.2	The R Foundation https://www.R-project.org/
DeepTools v3.5.1 (Ramirez <i>et al</i> , 2014)	https://deeptools.readthedocs.io/en/develop/

Materials

ChIPseeker v1.34.1 (Wang <i>et al</i> , 2022a)	https://guangchuangyu.github.io/software/ChIPseeker
UMI-tools v1.0.1 (Smith <i>et al</i> , 2017)	https://umi-tools.readthedocs.io/en/latest/
Living Image® Software - PerkinElmer® IVIS® Systems	https://www.perkinelmer.com/in_vivo/imaging
QuPath v0.3.2 (Bankhead <i>et al</i> , 2017)	https://qupath.github.io/

2.9 Equipment

Automated capillary electrophoresis	Fragment Analyzer TM (Agilent) Experion TM (Bio-Rad)
Chemiluminescence imaging	LAS-4000 mini (Fujifilm)
Cell culture incubator	BBD 6220 (Heraeus)
Centrifuges	Centrifuge 5417 R (Eppendorf) Centrifuge 5424 (Eppendorf) Heraeus Multifuge 1S-R (Thermo Fisher Scientific) Heraeus Megafuge 40R (Thermo Fisher Scientific)
Deep Sequencer	NextSeq 500 (Illumina)
Fluorescence readers	Infinite 200 PRO Microplate Reader (Tecan)
Heating block	Dry Bath System (Starlab)
High-Content Imaging	Operetta® High-Content Imaging System (PerkinElmer)
Cell Counter	Casy® cell counter (Innovatis) Countess TM (Thermo Fisher Scientific)

Materials

Immunoblot transfer chamber	PerfectBlue Tank Electro Blotter Web S (Peqlab)
Photometer	Ultrospec™ 3100 pro UV/Visible (Amersham Biosciences) NanoDrop 1000 (Thermo Fisher Scientific)
Quantitative RT-PCR machine	StepOne™ Realtime Cyclers (Applied Biosystems)
PCR thermal cycler	Mastercycler pro S (Eppendorf)
SDS-PAGE system	Mini-PROTEAN Tetra Cell (Bio-Rad)
Sterile bench	HeraSafe (Heraeus)
Thermoshaker	Thermomixer® comfort (Eppendorf)
Ultrasonifier	Digital Sonifier® W-250 D (Branson)
UV fluorescent table	Maxi UV fluorescent table (Peqlab)
Vortex Mixer	Vortex-Genie 2 (Scientific Industries)
Whatman filter paper	Gel Blotting Paper (Schleicher and Schuell)

3 Methods

Most of the methods listed below may be published in a similar form in Gaballa et al., *Manuscript under consideration*.

3.1 Cell culture methods

3.1.1 Cell cultivation, splitting, freezing and thawing

HEK293TN (RRID: CVCL_UL49), KPC and U2OS (RRID: CVCL_0042) cells were grown in DMEM (Sigma-Aldrich) supplemented with 10% FCS (Biochrom and Sigma-Aldrich) and 1% penicillin-streptomycin (Sigma-Aldrich). KPC cells were provided by Jens Sieveke (2014). HEK293TN and U2OS cells were obtained from ATCC. Cells were grown in a cell incubator at 37°C, 5% CO₂ and 95% relative humidity. Cells in culture were routinely tested for mycoplasma contamination.

Cells were passaged every third day. To do this, the medium was removed. The cells were washed with PBS and detached from the cell culture plate using trypsin/EDTA. Trypsin/EDTA was inhibited by adding full serum containing medium and cells were re-suspended. Some of the resuspended cells were plated onto a new dish containing fresh medium, while the remaining cells were discarded. Cell number was determined using Casy® cell counter according to the manufacturer's recommendations for seeding a defined number of cells.

To store the cells in liquid nitrogen, the medium was removed from a 70% confluent cell culture dish. The cells were washed, trypsinised and harvested as described above. Cell suspension was transferred to 15ml tube and centrifuged at 1,000rpm for 5 minutes. The supernatant was discarded. The cells were resuspended in freezing medium and transferred to cryo vials. MrFROSTY freezer was used at -80°C overnight to ensure slow freezing (1°C per minute).

Methods

To thaw cells, frozen cells were rapidly incubated in a water bath at 37 °C and resuspended in the complete medium. The solution was transferred to a 15 ml tube and centrifuged at 1,000 rpm for a period of 5 minutes. The cells were resuspended in fresh medium and plated onto a new cell culture dish after removal of the supernatant.

3.1.2 Lentiviral Infection

Stable cell lines were generated using psPAX2 (Addgene 12260) and pMD2.G (Addgene 12259) lentiviral packaging plasmids. HEK293 cells were used for lentiviral production. For this purpose, a 10 cm cell culture dish was seeded with 5×10^6 HEK293T cells. The next day, the cells were transfected using PEI, 10 µg of the packaging vector psPAX2, 2.5 µg of the envelope vector pMD2G and 10 µg of the lentiviral expression plasmid (pLT3 vector harboring target shRNA) were used to transfect. A 0.45 µm filter was used to filter out cells to provide Cell-free virus-containing supernatants. For long-term storage, the virus was aliquoted and stored at -80 °C or used directly for lentiviral infection of cells. shRNAs against CTR9, CDC73 and RTF1 were selected as previously described (Pelosof *et al.*, 2017) and were lentivirally transduced into the cell genome. KPC cells were infected with lentiviral supernatants in the presence of 4 µg/ml polybrene for 24 h. The cells were selected with puromycin at 2 µg/ml for two days. KPC cells harbouring shMYC were used as previously described (Krenz *et al.*, 2021).

3.1.3 siRNA transfection

siRNA transfection was performed using RNAiMAX reagent (Thermo Fisher Scientific) according to the manufacturer's reverse transfection protocol. For a 96-well plate with a final volume of 100 µl per well, 0.3 µl Lipofectamine RNAiMAX (Thermo Fisher Scientific) was mixed with 20 µl Opti-MEM™ (Thermo Fisher Scientific) and incubated for 10 minutes. Then siRNA was added to a final concentration of 25 nM and incubated for 10 minutes. Then 80 µl of single cell suspension in DMEM (Thermo Fisher Scientific) supplemented with 2% FCS was added to give a final volume of approximately 100 µl per well.

3.2 Cell biology methods

3.2.1 Immunofluorescence staining

Cells were plated on 96-well plates (Perkin Elmer) for immunofluorescence staining. Cells were treated with 10 mM EdU (Jena Bioscience) for 30 min for EdU pulse experiments in Figure 1b or siRNA screens in Figure 2a-c. Cells were fixed with 4% methanol-free PFA (Science Services) for 10 min at RT. Permeabilization was performed with 0.5% w/v Triton X-100/PBS for 15 min at RT. Blocking was performed with 5% w/v BSA/PBS for 1 h at RT. For the EdU pulse experiments, the newly synthesised DNA was visualised by means of copper(I)-catalysed azide-alkyne cycloaddition (100 mM Tris pH 8.5, 4 mM CuSO₄, 10 mM AFDye 647 Azide (Jena Bioscience), 10 mM L-ascorbic acid). Subsequently, the cells were incubated with the primary antibodies in blocking buffer overnight at 4°C. After washing, the cells were incubated with the appropriate fluorophore-conjugated secondary antibodies for 1 hour at room temperature. Nuclei were counterstained with 2.5 mg/ml Hoechst 33342 (Sigma-Aldrich) for 10 min at RT. Images were captured using an Operetta CLS High-Content Imaging System at 20 ×, 40 × or 63 × magnification with a water immersion objective. The images were processed and analysed using Harmony High Content Imaging and Analysis Software (PerkinElmer) and R software.

3.2.2 Proximity ligation assay

In a 384-well format (PerkinElmer), KPC cells expressing doxycycline-inducible shRNA targeting *Myc* were seeded. Where specified, cells were treated with doxycycline (1mg/ml, 48 hours) or ethanol at equivalent concentrations. Fixation and permeabilization were performed as described for immunofluorescence staining. Cells were incubated with the indicated mouse and rabbit antibodies in blocking buffer overnight at 4°C. The cells were incubated with the indicated mouse and rabbit antibodies in blocking buffer overnight at 4 °C. They were incubated with plus (Sigma-Aldrich, DUO92002) and minus (Sigma-Aldrich, DUO92004) probes targeting rabbit and mouse antibodies, respectively, for 1 h at 37°C. Ligation was performed for 30 min at 37°C after washing with PLA Wash Buffer A (Sigma-Aldrich). *In situ* PCR amplification using Alexa 495 (Sigma-Aldrich,

Methods

DUO92014) or 644 (Sigma-Aldrich, DUO92013) conjugated oligonucleotides was then performed after washing with PLA Wash Buffer A for 2 h at 37C. Counterstaining was performed using Hoechst 33342 (Thermo Fisher Scientific). Images were acquired using the Operetta CLS High-Content Analysis System at 40x magnification (PerkinElmer). Images were processed and analysed using Harmony High-Content Imaging and Analysis Software (PerkinElmer) and Prism v8.2.1.

3.2.3 Live cell imaging

KPC cells carrying shRNA against *Ctr9* were seeded in 24-well plates (Greiner) and cell proliferation was assessed using the Incucyte SX5 after the indicated treatments, with 9 fields analysed every 8 hours using a 10x objective.

3.2.4 siRNA screen

RNAi cherrypick library (SMARTpool, Horizon Discovery) was diluted according to manufacturer's instructions. KPC cells were seeded in 96-well plates (PerkinElmer) and simultaneously transfected with Lipofectamine RNAiMAX (Thermo Fisher Scientific) according to the manufacturer's instructions using reverse transfection at a final concentration of 25 nM siRNA/well. Cells were fixed 48 hours after transfection. As described for immunofluorescence staining, EdU pulse and staining were performed. The percentage of positive cells was used to calculate the z-score, where $z = (x - \mu) / \sigma$ (x is the percentage of positive cells in a given well, μ is the percentage of positive cells in all wells and σ is the standard deviation across all wells). The Z-score was calculated to rank the candidates in terms of their effect on the increase/decrease in the percentage of positive cells.

3.3 Molecular and biochemical methods

3.3.1 Chromatin immunoprecipitation (ChIP)

Cells were incubated with 1% formaldehyde for 10 minutes to fix proteins to DNA. For this purpose, 20 ml of cell culture medium was directly supplemented with 540 μ l of 37% formaldehyde on a 15 cm plate. Fixation was stopped with 2.5 ml of 1 M glycine (5 min, RT). The cells were washed twice with ice-cold 1x PBS. The cells were scraped from the plate in 2 ml of PBS containing protease and phosphatase inhibitors as well as 1 mM PMSF and transferred to a 15 ml Falcon tube. Pelleting was performed for 20 min at 1500rpm and 4°C. The supernatant was aspirated and either snap frozen in liquid nitrogen for storage at -80°C or further processed.

Chromatin isolation involved a two-step lysis. Firstly, the cells were lysed in ChIP lysis buffer I for isolation of nuclei, incubated for 20 min on ice and centrifuged for 15 min at 1500rpm at 4°C. ChIP lysis Buffer II was then used for at least 10 min on ice to isolate the chromatin. Protease and phosphatase inhibitors were freshly added to both buffers. The chromatin was then fragmented using a sonicator (total time 20 min with 10 s pulses and 30 s pauses with 25% amplitude) to obtain a fragment size between 150-300 bp. Chromatin was centrifuged at 14,000 rpm for 30 min at 4°C.

To control for fragmentation efficiency, 20 μ l of chromatin was mixed with 280 μ l of TE buffer containing 160 mM NaCl and 20 μ g/ml RNase A and incubated at 37 °C for 1 h, followed by the de-crosslinking step at 65 °C overnight. After adding 5 mM EDTA and 200 μ g/ μ l Proteinase K, chromatin was purified by phenol-chloroform extraction followed by precipitation with 100% EtOH and 30 μ l NaAc (stock: 3 M, pH 5.2) and washed with 70% EtOH. The pellet was air dried. It was resuspended in 20 μ l ddH₂O. 10 μ l of the chromatin was mixed with 6 x DNA loading dye and loaded onto a 2 % agarose gel. Supernatants were either shock frozen in liquid nitrogen for storage at -80°C or further processed in the next steps.

An antibody to the protein of interest was coupled to 30 μ l of magnetic Dynabeads (protein A and protein G, 1:1). The beads were washed three times with 1 ml of ChIP blocking

Methods

solution (5 mg/ml of BSA in PBS). The beads were resuspended in 500 μ l of ChIP blocking solution. 3 μ g of antibody was added. The mixture was incubated at 4°C for at least 6 hours on a rotating wheel. Beads were washed three times with ChIP Blocking Solution and resuspended in 30 μ L ChIP Blocking Solution per IP. A 1% input was collected before starting the IP. The IP was incubated for at least 6 h at 4°C on a rotating wheel with washed and antibody coupled Dynabeads added to the chromatin.

The beads were transferred to a fresh reaction tube and washed three times: the first time with Wash Buffer I, the second time with Wash Buffer II and the third time with Wash Buffer III. Different salt concentrations were used in these buffers. In order to completely remove the saline buffers, the beads were washed once with TE buffer and the reaction tube was changed. The chromatin was eluted twice with 150 μ l elution buffer by incubation on the rotary wheel for 15 min at room temperature.

Equal volumes of elution buffer were also added to the input samples. To decrosslink the DNA, 160 mM NaCl was added together with 20 μ g/ml RNaseA and the samples were incubated for 1 h at 37 °C and then overnight at 65 °C in a thermoshaker (800 rpm). The next day, 200 μ g/ml Proteinase K was added and the samples were incubated for 2 h at 45 °C in a thermoshaker. DNA was then purified by phenol/chloroform extraction. The DNA was precipitated in 100% EtOH for 30 min at -20 °C. After centrifuging, the pellet was washed twice with 75% EtOH before it was air dried and resuspended in 300 μ L ddH₂O. 10 μ l of chromatin was used in the reaction for quantitative real-time PCR (1.3.3).

3.3.2 RNA extraction and cDNA synthesis

Medium was removed and 1 ml TriFast™ lysis reagent (Peqlab) was added directly to the cell culture dish to isolate total RNA from the cultured cells. The suspension was then homogenised and transferred to a fresh 1.5 ml tube containing the reaction mixture. After the addition of 200 μ L chloroform, samples were vortexed thoroughly and incubated at room temperature for 5 minutes. Samples were centrifuged at 14,000 rpm for 5 min and the upper phase containing RNA was transferred to a new tube containing 1 volume of isopropanol. After incubating at -20°C for 15 min, the tubes were centrifuged at 14,000 rpm for 10 min at 4°C, washed with 70% EtOH and centrifuged. The RNA pellet was air

Methods

dried. It was resuspended in 30 μ l ddH₂O. RNA concentration was determined by NanoDrop.

The total RNA was reverse transcribed to form complementary DNA (cDNA). Up to 2 μ g RNA was diluted in 10 μ l ddH₂O and incubated at 65°C for 1 minute. The reaction was allowed to cool down on ice and the following mixture was added:

- 10 μ l 5x RT buffer (Promega)
- 1 μ l M-MLV reverse transcriptase (200 U/ml, Promega)
- 1.25 μ l dNTPs (10mM, Roth)
- 2 μ L random primer (2 mg/ml, Roche)
- 25.55 μ l ddH₂O

Subsequently, the reverse transcription reaction was performed in a thermocycler for 10 min at 25°C followed by 50 min at 37°C then 15 min at 70°C.

3.3.3 Real-time quantitative PCR (RT–qPCR)

RT–qPCR was used for quantification of the relative mRNA expression levels after cDNA synthesis (1.3.4) or recovered DNA from chromatin immunoprecipitation () for measurement of chromatin enrichment of a specific protein pull-down. A fluorescent dye is incorporated into the freshly synthesized double-stranded DNA, which can be monitored in each cycle after the end of the extension step, allowing the DNA to be quantified in real time. The reaction was set up in the following way:

- 10 μ l cDNA (diluted 1:10)
- 5 μ l SYBR Green Mix (Thermo Fisher Scientific)
- 4 μ l ddH₂O
- 1 μ l mix of forward and reverse primers (stock 10 μ M)

Methods

The measurement was performed on the StepOne™ Real-Time Cycler.

For mRNA qPCRs, all conditions were normalized to the corresponding mRNA of the gene *Vcl*.

3.3.4 Preparation of whole cell lysate and determination of protein concentration

To isolate proteins, cells were washed twice with ice-cold PBS, scraped into a 1.5 ml tube and then pelleted at 1200 rpm for 5 minutes at 4°C. The cell pellet was lysed by the addition of 200 µl of ice-cold RIPA buffer with proteinase and phosphate inhibitors (1:1000) and allowed to stand on ice for 20 minutes. Cell debris was then removed by centrifugation at 14,000 rpm for 5 minutes at 4°C. The supernatant was then aspirated into a new tube. This was snap frozen in liquid nitrogen and stored at -80°C. To determine protein concentration, 1.5 µL of protein sample was mixed with 150 µL of bicinchoninic acid and CuSO₄ solution (50:1) in a 96-well plate. The solution was incubated at 37 °C until the colour change was observed, after which the absorbance at 550 was measured using an appropriate reference. The protein concentration was estimated by comparing the measured values with a BSA calibration curve.

3.3.5 Immunoblotting

The proteins were separated by SDS-PAGE. They were then transferred to a PVDF membrane. In brief, the PVDF was first activated in methanol for a period of 30 seconds and then kept in the transfer buffer. Subsequently, the blotting sandwich was assembled, and air bubbles were removed by a plastic roller. Finally, the transfer was carried out by exposing the sandwich to an electric current of 350 mA for 3 h at a temperature of 4 °C.

After transfer, the membrane was washed once in TBST. It was then blocked at room temperature with a 5% solution of BSA in TBST. The blocked membrane was then incubated with the primary antibody for one night at 4 °C. Subsequently, the membrane was washed in TBST before it was treated with the HRP-conjugated secondary antibody for one hour. After washing with TBST, the Immobilon Western Substrate Kit (Millipore)

was used according to the manufacturer's protocol to visualize the proteins on the LAS-4000 imager (Fujifilm).

3.3.6 Transformation of competent bacteria with DNA plasmid

XL-1 blue, chemically competent bacteria were thawed on ice. They were mixed with either 1 µg DNA or the ligation mix. They were incubated for 30 minutes on ice, followed by heat shock at 42°C for two minutes and cooling on ice. The samples were mixed with 1 ml of LB medium without antibiotics and incubated for 30 min at 37 °C in a thermoshaker (200 rpm) before being plated on LB agar plates containing the appropriate antibiotics. The bacterial suspension was centrifuged for a short time, resuspended in 50 µl of LB medium and the complete reaction was plated. The LB agar plates were incubated overnight at 37 °C. The next day, single colonies were picked and incubated in 3 ml LB medium with the appropriate antibiotics in a shaking incubator. The temperature should be adjusted according to the vector used.

3.3.7 Bacterial plasmid DNA preparation for analysis (miniprep)

For the analytical preparation of plasmid DNA, alkaline lysis was performed. 1.5 ml of overnight culture was centrifuged, and the bacteria were resuspended in 200 µl Mini Buffer I containing 100 µg/ml RNaseA. The lysis was carried out in Mini Buffer II and the bacteria were incubated for 3 minutes at room temperature. After the addition of Mini Buffer III, the lysis was stopped by precipitation. Samples were centrifuged at 14,000rpm for 5min at room temperature. The supernatant was mixed with 500µl isopropanol in a fresh 1.5ml tube and incubated at -20°C for 15 minutes. The plasmid DNA was pelleted by centrifugation at 14,000 rpm at 4 °C. The pellet was washed with 70% EtOH, air dried and resuspended in 20 µl ddH₂O. Further analysis was carried out by restriction digesting.

3.3.8 Plasmid DNA Isolation (Maxiprep)

The PureLink® HiPure Plasmid Maxiprep Kit was used to process 200 ml of overnight culture consisting of LB medium with appropriate antibiotics and the remainder of the

overnight pre-culture that was not used in the miniprep (1.3.2). Purified plasmid DNA was resuspended in TE buffer.

3.4 Next generation sequencing methods

3.4.1 ChIP-sequencing

The protocol was carried out as described in section 3.3.1, with few modifications. $20 \cdot 50 \cdot 10^6$ cells were used per IP for cell culture. The DNA pellet was solubilised in 30 μ l ddH₂O using 100 μ l Dynabeads and 10-15 μ g antibody for the IP step. To test the efficiency of ChIP, 3 μ l of this DNA was mixed with 130 μ l ddH₂O and RT-qPCR was performed. To perform spike-in ChIP sequencing (ChIP-Rx), 10% fixed U2OS cells were added to the murine KPC cells at the step of Lysis Buffer I. Library was prepared using NEBNext Ultra II DNA Library Prep Kit for Illumina using manufacturer's protocol.

3.4.2 CUT&RUN-sequencing

The protocol was performed as previously described (Meers *et al*, 2019). Briefly, KPC cells were harvested using Accutase (Sigma). Cells were washed three times by adding 1 ml of wash buffer (20 mM HEPES pH 7.5, 150 mM NaCl, 0.5 mM spermidine) followed by centrifugation (3 min, 600 g, RT). Cells were coupled to concanavalin A-coated magnetic beads (Polysciences Europe) by incubation in 1 ml wash buffer supplemented with 10 μ L bead slurry per sample, prewashed with 1 ml binding buffer (20 mM HEPES pH 7.5, 10 mM KCl, 1 mM CaCl₂, 1 mM MnCl₂), for 10 min at room temperature (RT) with rotation. After magnetic separation of the bead-coupled cells, the supernatant was removed and replaced with 150 μ l Dig-wash buffer (wash buffer supplemented with 0.05% digitonin) containing 2 mM EDTA to permeabilize the cells. 3 μ g of MYC Y69 antibody (abcam) was added per sample and incubated overnight at 4°C with shaking (800 rpm). The next day, the cells were washed twice with 1 mL of Dig-Wash buffer. The cells were then incubated with Protein A/G-MNase fusion protein at a concentration of 1 μ g/mL diluted in 150 μ L of Dig-Wash buffer for 1 hour at 4°C (800 rpm). Cells were washed twice with 1 mL of Dig-Wash buffer followed by 1 mL of low salt rinse buffer (20 mM HEPES

Methods

pH 7.5, 0.05% digitonin, 0.5 mM spermidine). After removal of the low salt rinse buffer, the MNase coupled to the primary antibodies was activated by adding 200 µl of ice-cold incubation buffer (3.5 mM HEPES pH 7.5, 10 mM CaCl₂, 0.05% digitonin) and incubated for 30 min on ice. To stop the reaction, 200 µl of STOP buffer (170 mM NaCl, 20 mM EGTA, 0.05% digitonin, 50 µg/ml RNase A, 25 µg/ml glycogen) was added and samples were incubated at 37°C for 30 min to release MNase-cleaved DNA fragments from insoluble nuclear chromatin. For protein digestion, SDS and proteinase K were added at a concentration of 0.1% and 250 µg/ml, respectively, and incubated at 50°C for 1 h. DNA was isolated by phenol-chloroform extraction and quantified by determining the concentration of small fragments (7-50 bp) on the Fragment Analyzer (Agilent). Libraries were prepared using the NEBNext Ultra II DNA Library Prep Kit for Illumina according to the manufacturer's protocol.

3.4.3 mRNA-sequencing

peqGOLD TriFast (PeqLab) was used for RNA isolation. Total RNA was extracted using miRNeasy kit (QIAGEN) including on-column DNase I digestion. The Fragment Analyser was used to determine the RNA Quality Number (RQN). A minimum RQN of 9 was required for the RNA used for sequencing. After quality analysis, 1 µg of RNA was used for mRNA isolation using NEBNext® Oligo d(T)25 beads according to the NEBNext® Poly(A) mRNA magnetic isolation module and library preparation using NEBNext Ultra II Directional RNA Library Prep Kit for Illumina according to instructions. Size selection of the libraries was performed using Agentcourt AMPure XP Beads (Beckman Coulter), followed by amplification with 11 cycles of PCR.

3.4.4 BLISS

BLISS was performed as described before (Endres *et al.*, 2021). Cells were fixed with 3.7% v/v paraformaldehyde and washed with PBS. Lysis was performed by incubation in lysis buffer 1 (10 mM Tris-HCl, 10 mM NaCl, 1 mM EDTA, 0.2% Triton X-100, pH 8) for 1h at 4C, followed by a brief rinse in PBS and incubation in lysis buffer 2 (10 mM Tris-HCl, 150 mM NaCl, 1 mM EDTA, 0.3% SDS, pH 8) for 1h at 37C. After rinsing in PBS,

Methods

cells were equilibrated in CutSmart buffer (New England Biolabs) before double-strand breaks were blunted using the Quick Blunting Kit (New England Biolabs) according to the manufacturer's protocol. After PBS rinse and before blunting, AsiSi (New England Biolabs) digestion was performed according to the manufacturer's instructions. Sense and antisense adaptor oligos were annealed by heating at 95°C for 5 minutes, followed by a gradual cooling to 25°C over a period of 45 minutes. Following equilibration in CutSmart buffer (New England Biolabs) and T4 Ligase buffer (New England Biolabs), annealed adapters were applied to samples and ligated with T4 DNA Ligase (New England Biolabs) for 16h at 16°C according to the manufacturer's recommendations. Excess adapters were removed by repeated rinses in high salt wash buffer (10 mM Tris-HCl, 2 M NaCl, 2 mM EDTA, 0.5% Triton X-100, pH 8). Genomic DNA was extracted in DNA extraction buffer (1% SDS, 100 mM NaCl, 50 mM EDTA, 10 mM Tris-HCl, pH 8) supplemented with Proteinase K (1 mg/ml, Roth) for 16h in a thermoshaker at 55°C. DNA was isolated by phenol-chloroform extraction and isopropanol precipitation, resuspended in TE buffer and sonicated with a Covaris Focused Ultrasonicator M220 for 1 to 2 min to obtain a fragment size of 300-500 bp. Fragment size was determined on the Fragment Analyzer (Agilent) using the NGS Fragment High Sensitivity Analysis Kit (1-6,000 bp; Agilent). DNA was concentrated using Agencourt AMPure XP Beads (Beckman Coulter), transcribed into RNA, and DNA digested using the MEGAscript T7 Transcription Kit (Thermo Fischer Scientific) according to the manufacturer's recommendations. RNA purification was performed using Agencourt RNAClean XP Beads (Beckman Coulter). RNA concentration was determined on the Fragment Analyzer (Agilent) using the Standard Sensitivity RNA Analysis Kit (Agilent). Library preparation was performed by ligation of the RA3 adaptor to samples using T4 RNA Ligase 2 (New England Biolabs) supplemented with recombinant ribonuclease inhibitor (Thermo Fischer Scientific). Samples were reverse transcribed using SuperScript III Reverse Transcriptase Kit (Thermo Fisher Scientific), and library indexing and amplification were performed using NEBNext High-Fidelity 2X PCR Master Mix (New England Biolabs) with RP1- and desired RPI-primer. Libraries were purified using Agencourt AMPure XP Beads (Beckman Coulter), quality, quantity, and fragment size assessed on the Fragment Analyzer (Agilent) using the NGS Fragment High Sensitivity Analysis Kit (1- 6,000 bp; Agilent), and

Methods

then subjected to Illumina sequencing according to the manufacturer's instructions. Adapters and oligos were custom synthesized, and unique molecular identifiers (UMIs) were generated by random incorporation of the four standard dNTPs using the 'Machine mixing' option.

3.4.5 4sU sequencing

Subconfluent cells were treated as described. During the last 15 min of treatment, cells were incubated with 2mM 4-thiouridine (4sU; Sigma-Aldrich) before lysis with QIAzol reagent (QIAGEN). Total RNA extraction was performed using the miRNeasy kit (QIAGEN) with on-column DNase digestion, and RNA quantity and quality were assessed using a Nanodrop spectrophotometer and a Fragment Analyzer (Thermo Fisher Scientific), respectively. 20-40 µg of RNA with RQN values greater than 9 was then biotinylated by adding EZ-Link Biotin-HPDP (Pierce) in 0.2 mg/ml dimethylformamide and biotin labeling buffer (10 mM Tris pH 7.4, 1 mM EDTA) and incubating for 2h at RT with rotation. Biotinylated RNA was then purified by chloroform isoamyl alcohol extraction in MaXtract high-density tubes (QIAGEN). The upper aqueous phase was collected and 1/10 volume of 5 M NaCl and an equal volume of isopropanol were added. All samples were centrifuged at 20,000g for 20 min at 4°C, the RNA pellets were washed with 75% ethanol and centrifuged at 20,000g for 10 min at 4°C. After drying, the pellets were resuspended in nuclease-free water. Biotinylated RNA samples were then eluted using Dynabeads MyOne Streptavidin T1 beads (Invitrogen) in Dynabeads Wash Buffer (2 M NaCl, 10 mM Tris pH 7.5, 1 mM EDTA, 0.1% v/v Tween 20) for 15 min at RT with rotation. After stringent washing, 4sU-labeled RNA was eluted from the beads with 100 ml of freshly prepared 100 mM DTT in nuclease-free water and purified using the RNeasy MinElute Kit (QIAGEN). Samples were quantified using the RiboGreen Assay (Invitrogen), and 5-20 ng RNA was used for cDNA library preparation by first depleting rRNA using the NEBNext rRNA Depletion Kit (Human/Mouse/Rat) (New England Biolabs) and then the NEBNext Ultra II Directional RNA Library Prep Kit (New England Biolabs). cDNA libraries were amplified using appropriate multiplexed index primers in 11-14 cycle PCR, depending on the amount of RNA input.

3.5 Bioinformatics

ChIP-sequenced libraries were mapped separately to the mouse mm10 genome and human hg19 (spike-in) using Bowtie 2 v2.3.4.1 with default parameters. ChIP-Rx spike-in normalization was performed by calculating a spike-in normalization factor by dividing the number of mapped reads from the spike-in of the smallest sample by the number of mapped reads from the spike-in of each sample. For each sample, this factor was multiplied by the number of reads that mapped to the mouse genome. All bam files for subsequent analysis were adjusted to this read count using Samtools was used to manipulate the bam files (indexing and subsampling). To visualize the read alignments on the Integrated Genome Browser v9.1.10, the BAM files were converted to bigwig files using Deeptools without further normalization and a bin size of 10 bases. Heat map (Figure 4.8 c) was generated by applying the computeMatrix operation to all expressed genes (at least 10 reads mapped per gene based on mRNA sequencing), followed by the plotHeatMap function in Deeptools. Heat maps (Figure 4.10 c & 4.13 b) were generated using the bamCompare function first, followed by plotHeatMap in Deeptools.

CUT&RUN libraries were mapped to the mouse mm10 genome using default parameters with Bowtie 2 v2.3.4.1. Samples were read-normalized using the number of reads in the smallest sample. BAM files were converted to bigwig files using Deeptools with no further normalization and a bin size of 10 bases. Metagene plot (Figure 4.8 d) were generated by applying the computeMatrix operation to all expressed genes (centered on the TSS), followed by the plotProfile function in Deeptools.

For mRNA-seq, reads were mapped to mm10 using Bowtie 2 v2.3.4.1, then samples were normalized to the number of mapped reads in the smallest sample. Reads per gene were counted using the featureCounts function from the R package Rsubread. Non- and low-expressed genes with less than 5 reads per gene were removed. Differentially expressed genes were retrieved using edgeR, and *P* values were adjusted for multiple testing using the Benjamini-Höchberg procedure. Gene set enrichment analysis was performed using the Hallmark databases of MSigDB. Go terms were identified using Gostats and enrichR packages in R. In Figure 4.10 c, differential gene expression was calculated based on

Methods

reads mapping only to the second half of the gene. In Figure 4.9 c, downregulated genes in the DNA repair GO term (GO-0006281) were selected based on a $\log_2FC < 0$ and $FDR < 0.05$.

For BLISS, samples were demultiplexed based on their condition-specific barcodes using UMI-tools v1.0.1, allowing for one mismatch in the barcode, and mapped separately to the mouse reference genome (mm10) using Bowtie2 v2.3.4.1. For BLISS normalization, AsiSI-specific restriction sites were generated by *in silico* digestion of the mm10 genome, followed by counting deduplicated reads in AsiSI-specific restriction sites using countBamInGRanges from the R package exomeCopy. The sample with the lowest number of AsiSI-specific reads was divided by the number of corresponding reads from each sample. The resulting ratio was multiplied by the total number of deduplicated reads, and samples were then randomly subsampled to the calculated number of reads. For the data in Figure 4.2 d, AsiSI-normalized mapped reads were annotated to the respective described genomic region using ChIPseeker v1.34.1 in R v4.2.2.

For the analysis of the 4sU sequencing experiment, reads were mapped to the mouse reference genome (mm10) with Bowtie 2 v2.3.4.1. Reads mapping to exons and regions in the ENCODE Blacklist were removed from BAM files using bedtools v2.26.0. Samples were then normalized by the bamCoverage function in deepTools using counts per million mapped reads, and then bigwig files were generated. For the metagene quartile plots in Figure 4.10 a, expressed genes were stratified based on their length from quartile 1 (shortest) to quartile 4 (longest), where each quartile consists of 2091 genes, except quartile 4 with 2092 genes. Since only intronic 4sU reads were considered; thus, genes shorter than 10 kb were excluded from the analysis, as very short genes have a very low number of reads after filtering for exons.

3.6 Immunohistochemistry

Samples were paraffin-embedded and sectioned at 6 μm using a microtome (Leica) for immunohistochemical analysis. Sections were deparaffinized, rehydrated and subjected to high temperature antigen retrieval at pH 6 for all stains, except for pKAP1 at pH 9.

Methods

Detection of the primary antibodies was performed using appropriate secondary antibodies coupled to peroxidase. Hematoxylin was used to counterstain sections. Staining was imaged using a Pannoramic DESK scanner. Analysis was performed using QuPath (Bankhead *et al.*, 2017)

4 Results

4.1 MYC prevents transcription-replication conflicts in PDAC cells

MYC has two important functions in pancreatic ductal adenocarcinoma: First, it ensures efficient progression through S-phase (Krenz *et al.*, 2021). Second, MYC is required for enabling tumor cells to evade recognition and elimination by the host immune system (Krenz *et al.*, 2021; Muthalagu *et al.*, 2020; Sodir *et al.*, 2020). In this part of the dissertation, the effects of MYC depletion on the cell cycle and the underlying mechanism were investigated.

4.1.1 MYC is required for genomic stability during S-phase

To characterize the effect of MYC on S-phase in PDAC, tumor cell line derived from the “KPC” mouse model was used. Tumors derived from this model were induced by simultaneous expression of TP53^{R172H} and KRAS^{G12D} in pancreatic progenitor cells by Cre-mediated recombination. Efficient depletion of MYC was achieved by the expression of two shRNA targeting *Myc* as described previously (Figure 4.1 a) (Krenz *et al.*, 2021). To characterize the effect of MYC on cell cycle progression, quantitative image-based cytometry (QIBC) was used. In this assay, DNA content and replication were estimated based on Hoechst staining and EdU incorporation respectively. MYC depletion resulted in a decrease in the percentage of cells in S-phase (Figure 4.1 b). Interestingly, cells in S-phase incorporated less EdU, suggesting that overall DNA replication is perturbed. To find a possible explanation for this phenotype, I performed a co-staining with gamma-H2AX (γ -H2AX), a marker of double-strand break formation. Depletion of MYC led to an increase in γ -H2AX intensity, which occurred mainly in S-phase cells. (Figure 4.1 c, d). These results suggest that MYC ensures genomic stability during S-phase.

Results

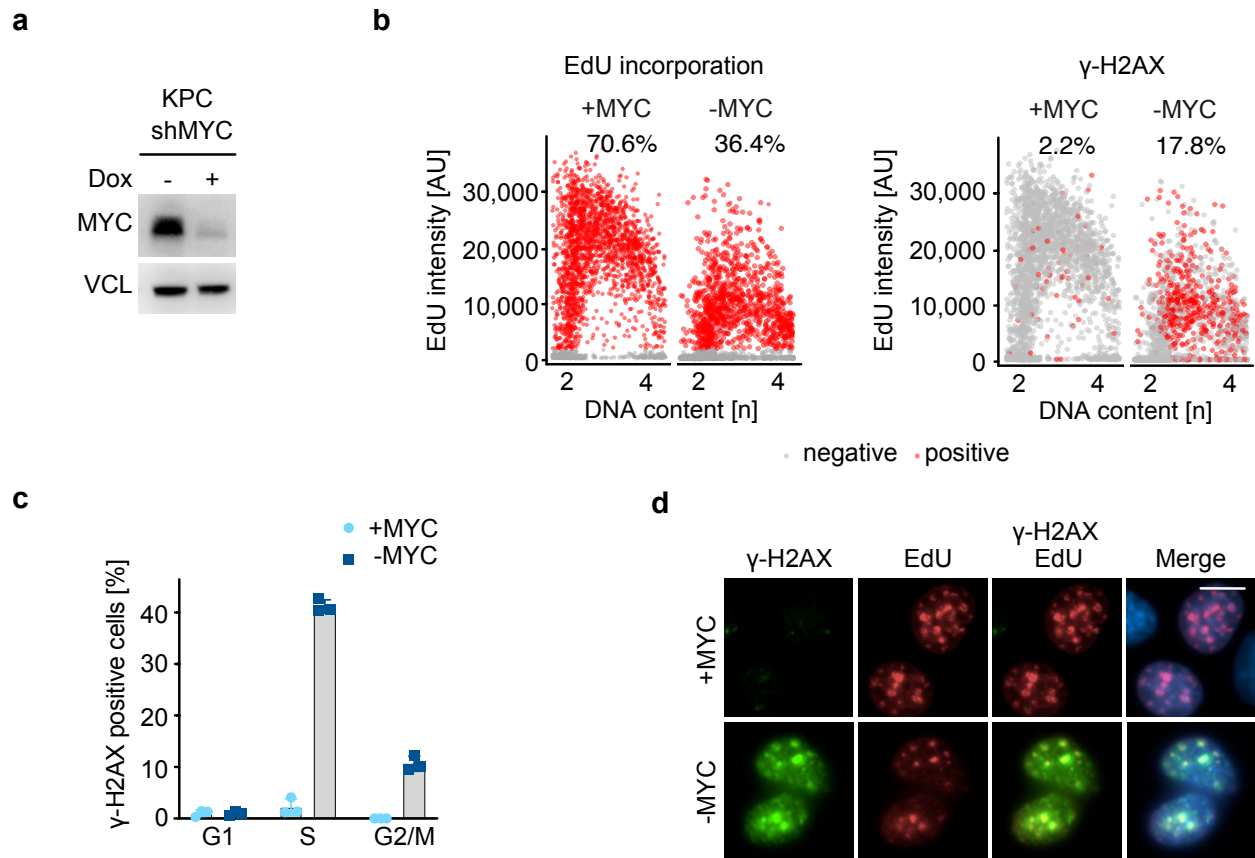


Figure 4. 1: MYC prevents DNA damage during S-phase

a. Immunoblot showing MYC expression in KPC cells. Where indicated, doxycycline (Dox) (1 μ g/ml) was added for 48 h. Vinculin was used as a loading control.

b. Quantitative image-based cytometry showing DNA content on the x-axis and EdU incorporation on the y-axis, with either EdU (left) or γ -H2AX (right) positive cells highlighted in red, for cells carrying doxycycline-inducible shRNA targeting *Myc*. Hereafter, "-MYC" indicates samples in which MYC depletion was induced by the addition of doxycycline (1 μ g/ml) for 48h, and "+MYC" indicates the corresponding control (treated with ethanol). n=3 (n: number of independent experiments, unless otherwise indicated).

c. Bar graph showing the percentage of γ -H2AX-positive cells in each cell cycle phase derived from (b). Data are expressed as mean \pm s.d. (n=3).

d. Representative immunofluorescence images used for the analysis shown in (b). The merged image includes all stains, including Hoechst for nuclear labeling. Scale bar: 10 μ m.

Parts of this figure may be published in a similar form in Gaballa et al., *Manuscript under consideration*.

4.1.2 MYC prevents transcription-replication conflicts

DNA damage occurring in S-phase is indicative of TRCs. To test this hypothesis, I performed proximity ligation assay (PLA). This assay evaluates the proximity between the

Results

RNAPII and either proliferating cell antigen (PCNA), which forms the sliding clamp of active replication forks, or RAD9, which replaces PCNA at stalled replication forks as part of the 9-1-1 complex (Yan & Michael, 2009). MYC depletion induced an increase in proximity in both assays, suggesting that endogenous MYC prevents TRCs (Figure 4.2 a). Since TRCs induce the activation of the ATR kinase to allow stabilization of stalled replication forks (Hamperl *et al.*, 2017; Saldivar *et al.*, 2017), the combination of MYC depletion and ATR inhibition was tested. AZD6738, a specific ATR inhibitor (Kwok *et al.*, 2015), was used for this purpose. ATR inhibition caused a weak increase in phosphorylation of KAP1 at serine 824, a substrate of the ATM kinase that is activated by double-strand breaks (Ziv *et al.*, 2006), but caused a much stronger increase upon MYC depletion (Figure 4.2 b). To better understand this phenotype, I performed BLISS sequencing of the double-strand breaks. Consistently, quantification of the number of double-strand breaks showed that MYC depletion caused a significant increase upon ATR inhibition. Bioinformatic analysis revealed that most of the double-strand breaks occurred in transcribed regions, consistent with previous observations (Endres *et al.*, 2021), as well as in distal intergenic regions. Taken together, these results demonstrate that endogenous MYC limits TRCs and the resulting DNA damage that occurs during S-phase.

Results

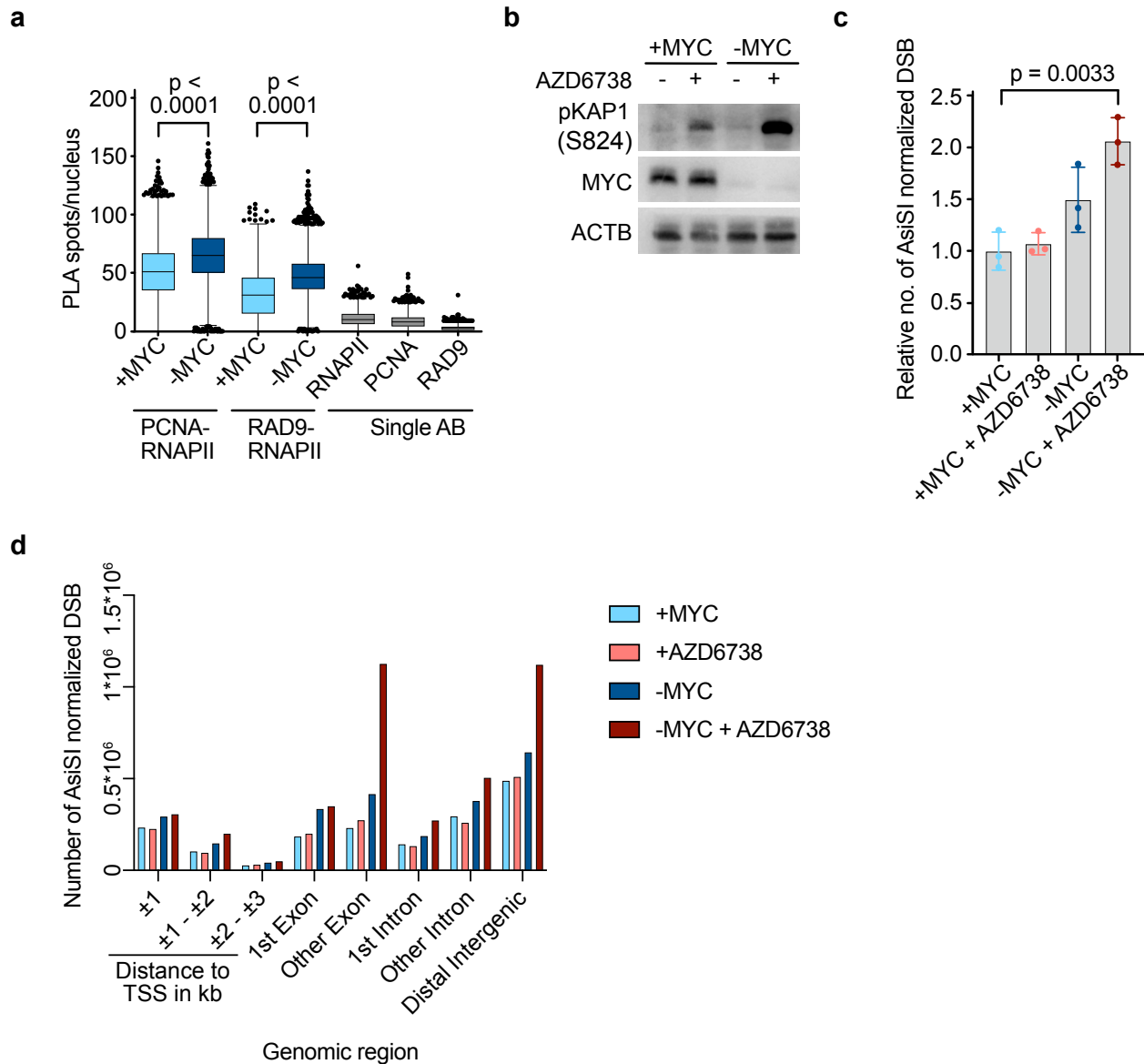


Figure 4. 2: MYC prevents transcription replication conflicts

a. Single cell quantification of nuclear PLA foci between either PCNA or RAD9 and total RNAPII. Single antibody controls are shown in gray for the +MYC condition. (n=3; two-tailed Mann-Whitney *U*-test; single antibody n=1).

b. Immunoblot of cells with doxycycline-inducible shRNA targeting *Myc*. MYC depletion was induced as in (a) and AZD6738 treatment was performed for 48h at 0.3 μ M concentration. Actin-beta was used as loading control (n=2).

c. Bar graph showing the relative number of AsiSI-normalized reads quantifying double-strand breaks as determined by BLISS sequencing. Doxycycline was added for 48 hours to induce MYC depletion, and AZD6738 (2 μ M) was used for 2 hours where indicated. Data are presented as mean \pm s.d. (n=3; unpaired two-tailed *t*-test).

d. Bar graph showing the number of AsiSI-normalized reads quantifying double-strand breaks at different genomic regions indicated. All biological replicates were pooled and shown in this graph (n=3). Experimental conditions are the same as in Figure 4.2c.

Parts of this figure may be published in a similar form in Gaballa et al., *Manuscript under consideration*.

4.2 An siRNA screen identifies the PAF1c as a regulator of genomic stability

4.2.1 Target selection strategy for the siRNA library.

The results in section 4.1 suggest that MYC ensures S-phase progression, limits DNA damage upon ATR inhibition and prevents TRCs. Therefore, potential downstream factors of MYC were screened to identify those that are responsible for these phenotypes. In addition, factors involved in R-loop resolution, polyadenylation, and promoter-proximal transcription, which can limit TRCs (Hamperl & Cimprich, 2016), were also included in the siRNA screen (Figure 4.3).

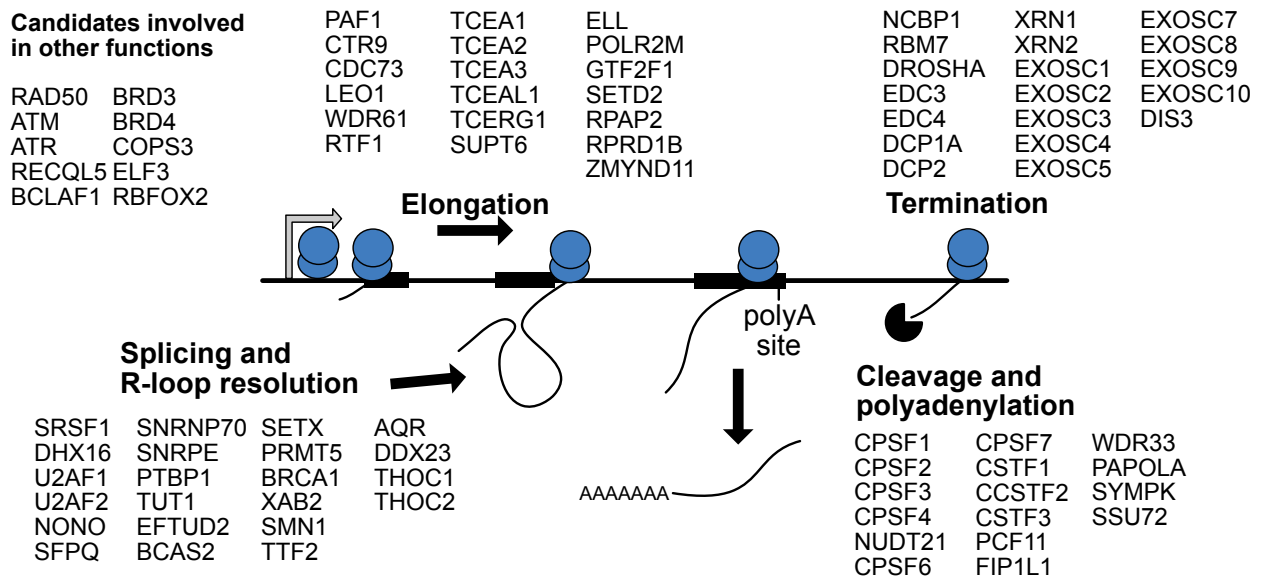


Figure 4. 3: Scheme illustrating siRNA targets and their function.

Parts of this figure may be published in a similar form in Gaballa et al., *Manuscript under consideration*.

Results

4.2.2 Set-up of the siRNA screen

For the siRNA screen, immunofluorescence-based readouts were used to assess S-phase progression and DNA damage induction with or without ATR inhibition. Three parameters were selected for this purpose. First, EdU incorporation was measured to assess efficient DNA replication (Figure 4.4, left). Second, phosphorylation of KAP1 at serine 842 (pKAP1(S824)) was examined as an indicator of double-strand breaks (Figure 4.4, middle). Third, the enhancement of ATR inhibition to induce pKAP1(S824) was examined (Figure 4.4, right). Example hits from the siRNA screen are shown for each readout, along with the thresholds used and example images (Figure 4.4).

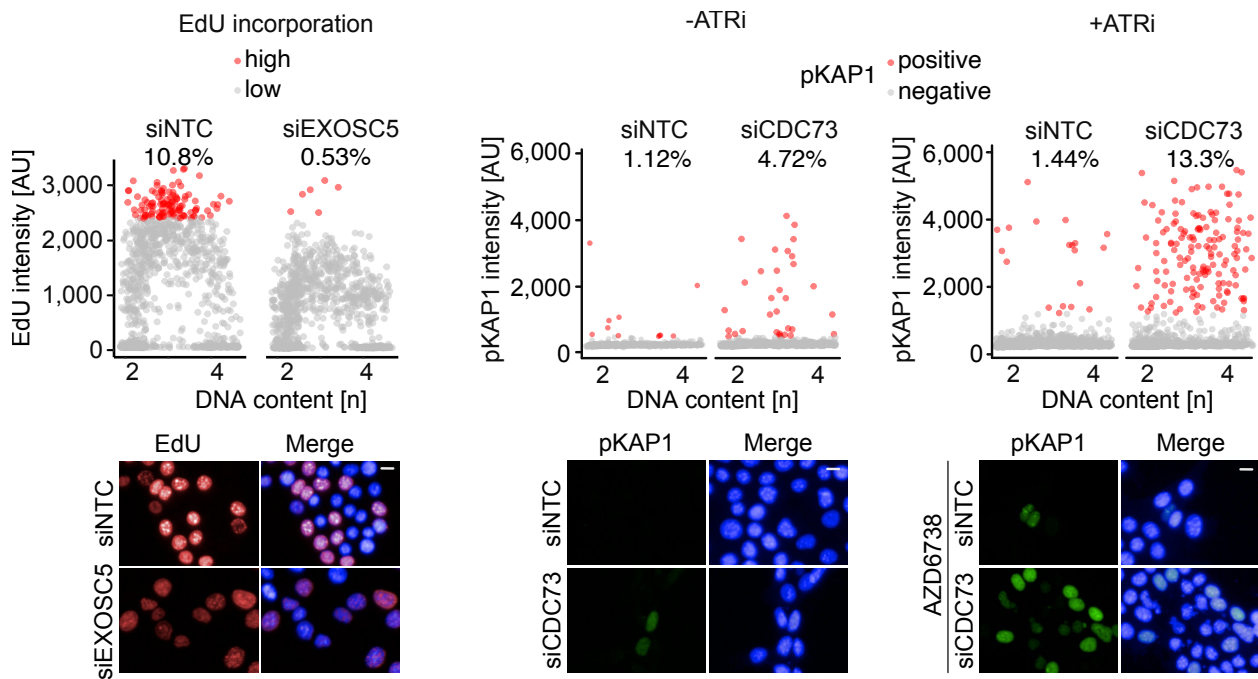


Figure 4. 4: Example hits from the siRNA screen

Quantitative image-based cytometry with DNA content shown on the x-axis. Left: EdU intensity plotted on the y-axis. Center: pKAP1(S824) intensity shown on the y-axis. Right: pKAP1(S824) intensity after incubation with AZD6738 (0.1 μM; 24h). For each parameter, an example of a hit siRNA is shown. Representative images are shown below. Scale bar: 10 μm. siRNA transfection was performed for 48h and EdU was added 30 min before fixation (n=3). Parts of this figure may be published in a similar form in Gaballa et al., *Manuscript under consideration*.

4.2.3 Hits of the siRNA screen

The different readouts of the siRNA screen were then analyzed. In the first readout, which analyzed the induction of DNA damage signaling marked by phosphorylation of KAP1, several known regulators of genomic stability such as AQR and ATR were scored as hits (Saldivar *et al.*, 2017; Sollier *et al.*, 2014) (Figure 4.5 a). In the second readout, analysis of pKAP1 levels upon incubation with a low dose of ATR inhibitor was investigated. Interestingly, 3 subunits of PAF1c scored as hits in this readout (Figure 4.5 b). In the third readout, the measurement of DNA replication efficiency was estimated by EdU incorporation. In this assay, 4 subunits of PAF1c scored positive (Figure 4.5 c). The overlap of the different readouts showed that 3 of the PAF1c subunits were present in at least 2 of the 3 different readouts.

Results

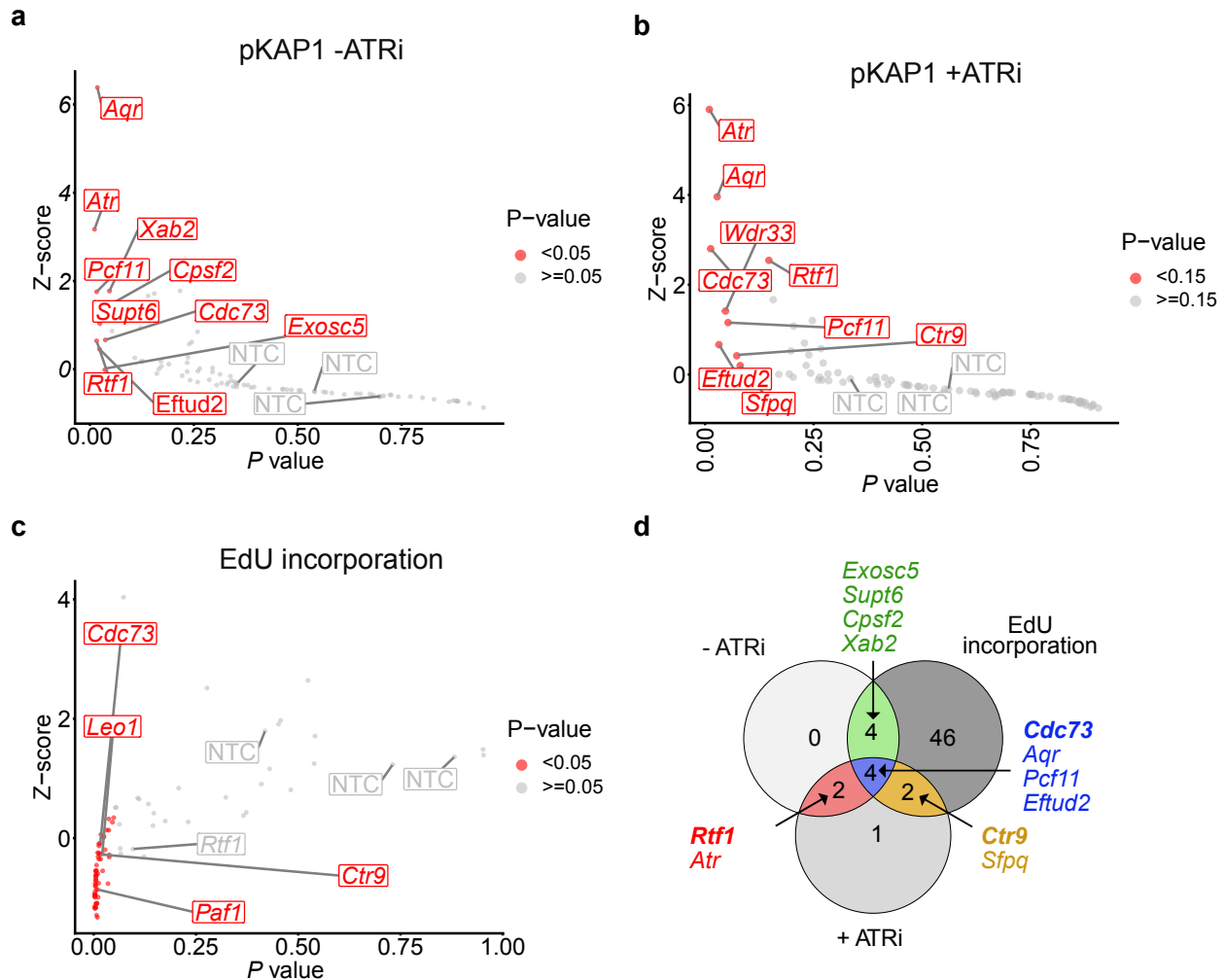


Figure 4. 5: siRNA screen hits

a. Scatter plot showing siRNA target genes with Z-score (based on pKAP1(S824) positive percentage cells) on the y-axis and P value on the x-axis. Annotated are positive hits and the non-targeting control (siNTC). One-sided t-test was performed to calculate P values with the likelihood of siRNA targeting a candidate to increase pKAP1 signal than siNTC ($n=3$).

b. Same as in a, but upon incubating the cells with AZD6738 (0.1 μ M, 24 h). One-sided t-test was performed to calculate P values with the likelihood of siRNA targeting a candidate to increase pKAP1 signal than siNTC ($n=2$).

c. Same as in a, with Z-score calculated based on percentage of EdU high cells (Figure 4.4, left). Annotated are subunits of the PAF1c and siNTC.

P values were calculated using unpaired two-sided t -test ($n=3$).

d. Venn diagram showing the overlap between hits of different read-outs. Labeled are the names of targets scoring in at least 2 of the 3 read-outs.

Parts of this Figure may be published in a similar form in Gaballa et al., *Manuscript under consideration*.

4.2.4 PAF1c maintains genomic stability during replication stress

Since subunits of PAF1c scored as hits in the siRNA screen, I performed validation experiments using shRNA-mediated knockdown. Doxycycline-inducible shRNAs targeting *Cdc73*, *Ctr9* and *Rtf1* were stably integrated into the genome of KPC cells. Indeed, depletion of these subunits synergized with a low dose of ATR inhibitor to induce DNA damage, mimicking MYC depletion (Figure 4.6 a). Depletion of the CTR9 subunit only moderately affected cell proliferation, but completely suppressed proliferation when incubated with a low dose of ATR inhibitor (Figure 4.6 b). These data suggest that PAF1c plays an important role in the maintaining genomic stability particularly during replication stress induced by low dose of ATR inhibitor. PAF1c has been shown to limit transcription-replication conflicts in yeast (Poli *et al.*, 2016). To test whether PAF1c affects the rate of TRCs, PLAs were performed. Depletion of either CTR9 or CDC73 did not significantly affect the number of TRCs, as indicated by the proximity between RAD9 and total RNAPII (Figure 4.6 c). These data suggest that PAF1c does not affect the basal level of TRCs, but rather limits DNA damage during replication stress, as suggested by the data in Figure 4.6.

Results

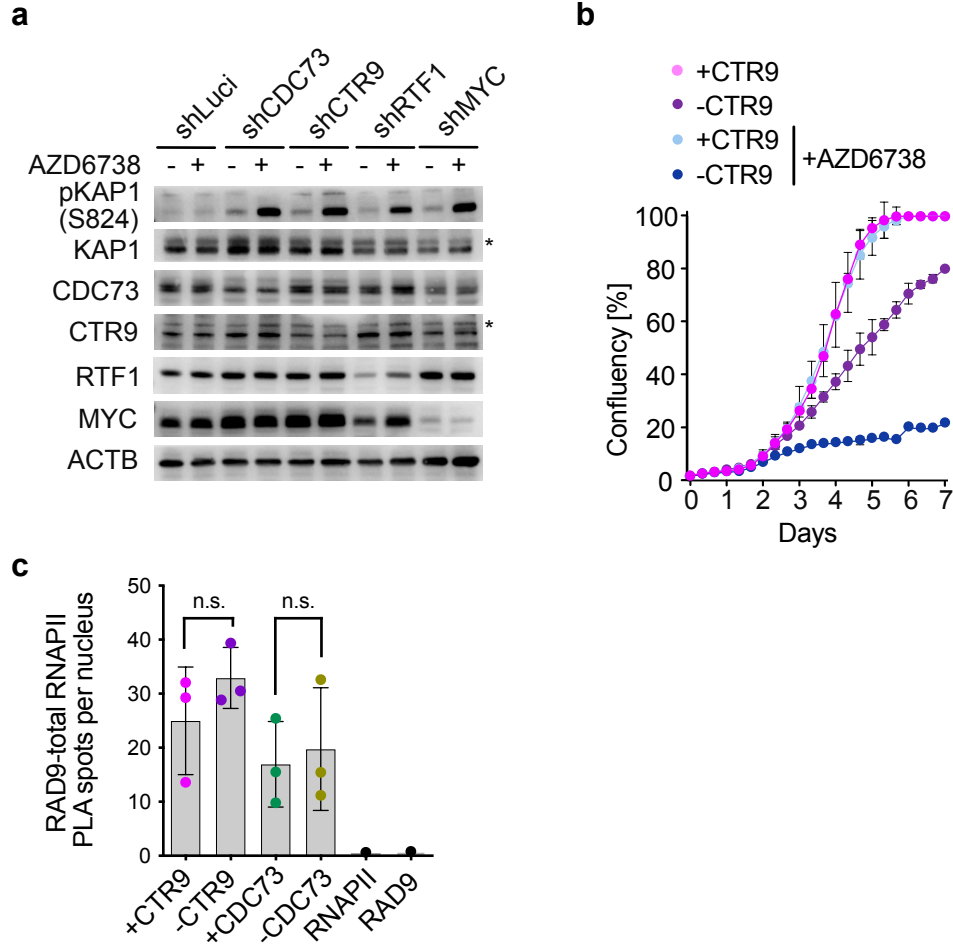


Figure 4. 6: Validation of siRNA screen hits

a. Immunoblot of cells harboring doxycycline-inducible shRNA targeting luciferase, components of PAF1c and *Myc*. Depletion was induced by addition of doxycycline for 72h and treatment with AZD6738 for 72h at a concentration of 0.2 μ M. Beta-actin was used as a loading control (n=3).

b. Incubated cell growth curve for cells carrying doxycycline-inducible shRNA targeting *Ctr9*. CTR9 depletion was induced by the addition of doxycycline (1 μ g/ml) and AZD6738 at a concentration of 0.5 μ M. Data are expressed as mean \pm s.d. (n=2).

c. Bar graphs quantifying the number of nuclear PLA foci between RAD9 and total RNAPII. Data are presented as mean \pm s.d. (n=3; unpaired two-tailed *t*-test, n=1 for single antibody controls).

Parts of this figure may be published in a similar form in Gaballa et al., *Manuscript under consideration*.

4.3 PAF1c is a downstream factor of MYC but is largely dispensable for the regulation of MYC target genes

4.3.1 siRNA screen targeting factors downstream of PAF1c

To better understand how PAF1c promotes genomic stability during replication stress and the mechanism behind its synergy with ATR inhibitor in inducing DNA damage, a second siRNA screen was performed targeting factors downstream of PAF1c. Since PAF1c has multiple functions during transcription (Francette *et al.*, 2021), including elongation by RNAPII (Vos *et al.*, 2018a), promotion of promoter proximal double-strand break repair (Endres *et al.*, 2021), and transcription termination (Liu *et al.*, 2022), factors in these categories downstream of PAF1c were included in the screen. The increase in DNA damage upon incubation with a low dose of ATR inhibitor was used as a readout (Figure 4.7 a). The CDC73 and RTF1 subunits of PAF1c were scored as positive hits. Consistently, HUWE1, which mediates the transfer of PAF1c from MYC to RNAPII, scored positive (Endres *et al.*, 2021). In addition, Cyclin K and its associated kinase CDK12 as well as CDK9 scored positive. CDK9 contributes to the recruitment of PAF1c to RNAPII, which then recruits CDK12 to regulate pause release and transcriptional elongation (Yu *et al.*, 2015). PAF1c bound to BRE1A/B (RNF20, RNF40) recruits RAD6A/B (UBE2A and UBE2B) to ubiquitylate histone H2B at lysine 120 (Kim *et al.*, 2009; Kim & Roeder, 2009; Van Oss *et al.*, 2016). This ubiquitylation allows for chromatin relaxation and recruitment of DNA repair factors, allowing for timely DNA repair (Moyal *et al.*, 2011). Depletion of these factors did not increase DNA double-strand break formation upon ATR inhibition compared to control. Similarly, depletion of INO80, which removes RNAPII during TRCs in yeast, did not score positive (Poli *et al.*, 2016). Validation experiments confirmed that depletion of RNF20 strongly reduced H2B ubiquitylation at lysine 120, with no detectable effect on KAP1 phosphorylation in the presence or absence of ATR inhibitor (Figure 4.7 b). Taken together, these data suggest that the function of PAF1c during transcription elongation may explain the phenotypes observed in section 4.2.

Results

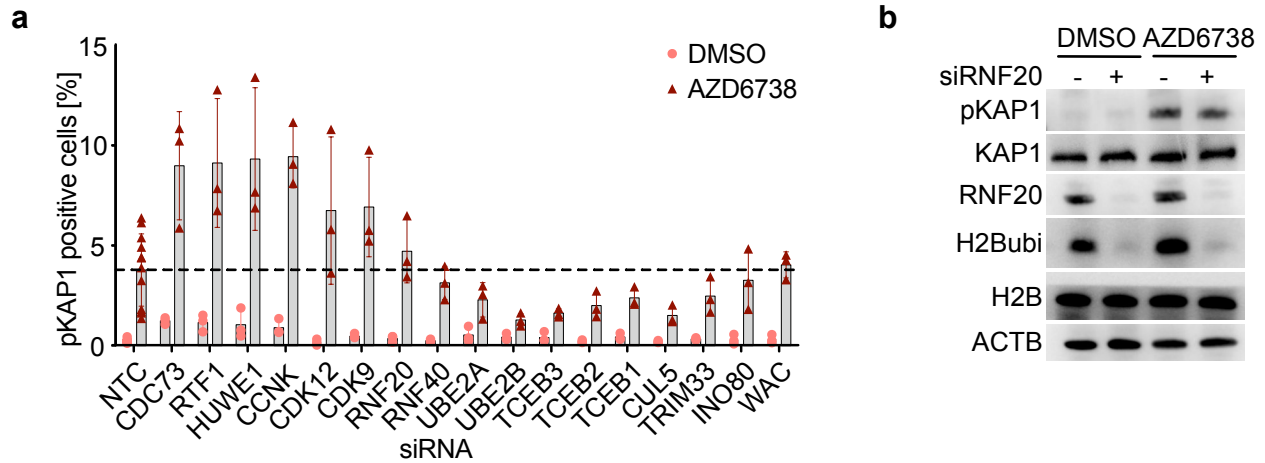


Figure 4. 7: siRNA screen targeting PAF1c downstream factors.

a. Bar graph showing the percentage of cells with pKAP1(S824)-positive nuclei. siRNAs were transfected 48 hours before fixation and AZD6738 was added for 24 hours at 0.1 μ M concentration where indicated. Data are presented as mean \pm s.d. (n=3 for all siRNAs except siNTC, n=12).

b. Immunoblot documenting the levels of the indicated proteins or post-translational modifications 48 h after siRNA-mediated depletion of RNF20 in KPC cells in the presence or absence of AZD6738 (0.2 μ M; 72 h) (n=3).

Parts of this figure may be published in a similar form in Gaballa et al., *Manuscript under consideration*.

4.3.2 MYC-dependent recruitment of CTR9 to the RNAPII is largely dispensable for the regulation of MYC target genes

Previous work has shown that MYC directly binds to PAF1c and enhances its recruitment to RNAPII (Endres *et al.*, 2021). To test whether endogenous MYC is required for PAF1c recruitment to RNAPII in KPC cells, PLA was performed. Consistent with previous findings, depletion of MYC decreased the proximity between CTR9 and RNAPII phosphorylated at serine 5, suggesting that MYC is required for the transfer of CTR9 to RNAPII (Figure 4.8 a).

Next, the effect of PAF1c on MYC-dependent transcription was examined. Doxycycline-induced expression of a potent shRNA targeting *Ctr9* showed strong CTR9 depletion (Figure 4.8 b). Chromatin immunoprecipitation followed by next-generation sequencing (ChIP-seq) revealed almost complete removal of CTR9 from chromatin (Figure 4.8 c). The CUT&RUN method was used to detect MYC binding to chromatin. MYC depletion decreased the signal to a level close to the IgG control, confirming the specificity of the

Results

MYC antibody (Figure 4.8 d). Consistent with previous observations in U2OS cells (Endres *et al.*, 2021), CTR9 depletion only moderately decreased MYC binding to chromatin. Gene set enrichment analysis showed that the decrease in MYC binding observed upon CTR9 depletion did not alter the expression of MYC target genes (Figure 4.8 e). This effect was also observed upon the depletion of CDC73, another subunit of the PAF1c. These data suggest that PAF1c only moderately affects MYC binding to chromatin, but is not required for MYC-dependent transcription.

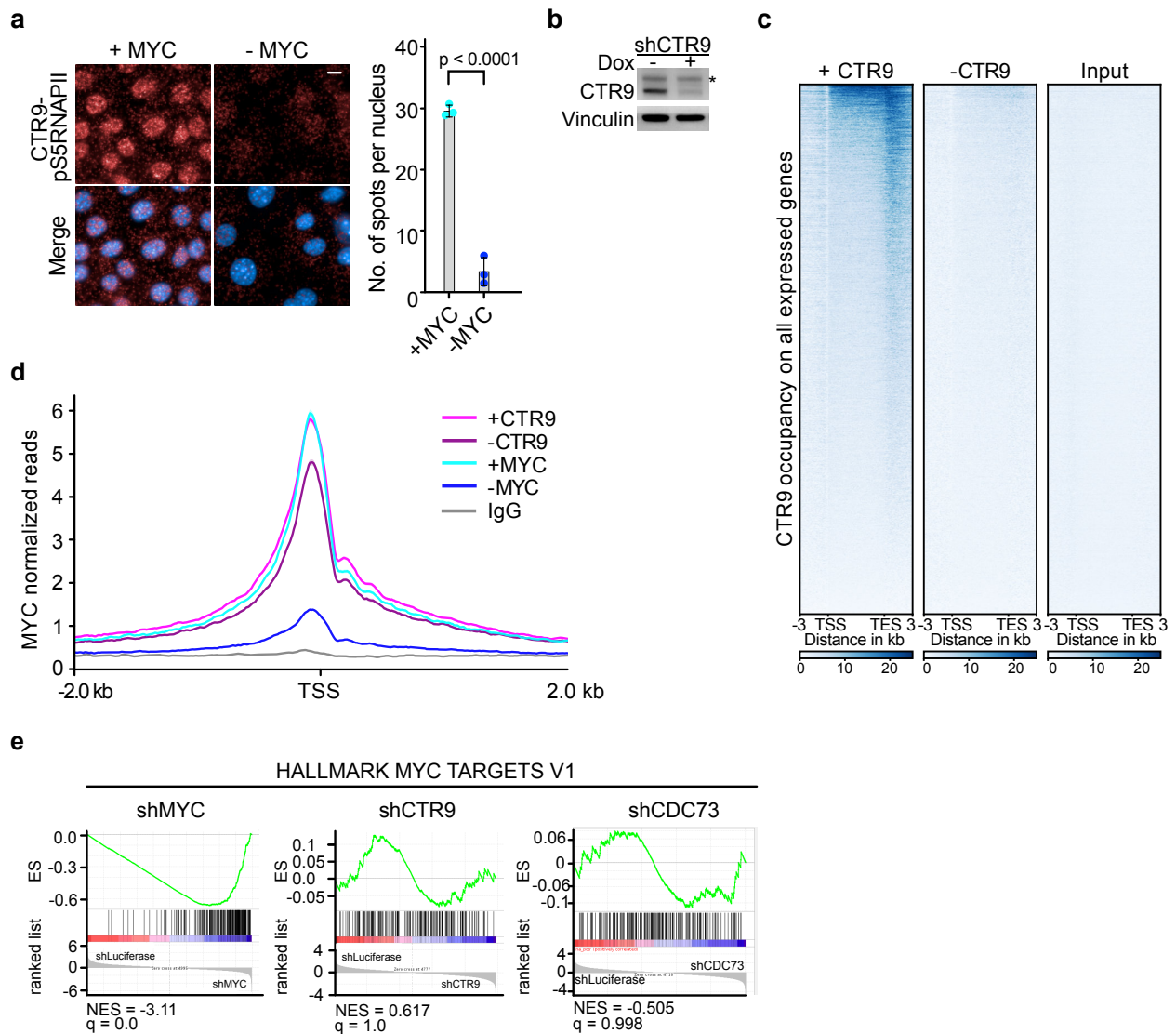


Figure 4. 8: Effect of PAF1c depletion on MYC-dependent transcription.

a. Left, representative images of PLAs between CTR9 and pS5RNAPII in cells harboring doxycycline-inducible shRNA targeting *Myc*. Scale bar: 10 μ m. Right, quantification of nuclear PLA foci (n=3; unpaired two-tailed *t*-test).

Results

b. Immunoblot of cells carrying doxycycline-inducible shRNA targeting CTR9. Where indicated, doxycycline was added for 48 hours. * indicates a non-specific band. Vinculin was used as loading control (n=4).

c. Heat map of CTR9 occupancy for all expressed (10920) genes analyzed by ChIP-Rx in cells carrying shCTR9. CTR9 depletion was achieved by adding doxycycline for 48h.

d. Average density plot of MYC occupancy localized around the transcription start site (TSS) of all expressed (10920) genes analyzed by CUT&RUN (n=1). "-CTR9" indicates samples in which CTR9 depletion was induced by doxycycline (1 µg/ml) for 48h in cells carrying doxycycline-inducible shRNA targeting *Ctr9*, and "+CTR9" indicates ethanol-treated cells. IgG was used as a negative control.

e. Gene set enrichment analysis plot of the gene set "HALLMARK MYC TARGETS V1" in cells expressing shRNA targeting luciferase versus either *Myc* (left), *Ctr9* (middle) or *Cdc73* (right) (n=3).

Parts of this figure may be published in a similar form in Gaballa et al., *Manuscript under consideration*.

4.4 PAF1c is required for the transcription of long DNA repair genes

4.4.1 PAF1c-dependent expression of DNA repair genes

The results in section 4.3.1 suggest that PAF1c function during transcription elongation is the critical function to prevent DNA damage during replication stress induced by ATR inhibition. To better understand this phenotype, an RNA sequencing experiment was performed. GO term analysis for down-regulated genes upon depletion of CTR9, CDC73 or MYC showed a significant enrichment of a group of genes involved in DNA repair and metabolism (Figure 4.9 a). Consistent with the results in (Figure 4.8 e), neither CTR9 nor CDC73 depletion affected the expression of MYC-dependent ribosome biogenesis genes. Notably, a group of DNA repair genes are relatively long, raising the possibility that PAF1c is specifically required to support the transcription of such long genes (Figure 4.9 b). Indeed, down-regulated genes upon CTR9 depletion in the DNA repair GO term were significantly longer than non- or up-regulated genes in the same GO term (Figure 4.9 c).

Results

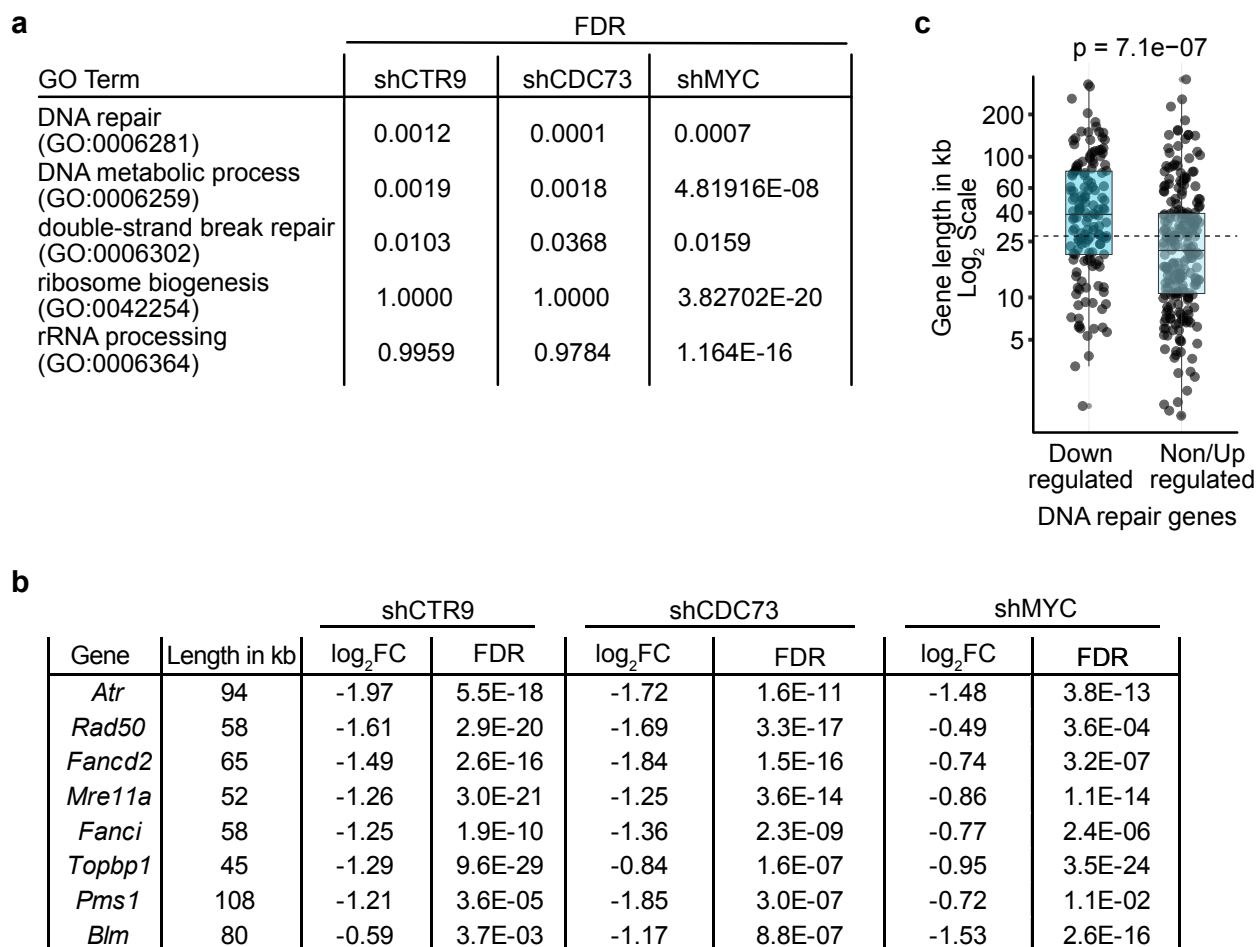


Figure 4. 9: PAF1c is required for the transcription of long DNA repair genes.

a. Table showing downregulated GO terms upon depletion of either CTR9, CDC73 or MYC. A log₂FC threshold of < -1 was set for the GO term search. False discovery rate (FDR) is calculated to adjust P values for multiple comparisons.

b. Table showing example genes involved in S-phase associated DNA repair that are downregulated upon depletion of either CTR9, CDC73 or MYC.

c. Box plot showing gene length in kilobases (kb) comparing genes expressed in the DNA repair GO term (GO-0006281, n=375 genes) stratified according to their differential expression upon CTR9 depletion to either downregulated (n = 147 genes) or non/upregulated (n = 228 genes). The dashed black line represents the median of all expressed genes in the DNA repair GO term. P value was calculated using the non-parametric Wilcoxon test.

Parts of this figure may be published in a similar form in Gaballa et al., *Manuscript under consideration*.

4.4.2 PAF1c promotes full-length transcription of long genes

To understand whether the effect of PAF1c depletion was limited to a specific downregulation of DNA repair genes or a more general downregulation of long genes,

Results

including many DNA repair genes, 4sU sequencing of nascent RNA was performed after CTR9 depletion. Consistent with its role in transcription elongation, metagene profiles for genes sorted into quartiles by ascending length showed a gene-length-dependent decrease in nascent transcription in the gene bodies of long genes, and that the strength of the decrease was dependent on gene length (Figure 4.10 a, b). It was also observed that depletion of CTR9 increased nascent transcription at promoter proximal regions. Consistent with this, RNA sequencing revealed a gene-length-dependent differential gene expression upon CTR9 depletion, with short genes being upregulated and long genes being downregulated (Figure 4.10 c). Consistently, total protein levels of several key DNA repair factors transcribed from long genes, showed a decrease upon CTR9 depletion (Figure 4.10 d). Next, ChIP sequencing was performed to map RNAPII on chromatin. CTR9 depletion caused a significant decrease (blue color) in RNAPII occupancy at the transcription start site (TSS) and a release (red color) into the gene body (Figure 4.10 e). This effect was observed for all genes regardless of their length and has been described in previous studies (Hou *et al.*, 2019; Wang *et al.*, 2022b; Yu *et al.*, 2015). Consistent with its role as an elongation factor, the RNAPII was released into gene bodies for only 20-30 kb and then its occupancy decreased. This observation shows that more RNAPII reaches the end of short genes, but not the end of long genes, and may explain the gene length-dependent differential expression effect observed upon CTR9 depletion.

Results

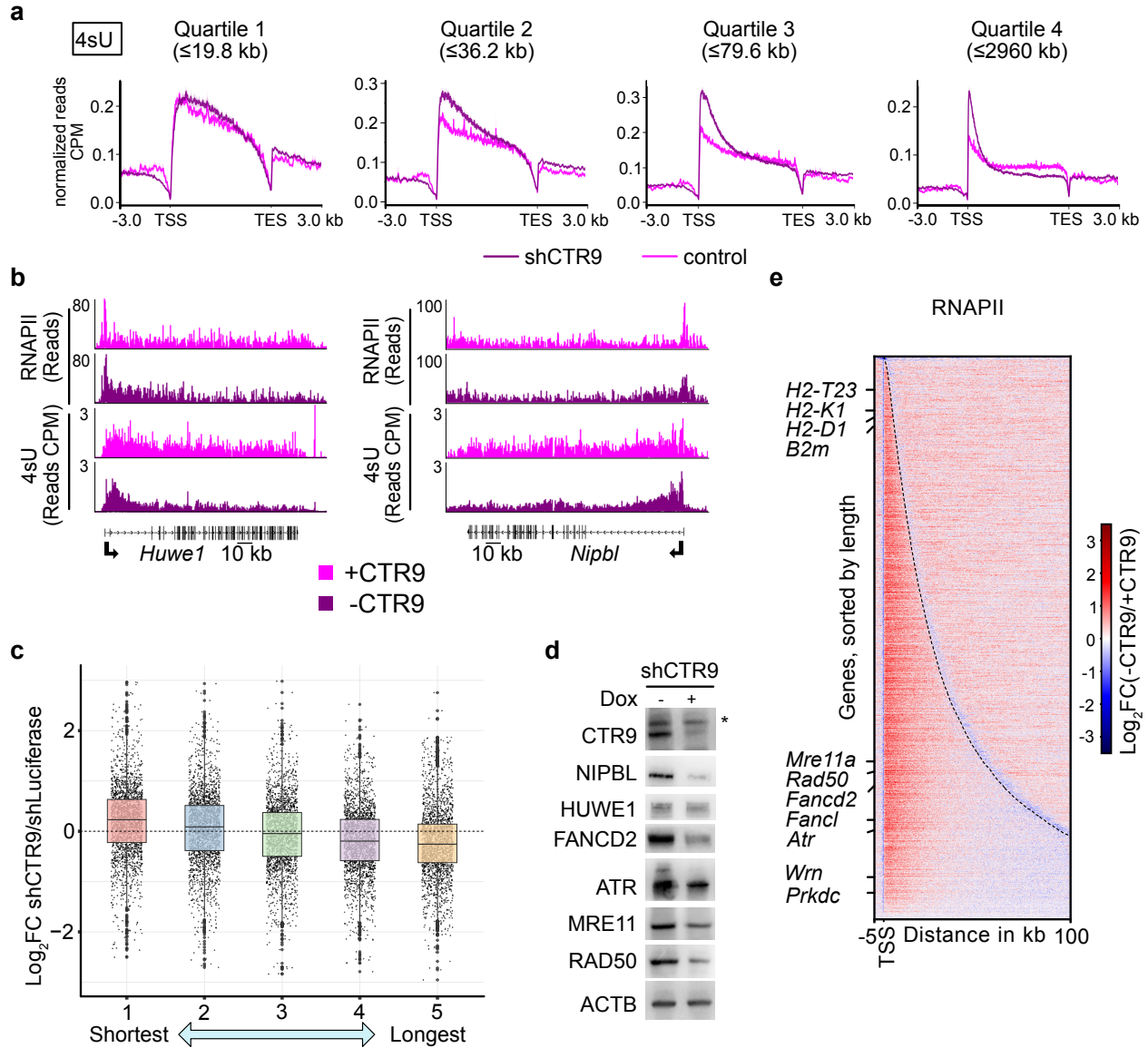


Figure 4. 10: PAF1c balances the transcriptional output of short and long genes.

a. Metagenetic plots mapping nascent transcription as indicated by 4sU incorporation. Metagenetic plots show read density averaged over the gene bodies of all expressed genes stratified by increasing length from quartile 1 (shortest) to quartile 4 (longest), where each quartile contains 2091 or 2092 genes. Only intronic 4sU-seq reads were considered (n=3).

b. Browser image showing read distribution of RNAPII ChIP-seencing (top) and 4sU-seencing showing nascent transcription (bottom) at two long DNA repair genes (GO-0006281) (n=2, for RNAPII ChIP-seencing. n=3, for 4sU-seencing experiment).

c. Box plot showing \log_2FC of mRNA sequencing analysis upon CTR9 depletion compared to control. Genes are shown as dots and bins of equal size are stratified based on their length from bin 1 (shortest) to bin 5 (longest). In this plot, \log_2FC was calculated based on reads mapped to the second half of the gene only.

d. Immunoblot documenting the levels of several key DNA repair proteins upon depletion of CTR9. * An asterisk indicates a non-specific band. CTR9 depletion was achieved by the addition of doxycycline for 48 hours (n=4).

Results

e. Heat map of the change in RNAPII occupancy for all expressed (n=10920) genes analyzed by spike-normalized ChIP-sequencing (ChIP-Rx) upon CTR9 depletion. Genes are ordered by length from shortest (top) to longest (bottom). The black dashed line represents the end of the gene. Some genes are annotated as belonging to either the DNA repair GO term (lower annotations) or the MHC class I GO term (upper annotations).

Parts of this figure may be published in a similar form in Gaballa et al., *Manuscript under consideration*.

4.5 PAF1c-dependent sequestration of SPT6 on long genes represses the expression of MHC class I genes

4.5.1 PAF1c represses the expression of MHC class I genes

Since the results in Figure 4.10 c show that many short genes were upregulated upon CTR9 depletion, GO term analysis was performed to search for the upregulated biological processes. Interestingly, genes involved in antigen processing and presentation (APAP) via MHC class I molecules as well as genes regulating T cell mediated cytotoxicity were upregulated upon either CTR9 or CDC73 depletion, similar to the MYC depletion shown previously (Figure 4.11 a, b) (Krenz *et al.*, 2021). This effect could possibly be explained by looking at the gene length of the APAP genes. To this end, a comparison between the gene length of DNA repair genes and APAP revealed a striking difference in their length, with APAP genes being significantly shorter (Figure 4.11 c).

Results

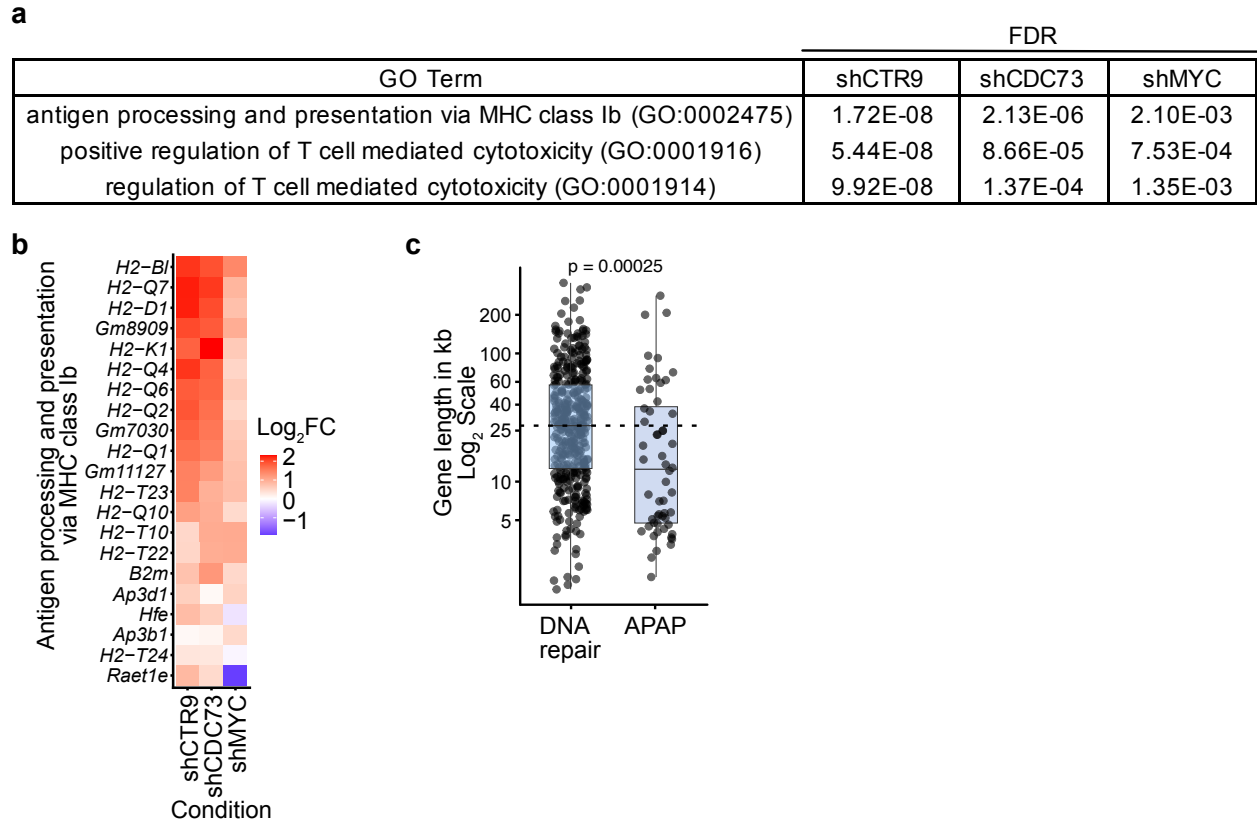


Figure 4. 11: PAF1c and MYC repress the transcription of MHC class I genes.

a. Table showing the FDR of upregulated GO terms upon depletion of CTR9, CDC73 or MYC.

b. Heat map showing \log_2FC of change in expression of genes involved in antigen processing and presentation via MHC class Ib (GO:0002475) upon depletion of either CTR9, CDC73 or MYC (n=3).

c. Box plot showing gene length in kilobases (kb), comparing expressed genes of the GO term DNA repair (GO-0006281, n=375 genes) with antigen processing and presentation genes (APAP, GO-0019882, n=56 genes). The dashed black line represents the median of all expressed genes in the DNA repair GO term. *P* value was calculated using the non-parametric Wilcoxon test.

Parts of this figure may be published in a similar form in Gaballa et al., *Manuscript under consideration*.

4.5.2 SPT6 binds MHC class I genes after CTR9 depletion

The data in Figure 4.10 suggest that PAF1c alters RNAPII occupancy, possibly by sequestering some elongation factors in the bodies of long genes, and upon PAF1c knockdown they are released and accumulate on short genes, aiding their transcription. To this end, I performed ChIP followed by quantitative real-time PCR to assess the relative binding of different proteins to four different APAP genes, either at promoter sites

Results

or in the gene bodies. Upon CTR9 depletion, total RNAPII decreased at promoters and increased in gene bodies (Figure 4.12 a), consistent with the ChIP sequencing result in Figure 4.10 e. CDK9-dependent RNAPII phosphorylation at serine 2 increased only moderately at both promoters and gene bodies, suggesting that the released RNAPII is in the elongating form (Figure 4.12 b). In addition, CTR9 depletion decreased the chromatin occupancy of RTF1 (Figure 4.12 c), another subunit of PAF1c that directly stimulates RNAPII elongation (Vos *et al.*, 2020; Vos *et al.*, 2018b). Furthermore, the chromatin association of the elongation factor SPT4, a subunit of DRB sensitivity inducing factor (DSIF), decreased at the promoter and increased at the gene bodies, following the behavior of total RNAPII (Figure 4.12 a, d). Strikingly, CTR9 depletion caused a strong increase in SPT6 chromatin occupancy at both promoters and gene bodies (Figure 4.12 e). SPT6 is a chromatin-remodeling histone chaperone that functions in transcription elongation and directly stimulates RNAPII processivity. (Kwak & Lis, 2013; Narain *et al.*, 2021; Zumer *et al.*, 2021). Taken together, these data suggest that SPT6 recruitment to chromatin may potentially support the transcription of MHC class I genes upon CTR9 depletion.

Results

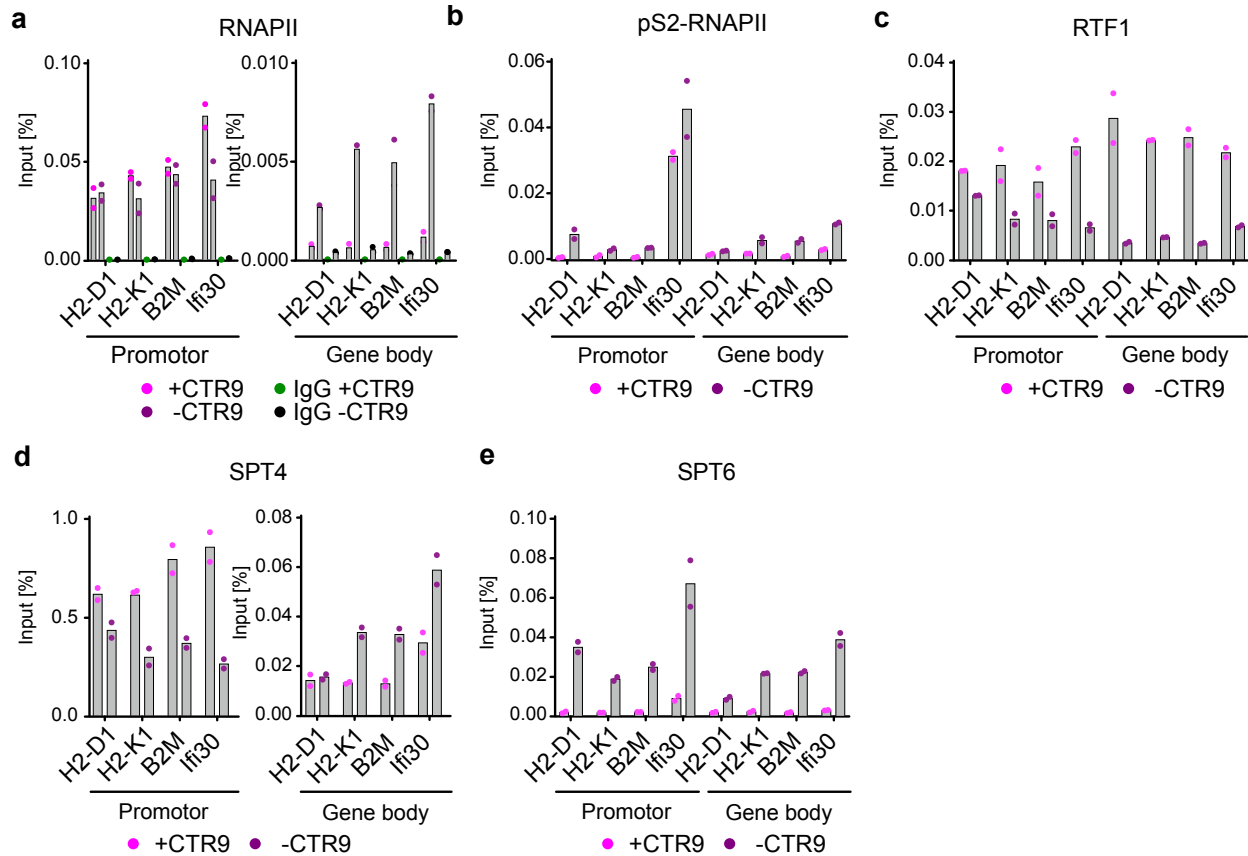


Figure 4. 12: Characterization of chromatin occupancy of different elongation factors upon CTR9 depletion

a. ChIP-qPCR showing RNAPII binding to the indicated genes either at the promoter or in the gene body. IgG was used as a negative control to show the background signal. Data show technical replicates (n=1).

b-e. Same as a, but showing pS2RNAPII, RTF1, SPT4 and SPT6 occupancy.

Parts of this figure may be published in a similar form in Gaballa et al., *Manuscript under consideration*.

4.5.3 SPT6 recruitment to MHC class I genes is required for their expression upon CTR9 depletion

Next, a ChIP-sequencing experiment for SPT6 and SPT5 was performed and compared to the total RNAPII described in section 4.4.2. SPT5, a subunit of the elongation factor DSIF, binds directly to MYC and is thereby recruited to promoters (Balupuri *et al.*, 2019). Browser track inspection of two major MHC class I genes showed an accumulation of SPT5 and RNAPII at the TSS, which are released to gene bodies upon CTR9 depletion (Figure 4.13 a). In contrast, SPT6 showed a very low enrichment close to the input background, which increased significantly upon CTR9 depletion. Upon CTR9 depletion,

Results

genome-wide analysis of SPT6 binding revealed a strong increase in SPT6 binding to chromatin at the TSS that persisted for 20-30kb downstream, reaching the ends of short but not long genes (Figure 4.13 b). Furthermore, the upregulation of two MHC class I genes tested upon CTR9 depletion was SPT6 dependent, suggesting that SPT6 recruitment to these genes is an important step for their upregulation (Figure 4.13 c).

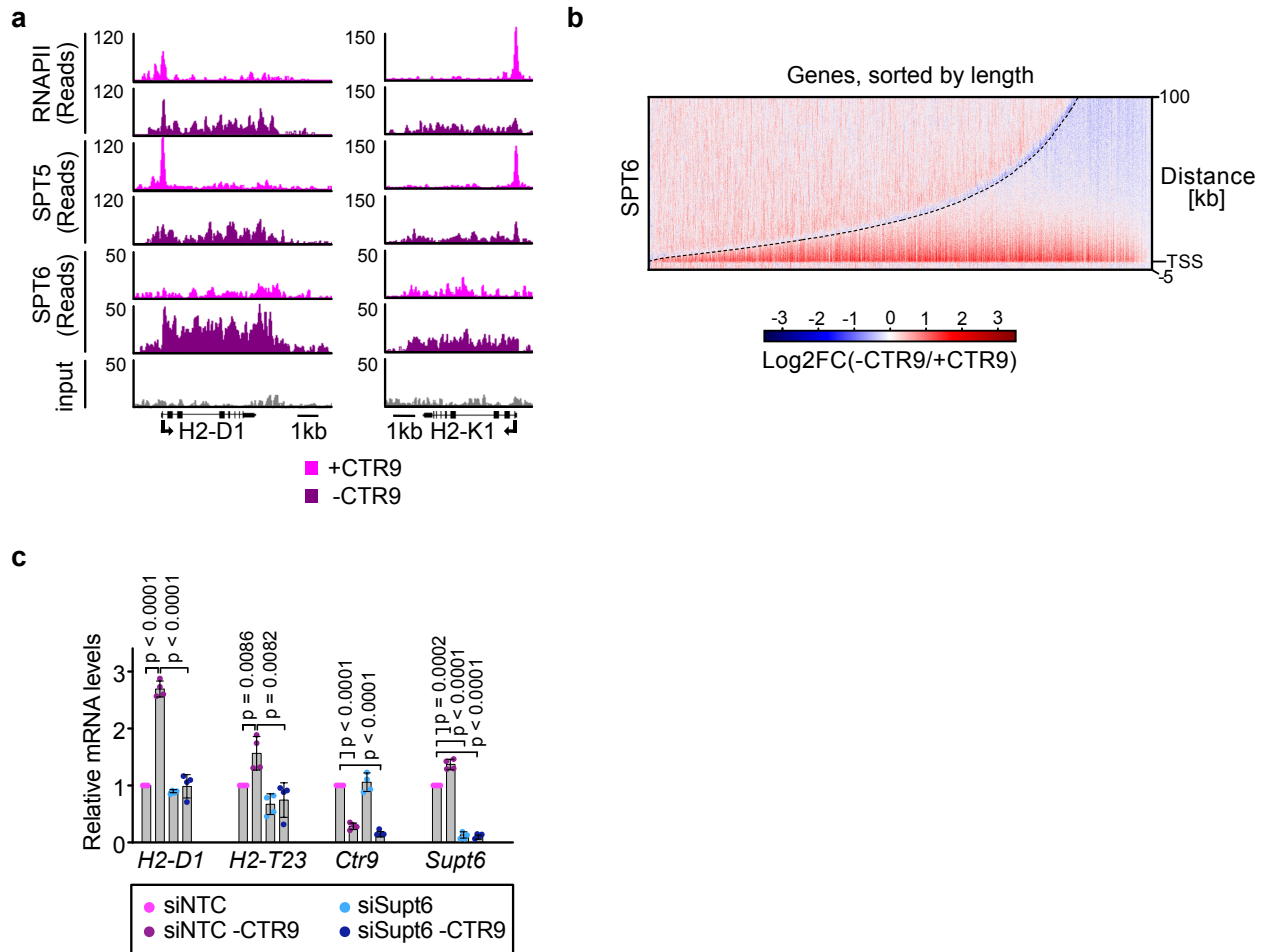


Figure 4. 13: SPT6 recruitment to MHC class I genes is required for their expression upon CTR9 depletion

a. Browser picture showing read distribution of RNAPII (top), SPT5 (middle) and SPT6 (bottom) at *H2-K1* and *H2-D1* genes from a ChIP-Rx experiment in cells expressing doxycycline-inducible shRNA targeting *Ctr9* (n=2).

b. Heat map of \log_2FC of SPT6 occupancy for all expressed (10,920) genes analyzed by ChIP-Rx comparing CTR9 depletion to control. Genes are ordered by length from shortest (left) to longest (right). The black dashed line represents the end of the gene (n=2).

c. RT-qPCR measurement of *H2-D1* and *H2-T23* MHC class I genes, *Ctr9* and *Supt6*. KPC cells expressing doxycycline-inducible shRNA targeting *Ctr9* were used. Both siRNA transfection and doxycycline addition were performed for 48h. Data are presented as mean \pm s.d. (n=4; unpaired two-sided *t*-test).

Parts of this figure may be published in a similar form in Gaballa et al., *Manuscript under consideration*.

4.5.4 SPT6 localization at the transcription end site is gene length dependent and correlates with gene expression upon CTR9 depletion

Since the results in section 4.5.3 showed that SPT6 may contribute to transcriptional output upon CTR9 depletion, a closer look was taken to further characterize its role. Under control conditions, chromatin binding of CTR9 (Figure 4.9 b) showed a strong correlation with SPT6 occupancy at the transcription end site (TES), suggesting that they both travel with RNAPII (Figure 4.14 a). Strikingly, SPT6 reaching the TES correlated with the change in mRNA expression upon CTR9 depletion (Figure 4.14 b). This provided evidence that the ability of SPT6 to reach the end of a gene is an important factor dictating its up-regulation. Consistent with the heat map shown in Figure 4.13 b, CTR9 depletion decreased SPT6 binding to TES in a gene length-dependent manner (Figure 4.14 c). Taken together, these data argue that PAF1c-dependent sequestration of SPT6 at the bodies of long genes represses the expression of MHC class I genes.

Results

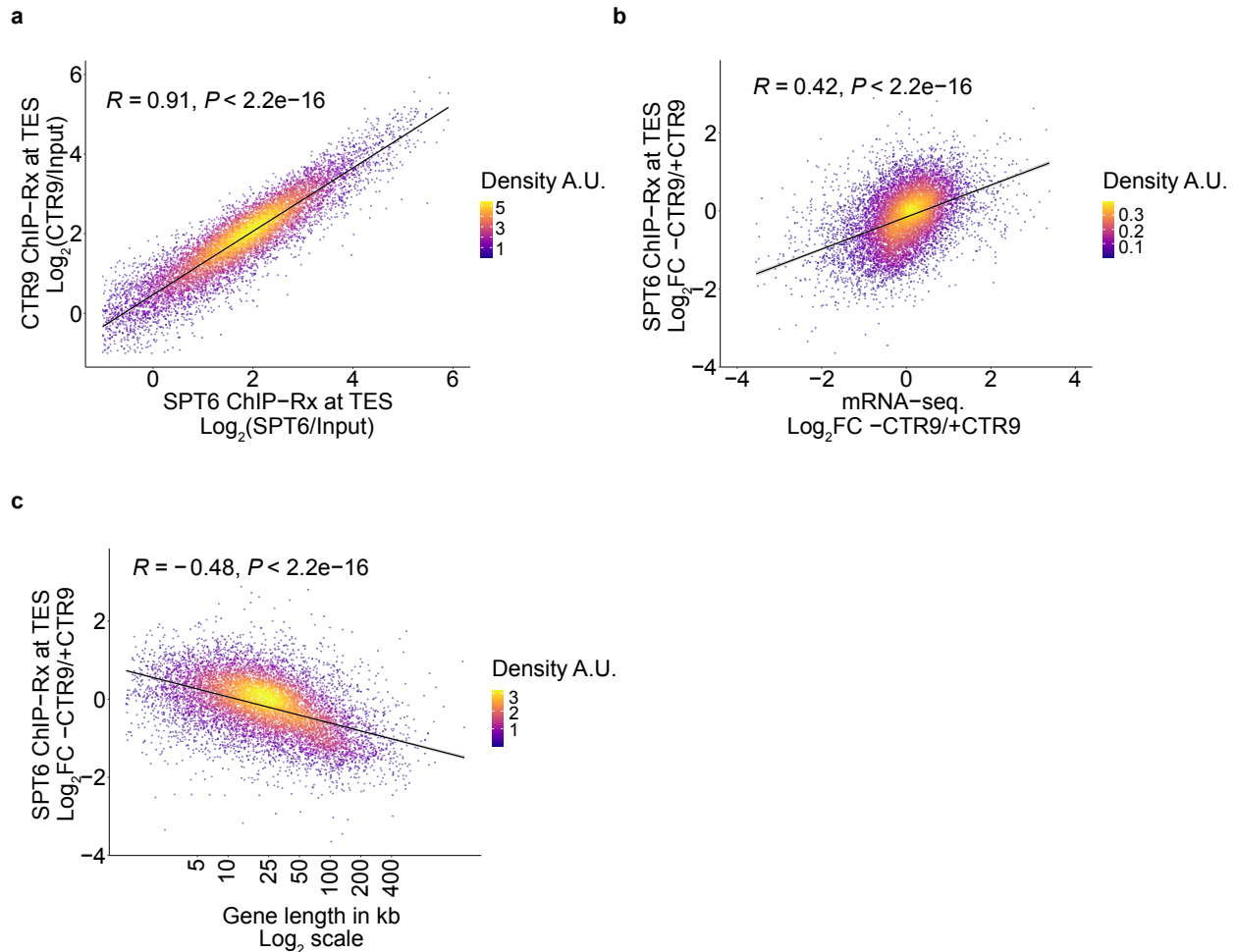


Figure 4. 14: Genome-wide analysis of SPT6 chromatin binding.

a. Scatter plot showing the correlation between SPT6 and CTR9 occupancy at the transcription end site (TES). The TES window was defined as -1 kb to +3 kb relative to the defined TES of each gene. Each dot represents one expressed gene, 10,920 genes in total. Log_2 reads mapped to TES for SPT6 (x-axis) or CTR9 (y-axis) were divided by input reads and plotted. R, Pearson correlation coefficient with calculated P value indicating its significance.

b. Scatter plot showing the correlation between change in mRNA expression (x-axis) and change in SPT6 chromatin binding (y-axis) upon CTR9 depletion. Each point represents one expressed gene, 10,920 genes in total. R, Pearson correlation coefficient with calculated P value indicating its significance.

c. Scatter plot showing the correlation between gene length (x-axis) and change in SPT6 chromatin binding (y-axis) upon CTR9 depletion. Each point represents one expressed gene, 10,920 genes in total. R, Pearson correlation coefficient with calculated P-value indicating its significance.

Parts of this figure may be published in a similar form in Gaballa et al., *Manuscript under consideration*.

4.6 PAF1c-dependent repression of MHC class I genes is conserved in multiple PDAC cell lines

Whether the PAF1c depletion phenotypes presented in this work are specific to the KPC cell line used or are conserved in other cancer cell lines with different mutational backgrounds remained open. To this end, two different murine PDAC cell lines, either p53-mutant or p16^{ink4a}(Cdkn2a)-deficient, were tested. Consistent with previous results, CTR9 depletion resulted in upregulation of two MHC class I genes and downregulation of two DNA repair genes tested (Figure 4.15 a). In addition, a human PDAC cell line (PA-TU-8988T) showed similar results (Figure 4.15 b). Consistently, CTR9 depletion sensitized these cell lines to increased DNA damage induction following ATR inhibition (Figure 4.15c). Taken together, the data presented suggest a more conserved function of PAF1c in promoting transcription of DNA repair (long) genes and repressing MHC class I (short) genes.

Results

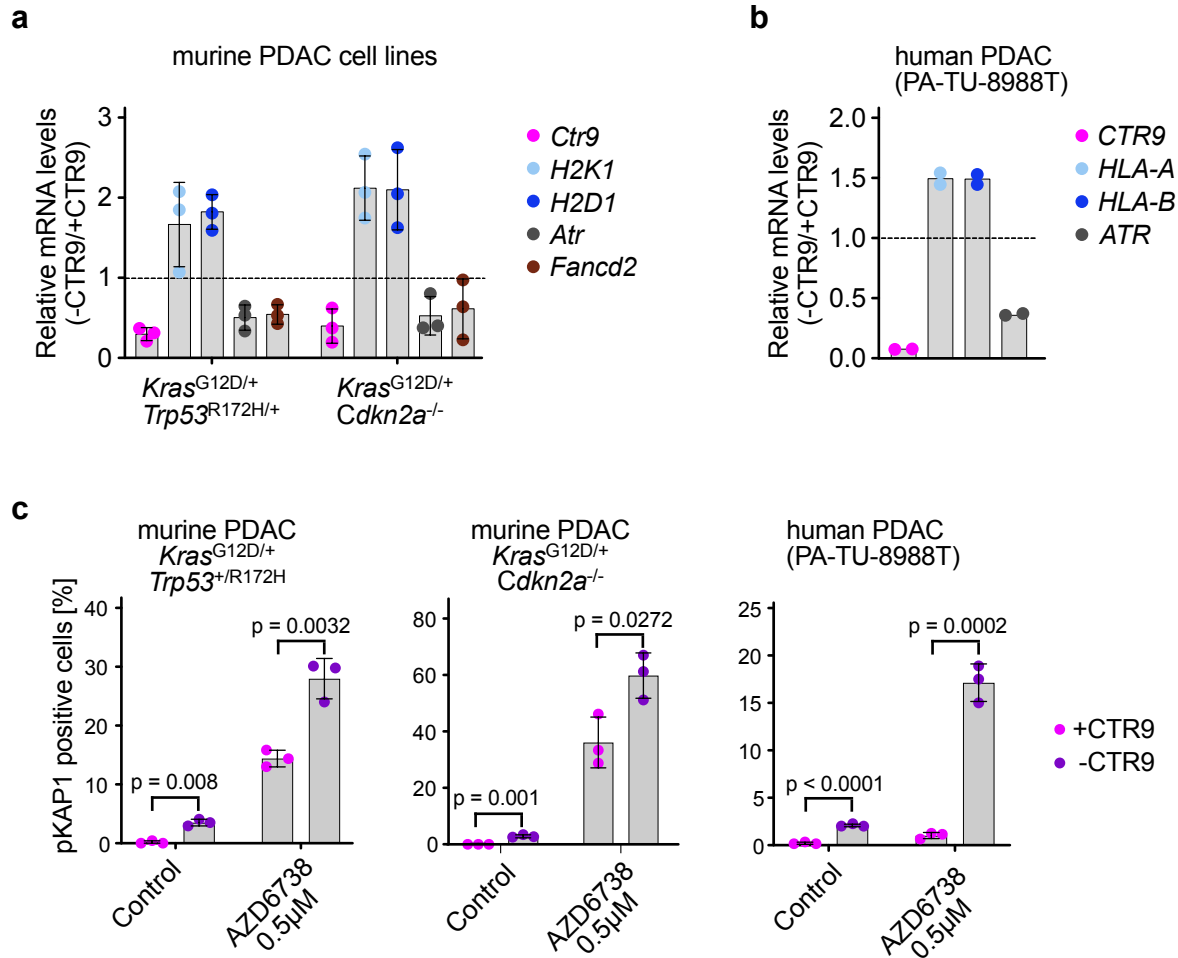


Figure 4. 15: Effects of CTR9 depletion in several PDAC cell lines

a. RT-qPCR measurement documenting the effects of CTR9 depletion in murine PDAC cells with the indicated genotypes. CTR9 depletion was induced by the addition of doxycycline for 48 h. Data are presented as mean \pm s.d. (n=3).

b. Same as a, but for PA-TU-8988T (bottom) human PDAC cell line. CTR9 depletion was induced by doxycycline addition for 48 h. Data are presented as the mean of two technical replicates.

c. Bar graphs documenting the percentage of pKAP1(S824)-positive cells in p53-mutant (left) or p16^{ink4a}-deficient (middle) murine PDAC cells as well as PA-TU-8988T (right) human PDAC cells. In the murine PDAC cell lines, CTR9 depletion was achieved by the addition of doxycycline for 48 h. PA-TU-8988T cells were transfected with siRNAs targeting CTR9. Treatment with AZD6738 0.5 μ M was for 72 h. Data are presented as mean \pm s.d. (n=3; unpaired two-sided *t*-test).

Parts of this figure may be published in a similar form in Gaballa et al., *Manuscript under consideration*.

4.7 CTR9 is required for PDAC maintenance *in vivo*

4.7.1 CTR9 depletion enables long-term survival of PDAC-bearing mice

MHC class I molecules bind peptides derived from mutated proteins, allowing CD8-positive T cells to identify and eliminate pathological cells such as cancer cells (Dhatchinamoorthy *et al*, 2021). Since PAF1c depletion resulted in the upregulation of MHC class I genes, its effect on tumor growth and maintenance *in vivo* was tested. To this end, two single-cell clones harboring doxycycline-inducible shRNA targeting *Ctr9* were selected and characterized for an efficient CTR9 depletion (Figure 4.16 a). An orthotopic transplantation model was used in which KPC cells were injected into the pancreas of syngeneic C57BL/6 mice and allowed to engraft for one week as previously described (Krenz *et al.*, 2021). Tumor status was then characterized by luciferase imaging, and doxycycline was added to the diet to induce CTR9 depletion (Figure 4.16 b). As a control, mice injected with KPC cells expressing non-targeting control shRNA were given food containing doxycycline, while another group of mice injected with KPC cells carrying shRNA targeting *Ctr9* were maintained in the absence of doxycycline. While control tumors expressing control shRNA and tumors harboring shRNA targeting *Ctr9* maintained in the absence of doxycycline continued to grow significantly, established tumors in which CTR9 was depleted often resulted in complete tumor regression (Figure 4.16 b, c). Both control groups of mice were sacrificed 44 days after transplantation. Strikingly, CTR9 depletion significantly prolonged survival, with five out of 17 mice surviving for more than 200 days, even though doxycycline administration in the diet was stopped after 91 days (Figure 4.16 d). This indicates that no tumor cells remained at the end of treatment and that this subset of mice was most likely cured.

Results

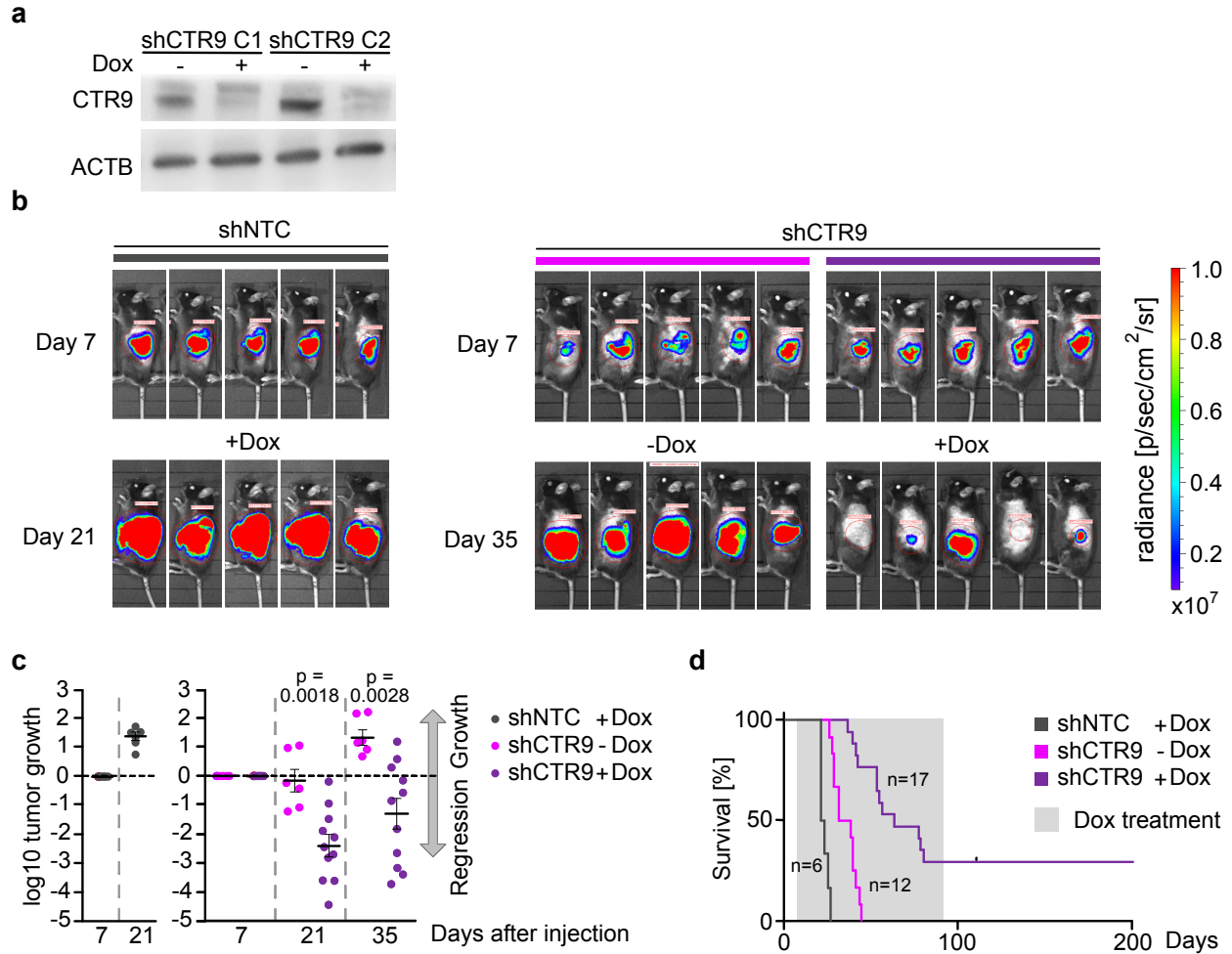


Figure 4. 16: Effect of CTR9 depletion *in vivo*

a. Immunoblot documenting CTR9 depletion in two different KPC clones carrying doxycycline-inducible shRNA targeting *Ctr9*.

b. Luciferase imaging of KPC cell-derived tumors expressing NTC (non-targeting control) shRNA or shRNA against *Ctr9* after orthotopic transplantation into C57BL/6J mice. Doxycycline treatment was initiated 7 days after transplantation. Luciferase activity is shown at day 7 after transplantation and after four weeks of doxycycline treatment.

c. Change in tumor volume of KPC tumors expressing doxycycline-inducible shNTC (left) or shCTR9 relative to the start of doxycycline treatment on day 7. The graph shows the \log_{10} of the ratio of luciferase activity at the indicated times relative to day 7. Results are presented as mean \pm S.E.M. *P* values were calculated using unpaired *t*-test.

d. Kaplan-Meier plot of mice transplanted with KPC cells expressing doxycycline-inducible shCTR9 or shNTC. Doxycycline was added to the diet as indicated for 12 weeks.

Parts of this figure may be published in a similar form in Gaballa et al., *Manuscript under consideration*.

All *in vivo* experiments were performed by Dr. Anneli Gebhardt-Wolf.

4.7.2 Survival benefit of CTR9 or MYC depletion is independent of ATR inhibition

The results in section 4.2.4 showed a strong enhancement of DNA damage induction upon PAF1c depletion and ATR inhibition. To test this *in vivo*, KPC cells were injected into mice as described in section 4.7.1. Doxycycline was administered in the diet and/or ATR inhibitor (AZD6738) was administered by gastric gavage for 3 days before tumors were harvested and analyzed by immunohistochemistry. Consistent with the *in vitro* data (Figure 4.6), CTR9 depletion enhanced the effect of ATR inhibition to induce DNA damage, as indicated by the phosphorylation of KAP1 (Figure 4.17 a, b). Furthermore, this effect was similar to that of γ -H2AX, another DNA damage marker tested (Figure 4.17 c, d).

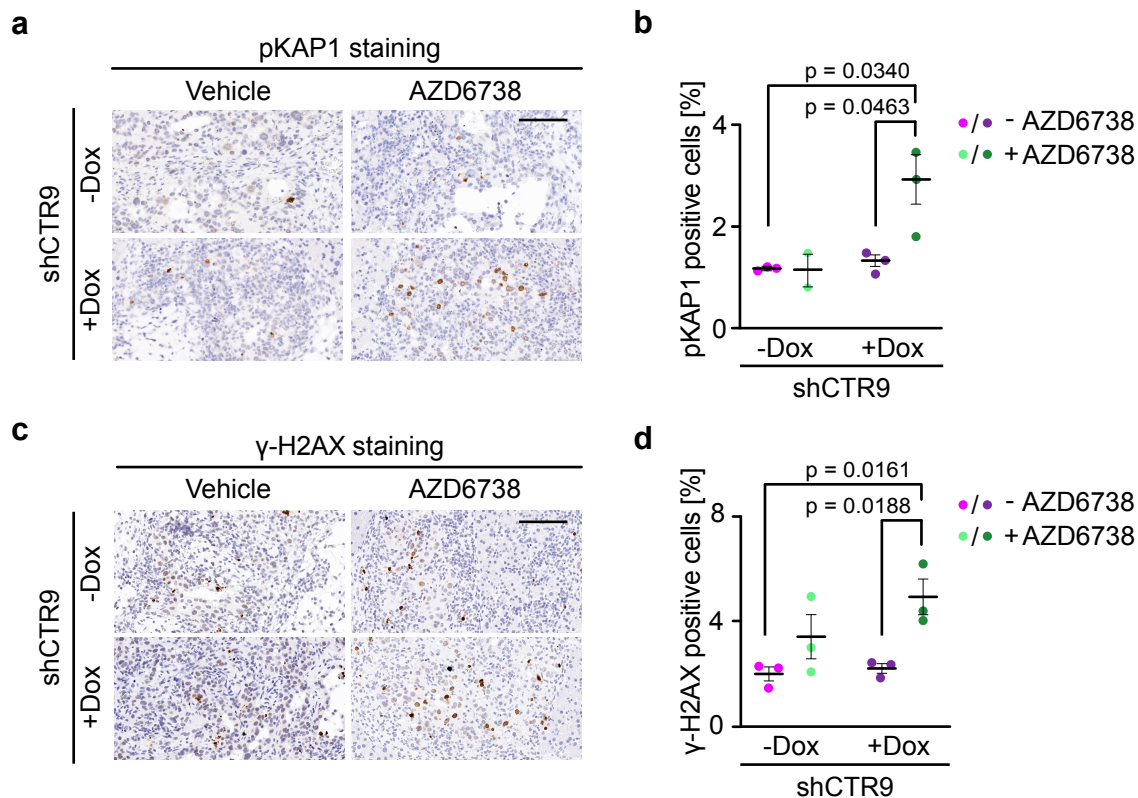


Figure 4. 17: Characterization of DNA damage induction *in vivo* upon CTR9 depletion and ATR inhibition.

a. Immunohistochemistry of pancreatic tumors expressing shRNA against *Ctr9*. Mice were treated with or without doxycycline and AZD6738 or vehicle for 3 days. Sections were stained with anti-pKAP1(S824) and anti- γ -H2AX antibodies. Scale bar: 100 μ m.

Results

b. Percentage of pKAP1 or γ -H2AX positive cells in tumor tissue. Positive cells were counted after 3 days of CTR9 depletion and AZD6738 treatment. Results are presented as mean \pm S.E.M. Each point represents an independent tumor and P values were calculated using unpaired t -test.

Parts of this figure may be published in a similar form in Gaballa et al., *Manuscript under consideration*.

All *in vivo* experiments were performed by Dr. Anneli Gebhardt-Wolf.

These results suggest that the combination of CTR9 depletion and ATR inhibition may confer a survival benefit by potentiating DNA damage induction. ATR inhibition resulted in a weak survival benefit in the control condition. Surprisingly, there was no clear survival benefit with the combination of ATR inhibition and CTR9 depletion, and the survival benefit was mainly driven by CTR9 depletion and not ATR inhibition (Figure 4.18). Furthermore, the survival benefit of ATR inhibition was similar in the control and after depletion of MYC (Figure 4.18). Taken together, the data in this section show that DNA damage induction does not correlate with survival benefit, suggesting that it is unlikely to be the potential reason for the tumor regression observed in section 4.7.1.

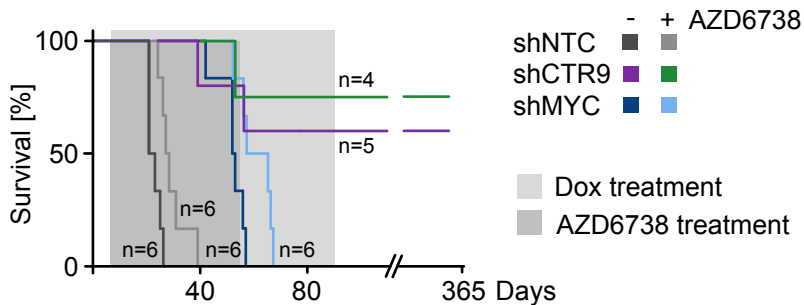


Figure 4. 18: Inhibition of ATR does not potentiate the survival benefit of CTR9 or MYC depletion compared to control.

Kaplan-Meier plot of mice transplanted with KPC cells expressing doxycycline-inducible shCTR9, shMYC or shNTC. Expression of shRNAs was induced with doxycycline from day 7 for 12 weeks in all mice. Mice were treated with AZD6738 or vehicle from day 7 for 7 weeks.

Parts of this figure may be published in a similar form in Gaballa et al., *Manuscript under consideration*.

All *in vivo* experiments were performed by Dr. Anneli Gebhardt-Wolf.

4.8 PAF1c mediates immune evasion in PDAC

4.8.1 CTR9 depletion reshapes the tumor microenvironment

The results presented in section 4.7 reveal two main observations: First, CTR9 depletion induces tumor regression and prolongs survival. Second, this effect is independent of the DNA damage induced by the combination with ATR inhibition. To understand how this effect is driven, CTR9 depletion was performed for 3 days prior to tumor harvest. Immunohistochemical analysis revealed an increased percentage of CD3-positive T cells with increased percentages of both cytotoxic CD8-positive and helper CD4-positive T cells (Figure 4.19 a). In addition, CTR9 depletion increased the influx of both B lymphocytes and macrophages (Figure 4.19 a). Strikingly, CTR9 knockdown reduced tumor cell density, with many remaining tumor cells in direct association with cytotoxic CD8-positive T cells (Figure 4.19 b).

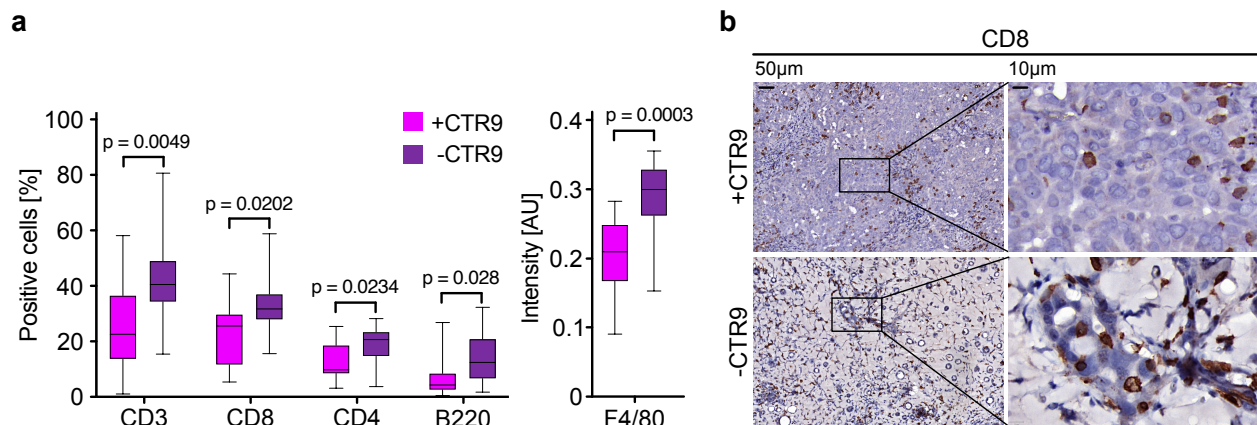


Figure 4. 19: Characterization of tumor immune cell infiltration upon CTR9 depletion.

a. Box plots showing the percentage of the indicated positive cells (left), or intensity of DAB (diaminobenzidine) staining (right) in tumor tissue. Pancreatic tumors expressing doxycycline-inducible shRNA against *Ctr9* were treated with/without doxycycline for three days. For each graph, $n \geq 4$ sections per tumor from three independent tumors were analyzed. P values were calculated by unpaired two-tailed t -test with Welch's correction.

b. Representative immunohistochemical images of tumor sections stained for CD8 (brown). Two different magnifications are shown. Note the juxtaposition of CD8-positive T cells with the rest of the tumor cells.

Parts of this figure may be published in a similar form in Gaballa et al., Manuscript under consideration.

The experiments shown in this figure were performed in collaboration with Dr. Anneli Gebhardt-Wolf and Dr. Mathias Rosenfeldt.

4.8.2 CTR9 mediates immune evasion in PDAC

To test the importance of tumor immune cell infiltration (Figure 4.19) for tumor regression and survival benefit after CTR9 depletion (Figure 4.16 b-d), NRG mice lacking both T and B lymphocytes and natural killer cells were used. KPC cells were transplanted as described above and allowed to engraft for one week. Strikingly, CTR9 was completely dispensable for tumor growth in NRG mice (Figure 4.20 a). Furthermore, there was no survival benefit upon CTR9 depletion (Figure 4.20 b). Taken together, these data suggest that the tumor regression observed after CTR9 depletion is entirely immune cell dependent and that immune cell infiltration into tumors is an important step for regression to occur.

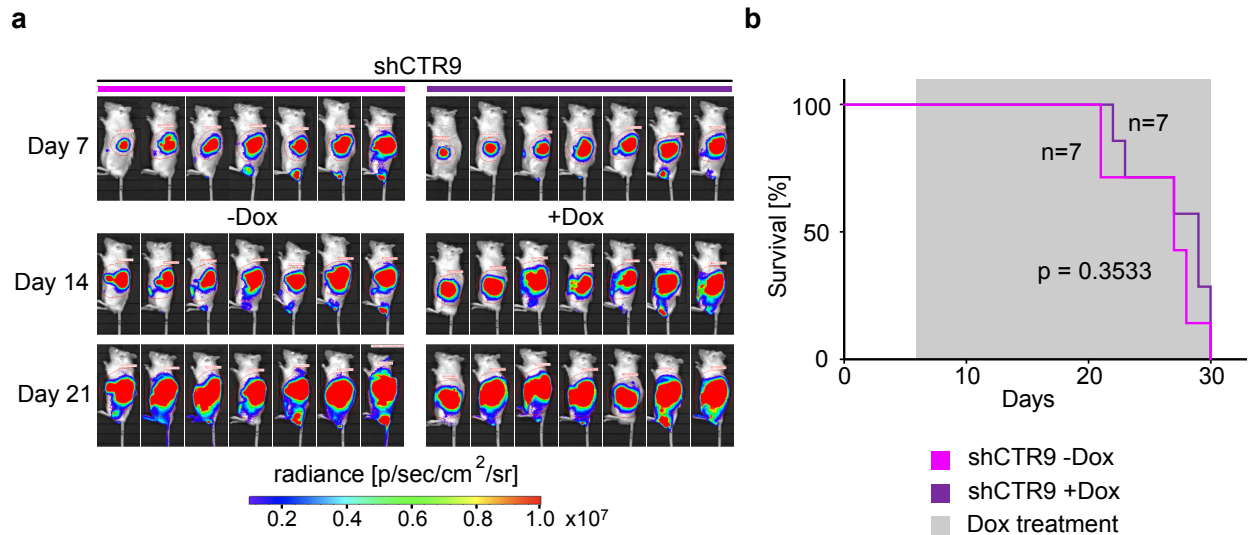


Figure 4. 20: Characterization of CTR9 depletion effect in tumors grown in immunodeficient mice.

a. Luciferase imaging of KPC cell-derived tumors carrying shRNA against *Ctr9* after orthotopic transplantation into NRG mice. Doxycycline treatment was initiated 7 days after transplantation. Luciferase activity of KPC cells was measured on day 7 after transplantation (start) and after 1 or 2 weeks of doxycycline treatment.

b. Kaplan-Meier plot of NRG mice transplanted with KPC cells expressing doxycycline-inducible shCTR9. Expression of shRNAs was induced by doxycycline starting on day 7. *P* values were calculated by Mantel-Cox test.

Parts of this figure may be published in a similar form in Gaballa et al., *Manuscript under consideration*.

All *in vivo* experiments were performed by Dr. Anneli Gebhardt-Wolf.

5 Discussion

5.1 MYC as a regulator of genomic stability

Previous studies from our laboratory suggested a link between MYC and S-phase progression and DNA repair. First, in PADC-driven KPC cells, MYC depletion prolonged the length of cell cycle phases, with S-phase being the most affected (Krenz *et al.*, 2021). Second, ectopic overexpression of MYC in U2OS cells was shown to suppress the accumulation of DNA double-strand breaks (Endres *et al.*, 2021). Third, MYC multimerization was shown to stabilize stalled replication forks, thereby limiting DNA double-strand break formation during S-phase (Solvie *et al.*, 2022).

Consistent with these studies, this work showed that MYC depletion decreased the rate of nucleotide incorporation during replication and induced DNA damage characterized by increased γ -H2AX signal. Consistent with the previous studies, DNA damage accumulated specifically during S-phase upon MYC depletion. Further experiments demonstrated that MYC prevents TRCs. This is consistent with previous studies demonstrating the role of MYCN in preventing TRCs mediated by Aurora-A (Roeschert *et al.*, 2021) or the RNA exosome (Papadopoulos *et al.*, 2022). During replication stress, cancer cells rely on ATR kinase to sense and resolve threats to genomic integrity (Saldivar *et al.*, 2017). Consistently, inhibition of the ATR kinase that is activated upon TRCs, synergized with MYC depletion to induce DNA damage.

5.2 Functions of MYC-dependent PAF1c recruitment to the RNAPII

In PDAC, MYC drives immune evasion and promotes S-phase progression (Krenz *et al.*, 2021). Whether these two functions are linked, and which downstream factors mediate these functions remained unclear. Recent MYC interactome studies have revealed the involvement of MYC in many complexes that drive a variety of functions, raising the question of which of these MYC interacting partners are required for MYC-dependent S-phase progression and immune evasion.

A siRNA-focused screen was performed to identify downstream factors of MYC that promote S-phase progression. PAF1c was the most prominent hit in this screen. This is consistent with a previous publication, showing that in yeast, PAF1c mediates RNAPII removal of chromatin during replication stress, thereby preventing TRCs (Poli *et al.*, 2016). Another study also showed that PAF1c is important for transcriptional recovery after DNA damage repair (van den Heuvel *et al.*, 2021). More recently, PAF1c was shown to be directly involved in the removal of RNAPII upon DNA damage (Chen *et al.*, 2022a). Although the results presented in this work do not show a direct involvement of PAF1c in the prevention of TRCs, they suggest the importance of this complex in limiting DNA damage during the S phase of the cell cycle. In addition to PAF1c, the siRNA screen revealed several hits involved in pre-mRNA splicing, namely AQR, EFTUD2, XAB2 and SFPQ. Indeed, this is consistent with previous siRNA screens showing that targeting the RNA splicing machinery induces DNA damage (Paulsen *et al.*, 2009).

The data presented here demonstrate that MYC is required for PAF1c recruitment to RNAPII, consistent with a previous study (Endres *et al.*, 2021). However, the mechanism proposed in this work differs from that described in Endres *et al.* where MYC-dependent histone ubiquitylation of H2B was found to be important for transcription elongation and DNA repair (Endres *et al.*, 2021). In this work, it was shown that reduction of H2B ubiquitylation by depletion of RNF20 didn't synergize with ATR inhibition to induce DNA damage. The different genetic background of the U2OS osteosarcoma cells used in Endres *et al.* and the PDAC-KPC cells used in this work, may explain this discrepancy.

Discussion

RNA sequencing experiments revealed that PAF1c is dispensable for MYC-dependent transcription. Furthermore, depletion of CTR9, a subunit of PAF1c, only moderately reduced MYC occupancy on chromatin, consistent with previous observations (Endres *et al.*, 2021).

A second siRNA screen for downstream factors of PAF1c revealed that HUWE1, CDK9, Cyclin K and its associated kinase CDK12 are critical for preventing DNA damage upon ATR inhibition. HUWE1 is an E3 ligase that mediates the transfer of PAF1c from MYC to RNAPII (Endres *et al.*, 2021), strongly supporting the conclusion of the first siRNA screen and arguing that PAF1c association with RNAPII is required to alleviate DNA damage during replication stress. CDK9 and CDK12 are important kinases for PAF1c-dependent transcription elongation (Yu *et al.*, 2015). These results suggest that the canonical function of PAF1c in transcription elongation is important for genomic stability.

Interference with proper transcription elongation can lead to genomic instability, either directly by reducing the processivity of RNAPII and preventing its proper eviction as the replication fork advances, or indirectly by down-regulating genes required for DNA repair (Noe Gonzalez *et al.*, 2021). Nascent transcription experiments showed that PAF1c is required for full-length transcription of particularly long genes. Subsequent RNA sequencing experiments confirmed a general downregulation of long genes and a parallel upregulation of short genes. In addition, RNAPII ChIP sequencing experiments showed a strong effect of PAF1c on transcription elongation. Depletion of PAF1c resulted in a decrease in RNAPII occupancy at TSS, accompanied by a release into gene bodies (Figure 4.10 e). Consistent with this, inhibition of RNAPII pause release by PAF1c was demonstrated by the Shilatifard laboratory in 2015 (Chen *et al.*, 2015). Interestingly, RNAPII release was restricted to the first 20-30 kb regardless of gene length, consistent with the well-documented function of PAF1c as an elongation factor (Chen *et al.*, 2022a; Hou *et al.*, 2019). This effect of PAF1c depletion allowed RNAPII to reach the end of short genes, but not the end of long genes. Subsequent analyses provided evidence that many of the long genes that were downregulated were involved in DNA repair. On the other hand, many of the short genes that were upregulated were genes involved in antigen processing and presentation.

5.3 PAF1c-dependent occupancy of transcription elongation factors

The change in RNAPII elongation upon PAF1c depletion could be due to a loss or gain of other transcription elongation factors. Examination of the chromatin occupancy of different factors revealed that DSIF, which is composed of SPT5 and SPT4, follows total RNAPII upon PAF1c depletion. Strikingly, depletion of PAF1c resulted in a strong enrichment of chromatin occupancy of SPT6 at TSS, which persisted for 20 to 30 kb and then decreased (Figure 4.13 b). This allows SPT6 to reach the end of short but not long genes, mimicking the results of nascent transcription. Indeed, bioinformatic analysis showed a significant correlation between increased SPT6 binding at the TES and upregulation of mRNA transcript upon CTR9 depletion. Furthermore, co-depletion of CTR9 and SPT6 rescued the upregulation of two of the MHC class I genes upon CTR9 depletion.

The observed increase in SPT6 chromatin occupancy may have several functions. First, SPT6 recruitment at the TSS may allow RNAPII progression through the +1 nucleosome, consistent with the previous finding of SPT6 function during RNAPII elongation (Zumer *et al.*, 2021). Second, an increase in SPT6 at the TSS and downstream of 20-30 kb may increase the processivity and velocity of RNAPII, thereby increasing the overall transcription of short but not long genes. Interestingly, loss of SPT6 has been shown to impair PAF1c recruitment to RNAPII (Aoi *et al.*, 2022). A model in which PAF1c stabilizes SPT6 on an elongating RNAPII is still open, and upon PAF1c loss, SPT6 accumulates at the TSS, travels briefly with the RNAPII, but quickly loses occupancy due to the absence of the "stabilizer". Consistent with this model, cryo-electron microscopy-based maps revealed a contact between SPT6 and CTR9 in the RNAPII elongation complex (Vos *et al.*, 2018a), which is consistent with published data showing an interaction between CTR9 and SPT6 (Adelman *et al.*, 2006; Dronamraju & Strahl, 2014; Kaplan *et al.*, 2005).

5.4 PAF1c: a novel therapeutic target in PDAC

Suppression of MHC class I gene expression is a well-documented function of oncogenic MYC or MYCN (Bernards *et al.*, 1986; Braun *et al.*, 1992; Versteeg *et al.*, 1988). The observed upregulation of the same set of genes upon PAF1c depletion motivated an *in vivo* experiment to evaluate the therapeutic benefit of depleting this complex. Indeed, depletion of CTR9 in established PDAC tumors caused strong regression, with many mice having no detectable tumor signal one week after depletion. This translated into a significant increase in survival, with five out of 17 mice considered to be long-term survivors.

Consistent with the *in vitro* data, the combination of CTR9 depletion and ATR inhibition was synergistic in inducing DNA damage *in vivo*. Strikingly, there was no therapeutic benefit from combining ATR inhibition with either CTR9 or MYC depletion, and the survival benefit was driven solely by CTR9 or MYC depletion (Figure 4.18). Upon DNA damage, the tumor suppressor p53 is activated and promotes either cell cycle arrest and DNA repair or apoptosis (Hafner *et al.*, 2019). Since KPC tumors express mutant p53, the induction of DNA damage upon CTR9 depletion and ATR inhibition may not be able to induce p53-dependent apoptosis.

The tumor regression observed upon CTR9 depletion was entirely immune cell dependent. In tumors transplanted into NRG mice, which lack both T and B lymphocytes as well as natural killer cells, CTR9 depletion had no effect on tumor size or survival. These results were similar to those obtained after MYC depletion (Krenz *et al.*, 2021). Consistent with the upregulation of MHC class I gene expression, there was a significant infiltration of CD3⁺ T cells, with increased infiltration of both CD8⁺ and CD4⁺ T cells. This was accompanied by increased infiltration of B220⁺ B cells and F4/80⁺ macrophages.

5.5 The hard-wired link between genomic stability and immune evasion in cancer

"Sustaining proliferative signaling" and "Enabling replicative immortality" are two hallmarks of cancer (Hanahan & Weinberg, 2011). Cancer cells seek sustained and uncontrolled proliferation, which increases the likelihood of accumulating mutations. In fact, "Genome instability and mutation" is considered to be a hallmark of cancer (Hanahan, 2022). Since mutations can frequently arise as a result of the genomic instability of cancer cells, limiting their recognition as non-self by the host immune system is essential for tumor growth. Thus, "Avoiding immune destruction" is also considered to be a hallmark of cancer (Hanahan, 2022).

5.5.1 Importance of gene-length-dependent transcription in cancer

While genomic instability contributes to tumorigenesis, impairment of DNA damage response pathways in cancer cells renders them susceptible to DNA damage and dependent on the residual expression of DNA repair genes (Hopkins *et al*, 2022). As a result, cancer cells may have a selective advantage by properly expressing DNA repair genes, many of which are long genes. Proper expression of these genes is also important for limiting the accumulation of mutations. These mutations pose a threat to cancer cells because peptides derived from mutated proteins are normally presented on MHC class I molecules on the cell surface. This presentation enables CD8+ T cells to recognize and eliminate these cells. Thus, limiting the recognition of cells harboring these mutations by downregulating the expression of MHC class I genes, many of which are short genes, is an important mechanism by which cancer cells evade immune recognition (Dersh *et al.*, 2021). This thesis provides evidence that these two processes are linked, and that the gene-length-dependent transcriptional equilibrium mediated by PAF1c provides an excellent program for cancer cell growth *in vivo*.

5.5.2 A new model linking genomic stability and immune evasion

A growing body of evidence links genomic instability to innate immune activation (Crossley *et al.*, 2023; Mackenzie *et al.*, 2017; Zhang *et al.*, 2020). This previous work has established a model in which the induction of DNA damage/R-loops leads to the accumulation of nucleic acid species in the cytoplasm that can be detected by specialized receptors as cyclic GMP-AMP synthase (cGAS). Once bound to cGAS, a pathway is activated that ultimately leads to the activation of innate immune signaling. However, the work in this thesis opens up a new model in which all events required for activation of immune signaling occur in the nucleus, eliminating any dependence on the cytosolic cGAS-STING pathway.

Binding of DNA to cGAS promotes its homodimerization and synthesis of the second messenger cyclic-GMP-AMP (cGAMP), which is recognized by the endoplasmic resident stimulator of interferon genes (STING) (Ishikawa *et al.*, 2009; Sun *et al.*, 2013). This leads to the recruitment of TANK-binding protein kinase 1 (TBK1) and IRF3, forming a trimeric structure. Subsequently, TBK1 phosphorylates IRF3, allowing its homodimerization and translocation to the nucleus, triggering innate immune signaling and the production of type I interferons (IFNs) (Ishikawa *et al.*, 2009; Sun *et al.*, 2013). The stresses encountered during cancer development may give an advantage to tumor cells that suppress the cGAS-STING pathway. For example, mutant p53 has been shown to disrupt the cGAS-STING-TBK1-IRF3 DNA-sensing pathway (Ghosh *et al.*, 2021; Ghosh *et al.*, 2023). Mechanistically, mutant p53, but not wild-type p53, binds to (TBK1), thereby preventing the formation of the trimeric complex between TBK1, STING and IRF3, which is required for IRF3 activation. Thus, restoring immunosurveillance independent of the cytosolic cGAS-STING pathway may be particularly important for patients with mutations in the *TP53* gene, which is considered to be the most frequently mutated gene in human cancers (Chen *et al.*, 2022b; Zhu *et al.*, 2020). Since the mechanism of PAF1c-mediated immune evasion presented in this work is independent of cytosolic sensing mechanisms, patients lacking an active cGAS-STING pathway, including patients with mutant p53, may particularly benefit from therapeutic targeting of the PAF1c.

Discussion

Unlike MYC, PAF1c is a well-structured protein, and its cryo-EM-based structure was determined at 3.1 Å resolution (Vos *et al.*, 2018a). Based on this, the Shilatifard lab set up a structure-based compound screen to identify novel small molecules that inhibit PAF1c function (Soliman *et al.*, 2023). Indeed, a first-in-class small molecule inhibitor of PAF1C (iPAF1C) was able to disrupt PAF1 binding to CTR9, decrease PAF1 chromatin occupancy and mimic genetic depletion of PAF1. This demonstrates the feasibility of targeting PAF1c with small molecules, thus offering implications for tumor therapy.

5.6 Conclusions

This work provides a rationale for targeting the immuno-evasive oncogenic function of MYC in PDAC. The MYC-dependent recruitment of PAF1c to RNAPII fulfills several functions required by aggressive tumors. First, PAF1c promotes the transcription of DNA repair genes and ensures their full-length transcription. DNA repair is required by rapidly proliferating cells to cope with replication and transcriptional stress. Second, PAF1c sequesters transcription elongation factors such as SPT6 away from short MHC class I genes. As a result, this set of genes is repressed, supporting tumor immune escape. Loss of PAF1c shifts the balance toward increased transcription of short genes. Thus, MHC class I genes are upregulated. At the same time, full-length transcription of long genes is disrupted. Since the transcriptional output upon PAF1c depletion is not optimal for tumor growth, established PDAC tumors regress upon CTR9 loss. CTR9 is not essential for tumor growth, as its loss in tumors transplanted into immunodeficient NRG mice does not affect tumor growth or survival. These findings suggest that targeting PAF1c makes tumors visible to the immune system while leaving normal, highly proliferating cells unaffected. A schematic summary of the work performed in this thesis is shown in Figure 5.1.

Discussion

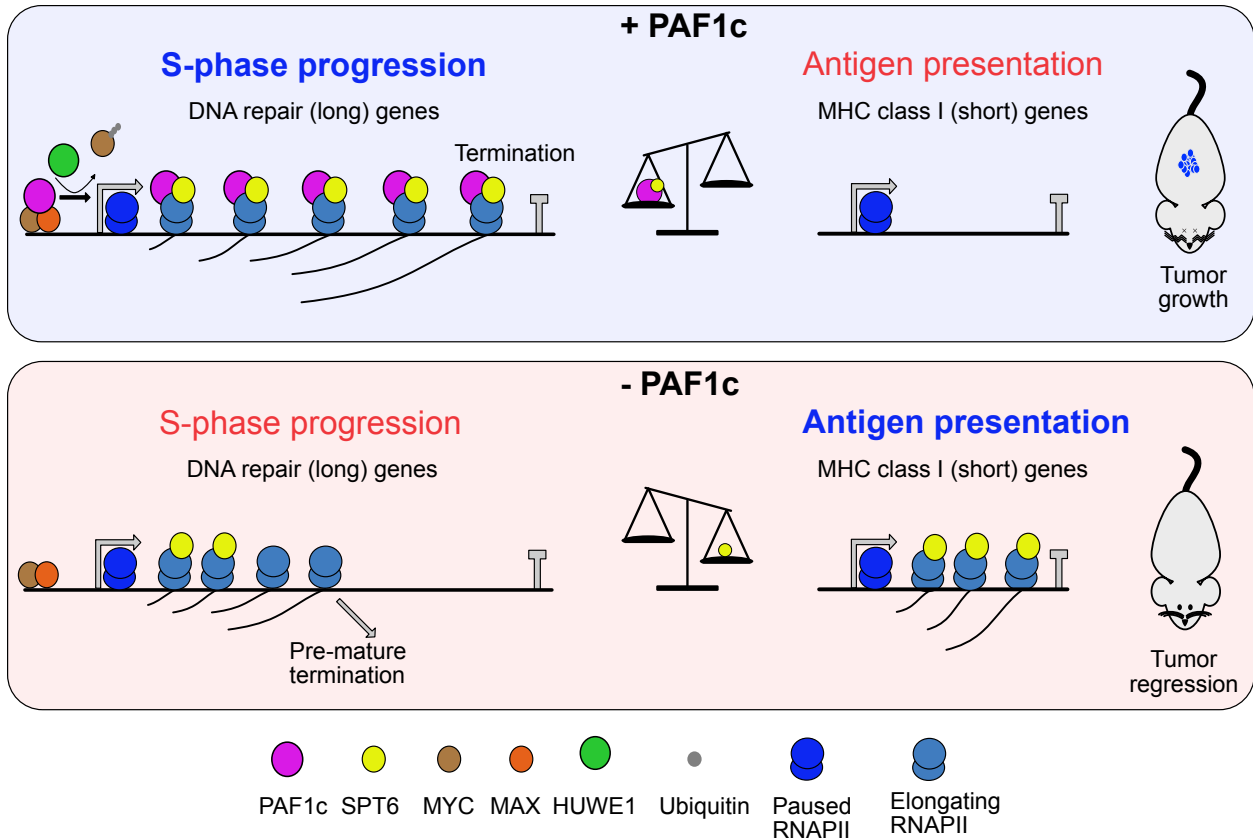


Figure 5. 1: Model summarizing the findings.

A model is presented that summarizes the findings presented in this dissertation. It is proposed that PAF1c acts downstream of MYC to promote full-length transcription of long DNA repair genes while limiting expression of short MHC class I genes. Disruption of PAF1c function redistributes transcription elongation factors, including SPT6. This restores the expression of short MHC class I genes and impairs the full-length transcription of long DNA repair genes. This change alters the tumor microenvironment, leading to immune cell-dependent tumor regression and long-term survival of PDAC-bearing mice.

Parts of this figure may be published in a similar form in Gaballa et al., *Manuscript under consideration*.

6 References

- Adams JM, Harris AW, Pinkert CA, Corcoran LM, Alexander WS, Cory S, Palmiter RD, Brinster RL (1985) The c-myc oncogene driven by immunoglobulin enhancers induces lymphoid malignancy in transgenic mice. *Nature* 318: 533-538
- Adelman K, Wei W, Ardehali MB, Werner J, Zhu B, Reinberg D, Lis JT (2006) Drosophila Paf1 modulates chromatin structure at actively transcribed genes. *Mol Cell Biol* 26: 250-260
- Aoi Y, Shah AP, Ganesan S, Soliman SHA, Cho BK, Goo YA, Kelleher NL, Shilatifard A (2022) SPT6 functions in transcriptional pause/release via PAF1C recruitment. *Mol Cell* 82: 3412-3423 e3415
- Baluapuri A, Hofstetter J, Dudvarski Stankovic N, Endres T, Bhandare P, Vos SM, Adhikari B, Schwarz JD, Narain A, Vogt M *et al* (2019) MYC Recruits SPT5 to RNA Polymerase II to Promote Processive Transcription Elongation. *Mol Cell* 74: 674-687 e611
- Baluapuri A, Wolf E, Eilers M (2020) Target gene-independent functions of MYC oncoproteins. *Nature Reviews Molecular Cell Biology* 21: 255-267
- Bankhead P, Loughrey MB, Fernandez JA, Dombrowski Y, McArt DG, Dunne PD, McQuaid S, Gray RT, Murray LJ, Coleman HG *et al* (2017) QuPath: Open source software for digital pathology image analysis. *Sci Rep* 7: 16878
- Bermejo R, Lai MS, Foiani M (2012) Preventing replication stress to maintain genome stability: resolving conflicts between replication and transcription. *Mol Cell* 45: 710-718
- Bernards R, Dessain SK, Weinberg RA (1986) N-myc amplification causes down-modulation of MHC class I antigen expression in neuroblastoma. *Cell* 47: 667-674
- Blackwood EM, Eisenman RN (1991) Max: a helix-loop-helix zipper protein that forms a sequence-specific DNA-binding complex with Myc. *Science* 251: 1211-1217
- Braun J, Felsher DW, Goodglick LA (1992) c-myc, MHCI, and NK resistance in immunodeficiency lymphomas. *Ann N Y Acad Sci* 651: 467-469

References

- Buchel G, Carstensen A, Mak KY, Roeschert I, Leen E, Sumara O, Hofstetter J, Herold S, Kalb J, Baluapuri A *et al* (2017) Association with Aurora-A Controls N-MYC-Dependent Promoter Escape and Pause Release of RNA Polymerase II during the Cell Cycle. *Cell Rep* 21: 3483-3497
- Burr ML, Sparbier CE, Chan KL, Chan YC, Kersbergen A, Lam EYN, Azidis-Yates E, Vassiliadis D, Bell CC, Gilan O *et al* (2019) An Evolutionarily Conserved Function of Polycomb Silences the MHC Class I Antigen Presentation Pathway and Enables Immune Evasion in Cancer. *Cancer Cell* 36: 385-401 e388
- Casey SC, Tong L, Li Y, Do R, Walz S, Fitzgerald KN, Gouw AM, Baylot V, Gutgemann I, Eilers M *et al* (2016) MYC regulates the antitumor immune response through CD47 and PD-L1. *Science* 352: 227-231
- Chen DS, Mellman I (2017) Elements of cancer immunity and the cancer-immune set point. *Nature* 541: 321-330
- Chen F, Liu B, Zhou H, Long J (2022a) The Paf1 complex is required for RNA polymerase II removal in response to DNA damage. *Proc Natl Acad Sci U S A* 119: e2207332119
- Chen FX, Woodfin AR, Gardini A, Rickels RA, Marshall SA, Smith ER, Shiekhattar R, Shilatifard A (2015) PAF1, a Molecular Regulator of Promoter-Proximal Pausing by RNA Polymerase II. *Cell* 162: 1003-1015
- Chen X, Zhang T, Su W, Dou Z, Zhao D, Jin X, Lei H, Wang J, Xie X, Cheng B *et al* (2022b) Mutant p53 in cancer: from molecular mechanism to therapeutic modulation. *Cell Death Dis* 13: 974
- Crossley MP, Song C, Bocek MJ, Choi JH, Kousorous J, Sathirachinda A, Lin C, Brickner JR, Bai G, Lans H *et al* (2023) R-loop-derived cytoplasmic RNA-DNA hybrids activate an immune response. *Nature* 613: 187-194
- Dammert MA, Bragelmann J, Olsen RR, Bohm S, Monhasery N, Whitney CP, Chalishazar MD, Tumbrink HL, Guthrie MR, Klein S *et al* (2019) MYC paralog-dependent apoptotic priming orchestrates a spectrum of vulnerabilities in small cell lung cancer. *Nat Commun* 10: 3485
- Dang CV (2012) MYC on the path to cancer. *Cell* 149: 22-35

References

- Dauch D, Rudalska R, Cossa G, Nault JC, Kang TW, Wuestefeld T, Hohmeyer A, Imbeaud S, Yevsa T, Hoenicke L *et al* (2016) A MYC-aurora kinase A protein complex represents an actionable drug target in p53-altered liver cancer. *Nat Med* 22: 744-753
- Dersh D, Holly J, Yewdell JW (2021) A few good peptides: MHC class I-based cancer immunosurveillance and immunoevasion. *Nat Rev Immunol* 21: 116-128
- Dhanasekaran R, Deutzmann A, Mahauad-Fernandez WD, Hansen AS, Gouw AM, Felsher DW (2022) The MYC oncogene - the grand orchestrator of cancer growth and immune evasion. *Nat Rev Clin Oncol* 19: 23-36
- Dhatchinamoorthy K, Colbert JD, Rock KL (2021) Cancer Immune Evasion Through Loss of MHC Class I Antigen Presentation. *Front Immunol* 12: 636568
- Dronamraju R, Strahl BD (2014) A feed forward circuit comprising Spt6, Ctk1 and PAF regulates Pol II CTD phosphorylation and transcription elongation. *Nucleic Acids Res* 42: 870-881
- Endres T, Solvie D, Heidelberger JB, Andrioletti V, Baluapuri A, Ade CP, Muhar M, Eilers U, Vos SM, Cramer P *et al* (2021) Ubiquitylation of MYC couples transcription elongation with double-strand break repair at active promoters. *Mol Cell* 81: 830-844 e813
- Falcon S, Gentleman R (2007) Using GOstats to test gene lists for GO term association. *Bioinformatics* 23: 257-258
- Farrell AS, Sears RC (2014) MYC degradation. *Cold Spring Harb Perspect Med* 4
- Francette AM, Tripplehorn SA, Arndt KM (2021) The Paf1 Complex: A Keystone of Nuclear Regulation Operating at the Interface of Transcription and Chromatin. *J Mol Biol* 433: 166979
- Freese NH, Norris DC, Loraine AE (2016) Integrated genome browser: visual analytics platform for genomics. *Bioinformatics* 32: 2089-2095
- Garrido F, Aptsiauri N (2019) Cancer immune escape: MHC expression in primary tumours versus metastases. *Immunology* 158: 255-266
- Ghosh M, Saha S, Bettke J, Nagar R, Parrales A, Iwakuma T, van der Velden AWM, Martinez LA (2021) Mutant p53 suppresses innate immune signaling to promote tumorigenesis. *Cancer Cell* 39: 494-508 e495
- Ghosh M, Saha S, Li J, Montrose DC, Martinez LA (2023) p53 engages the cGAS/STING cytosolic DNA sensing pathway for tumor suppression. *Mol Cell* 83: 266-280 e266

References

- Gomez-Gonzalez B, Aguilera A (2019) Transcription-mediated replication hindrance: a major driver of genome instability. *Genes Dev* 33: 1008-1026
- Hafner A, Bulyk ML, Jambhekar A, Lahav G (2019) The multiple mechanisms that regulate p53 activity and cell fate. *Nat Rev Mol Cell Biol* 20: 199-210
- Hamperl S, Bocek MJ, Saldivar JC, Swigut T, Cimprich KA (2017) Transcription-Replication Conflict Orientation Modulates R-Loop Levels and Activates Distinct DNA Damage Responses. *Cell* 170: 774-786 e719
- Hamperl S, Cimprich KA (2016) Conflict Resolution in the Genome: How Transcription and Replication Make It Work. *Cell* 167: 1455-1467
- Hanahan D (2022) Hallmarks of Cancer: New Dimensions. *Cancer Discov* 12: 31-46
- Hanahan D, Weinberg RA (2011) Hallmarks of cancer: the next generation. *Cell* 144: 646-674
- Hopkins JL, Lan L, Zou L (2022) DNA repair defects in cancer and therapeutic opportunities. *Genes Dev* 36: 278-293
- Hou L, Wang Y, Liu Y, Zhang N, Shamovsky I, Nudler E, Tian B, Dynlacht BD (2019) Paf1C regulates RNA polymerase II progression by modulating elongation rate. *Proc Natl Acad Sci U S A* 116: 14583-14592
- Ishikawa H, Ma Z, Barber GN (2009) STING regulates intracellular DNA-mediated, type I interferon-dependent innate immunity. *Nature* 461: 788-792
- Izban MG, Luse DS (1992) The RNA polymerase II ternary complex cleaves the nascent transcript in a 3'----5' direction in the presence of elongation factor SII. *Genes Dev* 6: 1342-1356
- Jaenicke LA, von Eyss B, Carstensen A, Wolf E, Xu W, Greifenberg AK, Geyer M, Eilers M, Popov N (2016) Ubiquitin-Dependent Turnover of MYC Antagonizes MYC/PAF1C Complex Accumulation to Drive Transcriptional Elongation. *Mol Cell* 61: 54-67
- Kalkat M, De Melo J, Hickman KA, Lourenco C, Redel C, Resetca D, Tamachi A, Tu WB, Penn LZ (2017) MYC Deregulation in Primary Human Cancers. *Genes (Basel)* 8
- Kalkat M, Resetca D, Lourenco C, Chan PK, Wei Y, Shiah YJ, Vitkin N, Tong Y, Sunnerhagen M, Done SJ *et al* (2018) MYC Protein Interactome Profiling Reveals Functionally Distinct Regions that Cooperate to Drive Tumorigenesis. *Mol Cell* 72: 836-848 e837

References

- Kaplan CD, Holland MJ, Winston F (2005) Interaction between transcription elongation factors and mRNA 3'-end formation at the *Saccharomyces cerevisiae* GAL10-GAL7 locus. *J Biol Chem* 280: 913-922
- Khan AN, Gregorie CJ, Tomasi TB (2008) Histone deacetylase inhibitors induce TAP, LMP, Tapasin genes and MHC class I antigen presentation by melanoma cells. *Cancer Immunol Immunother* 57: 647-654
- Kim J, Guermah M, McGinty RK, Lee JS, Tang Z, Milne TA, Shilatifard A, Muir TW, Roeder RG (2009) RAD6-Mediated transcription-coupled H2B ubiquitylation directly stimulates H3K4 methylation in human cells. *Cell* 137: 459-471
- Kim J, Roeder RG (2009) Direct Bre1-Paf1 complex interactions and RING finger-independent Bre1-Rad6 interactions mediate histone H2B ubiquitylation in yeast. *J Biol Chem* 284: 20582-20592
- Kohl NE, Kanda N, Schreck RR, Bruns G, Latt SA, Gilbert F, Alt FW (1983) Transposition and amplification of oncogene-related sequences in human neuroblastomas. *Cell* 35: 359-367
- Kortlever RM, Sodir NM, Wilson CH, Burkhart DL, Pellegrinet L, Brown Swigart L, Littlewood TD, Evan GI (2017) Myc Cooperates with Ras by Programming Inflammation and Immune Suppression. *Cell* 171: 1301-1315 e1314
- Krenz B, Gebhardt-Wolf A, Ade CP, Gaballa A, Roehrig F, Vendelova E, Baluapuri A, Eilers U, Gallant P, D'Artista L *et al* (2021) MYC- and MIZ1-Dependent Vesicular Transport of Double-Strand RNA Controls Immune Evasion in Pancreatic Ductal Adenocarcinoma. *Cancer Res* 81: 4242-4256
- Kwak H, Lis JT (2013) Control of transcriptional elongation. *Annu Rev Genet* 47: 483-508
- Kwok M, Davies N, Agathangelou A, Smith E, Petermann E, Yates E, Brown J, Lau A, Stankovic T (2015) Synthetic lethality in chronic lymphocytic leukaemia with DNA damage response defects by targeting the ATR pathway. *Lancet* 385 Suppl 1: S58
- Lalonde M, Trauner M, Werner M, Hamperl S (2021) Consequences and Resolution of Transcription-Replication Conflicts. *Life (Basel)* 11
- Langmead B, Salzberg SL (2012) Fast gapped-read alignment with Bowtie 2. *Nat Methods* 9: 357-359

References

- Li H, Handsaker B, Wysoker A, Fennell T, Ruan J, Homer N, Marth G, Abecasis G, Durbin R, Genome Project Data Processing S (2009) The Sequence Alignment/Map format and SAMtools. *Bioinformatics* 25: 2078-2079
- Liao Y, Smyth GK, Shi W (2019) The R package Rsubread is easier, faster, cheaper and better for alignment and quantification of RNA sequencing reads. *Nucleic Acids Res* 47: e47
- Liu X, Guo Z, Han J, Peng B, Zhang B, Li H, Hu X, David CJ, Chen M (2022) The PAF1 complex promotes 3' processing of pervasive transcripts. *Cell Rep* 38: 110519
- Mackenzie KJ, Carroll P, Martin CA, Murina O, Fluteau A, Simpson DJ, Olova N, Sutcliffe H, Rainger JK, Leitch A *et al* (2017) cGAS surveillance of micronuclei links genome instability to innate immunity. *Nature* 548: 461-465
- Makela TP, Saksela K, Evan G, Alitalo K (1991) A fusion protein formed by L-myc and a novel gene in SCLC. *EMBO J* 10: 1331-1335
- Meers MP, Bryson TD, Henikoff JG, Henikoff S (2019) Improved CUT&RUN chromatin profiling tools. *Elife* 8
- Mirkin EV, Mirkin SM (2005) Mechanisms of transcription-replication collisions in bacteria. *Mol Cell Biol* 25: 888-895
- Moyal L, Lerenthal Y, Gana-Weisz M, Mass G, So S, Wang SY, Eppink B, Chung YM, Shalev G, Shema E *et al* (2011) Requirement of ATM-dependent monoubiquitylation of histone H2B for timely repair of DNA double-strand breaks. *Mol Cell* 41: 529-542
- Muthalagu N, Monteverde T, Raffo-Iraolagoitia X, Wiesheu R, Whyte D, Hedley A, Laing S, Kruspig B, Upstill-Goddard R, Shaw R *et al* (2020) Repression of the Type I Interferon Pathway Underlies MYC- and KRAS-Dependent Evasion of NK and B Cells in Pancreatic Ductal Adenocarcinoma. *Cancer Discov* 10: 872-887
- Narain A, Bhandare P, Adhikari B, Backes S, Eilers M, Dolken L, Schlosser A, Erhard F, Baluapuri A, Wolf E (2021) Targeted protein degradation reveals a direct role of SPT6 in RNAPII elongation and termination. *Mol Cell* 81: 3110-3127 e3114
- Nau MM, Brooks BJ, Battey J, Sausville E, Gazdar AF, Kirsch IR, McBride OW, Bertness V, Hollis GF, Minna JD (1985) L-myc, a new myc-related gene amplified and expressed in human small cell lung cancer. *Nature* 318: 69-73

References

- Noe Gonzalez M, Blears D, Svejstrup JQ (2021) Causes and consequences of RNA polymerase II stalling during transcript elongation. *Nat Rev Mol Cell Biol* 22: 3-21
- Papadopoulos D, Solvie D, Baluapuri A, Endres T, Ha SA, Herold S, Kalb J, Giansanti C, Schulein-Volk C, Ade CP *et al* (2022) MYCN recruits the nuclear exosome complex to RNA polymerase II to prevent transcription-replication conflicts. *Mol Cell* 82: 159-176 e112
- Paulsen RD, Soni DV, Wollman R, Hahn AT, Yee MC, Guan A, Hesley JA, Miller SC, Cromwell EF, Solow-Cordero DE *et al* (2009) A genome-wide siRNA screen reveals diverse cellular processes and pathways that mediate genome stability. *Mol Cell* 35: 228-239
- Pelossof R, Fairchild L, Huang CH, Widmer C, Sreedharan VT, Sinha N, Lai DY, Guan Y, Premririt PK, Tschaharganeh DF *et al* (2017) Prediction of potent shRNAs with a sequential classification algorithm. *Nat Biotechnol* 35: 350-353
- Pishesha N, Harmand TJ, Ploegh HL (2022) A guide to antigen processing and presentation. *Nat Rev Immunol* 22: 751-764
- Poli J, Gerhold CB, Tosi A, Hustedt N, Seeber A, Sack R, Herzog F, Pasero P, Shimada K, Hopfner KP *et al* (2016) Mec1, INO80, and the PAF1 complex cooperate to limit transcription replication conflicts through RNAPII removal during replication stress. *Genes Dev* 30: 337-354
- Prado F, Aguilera A (2005) Impairment of replication fork progression mediates RNA polII transcription-associated recombination. *EMBO J* 24: 1267-1276
- Ramirez F, Dundar F, Diehl S, Gruning BA, Manke T (2014) deepTools: a flexible platform for exploring deep-sequencing data. *Nucleic Acids Res* 42: W187-191
- Richards MW, Burgess SG, Poon E, Carstensen A, Eilers M, Chesler L, Bayliss R (2016) Structural basis of N-Myc binding by Aurora-A and its destabilization by kinase inhibitors. *Proc Natl Acad Sci U S A* 113: 13726-13731
- Rickman DS, Schulte JH, Eilers M (2018) The Expanding World of N-MYC-Driven Tumors. *Cancer Discov* 8: 150-163
- Rocha EPC (2004) The replication-related organization of bacterial genomes. *Microbiology (Reading)* 150: 1609-1627

References

- Roeschert I, Poon E, Henssen AG, Garcia HD, Gatti M, Giansanti C, Jamin Y, Ade CP, Gallant P, Schulein-Volk C *et al* (2021) Combined inhibition of Aurora-A and ATR kinase results in regression of MYCN-amplified neuroblastoma. *Nat Cancer* 2: 312-326
- Saldivar JC, Cortez D, Cimprich KA (2017) The essential kinase ATR: ensuring faithful duplication of a challenging genome. *Nat Rev Mol Cell Biol* 18: 622-636
- Sansom OJ, Meniel VS, Muncan V, Pheffe TJ, Wilkins JA, Reed KR, Vass JK, Athineos D, Clevers H, Clarke AR (2007) Myc deletion rescues Apc deficiency in the small intestine. *Nature* 446: 676-679
- Schaub FX, Dhankani V, Berger AC, Trivedi M, Richardson AB, Shaw R, Zhao W, Zhang X, Ventura A, Liu Y *et al* (2018) Pan-cancer Alterations of the MYC Oncogene and Its Proximal Network across the Cancer Genome Atlas. *Cell Syst* 6: 282-300 e282
- Schwab M, Alitalo K, Klempnauer KH, Varmus HE, Bishop JM, Gilbert F, Brodeur G, Goldstein M, Trent J (1983) Amplified DNA with limited homology to myc cellular oncogene is shared by human neuroblastoma cell lines and a neuroblastoma tumour. *Nature* 305: 245-248
- Sharma P, Allison JP (2015) Immune checkpoint targeting in cancer therapy: toward combination strategies with curative potential. *Cell* 161: 205-214
- Smith T, Heger A, Sudbery I (2017) UMI-tools: modeling sequencing errors in Unique Molecular Identifiers to improve quantification accuracy. *Genome Res* 27: 491-499
- Sodir NM, Kortlever RM, Barthet VJA, Campos T, Pellegrinet L, Kupczak S, Anastasiou P, Swigart LB, Soucek L, Arends MJ *et al* (2020) MYC Instructs and Maintains Pancreatic Adenocarcinoma Phenotype. *Cancer Discov* 10: 588-607
- Soliman SHA, Cisneros WJ, Iwanaszko M, Aoi Y, Ganesan S, Walter M, Zeidner JM, Mishra RK, Kim EY, Wolinsky SM *et al* (2023) Enhancing HIV-1 latency reversal through regulating the elongating RNA Pol II pause-release by a small-molecule disruptor of PAF1C. *Sci Adv* 9: eadf2468
- Sollier J, Stork CT, Garcia-Rubio ML, Paulsen RD, Aguilera A, Cimprich KA (2014) Transcription-coupled nucleotide excision repair factors promote R-loop-induced genome instability. *Mol Cell* 56: 777-785

References

- Solvie D, Baluapuri A, Uhl L, Fleischhauer D, Endres T, Papadopoulos D, Aziba A, Gaballa A, Mikicic I, Isaakova E *et al* (2022) MYC multimers shield stalled replication forks from RNA polymerase. *Nature* 612: 148-155
- Srivatsan A, Tehranchi A, MacAlpine DM, Wang JD (2010) Co-orientation of replication and transcription preserves genome integrity. *PLoS Genet* 6: e1000810
- Sun L, Wu J, Du F, Chen X, Chen ZJ (2013) Cyclic GMP-AMP synthase is a cytosolic DNA sensor that activates the type I interferon pathway. *Science* 339: 786-791
- Sun T, Li Y, Yang W, Wu H, Li X, Huang Y, Zhou Y, Du Z (2019) Histone deacetylase inhibition up-regulates MHC class I to facilitate cytotoxic T lymphocyte-mediated tumor cell killing in glioma cells. *J Cancer* 10: 5638-5645
- van den Heuvel D, Spruijt CG, Gonzalez-Prieto R, Kragten A, Paulsen MT, Zhou D, Wu H, Apelt K, van der Weegen Y, Yang K *et al* (2021) A CSB-PAF1C axis restores processive transcription elongation after DNA damage repair. *Nat Commun* 12: 1342
- Van Oss SB, Cucinotta CE, Arndt KM (2017) Emerging Insights into the Roles of the Paf1 Complex in Gene Regulation. *Trends Biochem Sci* 42: 788-798
- Van Oss SB, Shirra MK, Bataille AR, Wier AD, Yen K, Vinayachandran V, Byeon IL, Cucinotta CE, Heroux A, Jeon J *et al* (2016) The Histone Modification Domain of Paf1 Complex Subunit Rtf1 Directly Stimulates H2B Ubiquitylation through an Interaction with Rad6. *Mol Cell* 64: 815-825
- Versteeg R, Noordermeer IA, Kruse-Wolters M, Ruiter DJ, Schrier PI (1988) c-myc down-regulates class I HLA expression in human melanomas. *EMBO J* 7: 1023-1029
- Vos SM, Farnung L, Boehning M, Wigge C, Linden A, Urlaub H, Cramer P (2018a) Structure of activated transcription complex Pol II-DSIF-PAF-SPT6. *Nature* 560: 607-612
- Vos SM, Farnung L, Linden A, Urlaub H, Cramer P (2020) Structure of complete Pol II-DSIF-PAF-SPT6 transcription complex reveals RTF1 allosteric activation. *Nat Struct Mol Biol* 27: 668-677
- Vos SM, Farnung L, Urlaub H, Cramer P (2018b) Structure of paused transcription complex Pol II-DSIF-NELF. *Nature* 560: 601-606
- Wang Q, Li M, Wu T, Zhan L, Li L, Chen M, Xie W, Xie Z, Hu E, Xu S *et al* (2022a) Exploring Epigenomic Datasets by ChIPseeker. *Curr Protoc* 2: e585

References

- Wang Z, Song A, Xu H, Hu S, Tao B, Peng L, Wang J, Li J, Yu J, Wang L *et al* (2022b) Coordinated regulation of RNA polymerase II pausing and elongation progression by PAF1. *Sci Adv* 8: eabm5504
- Woan KV, Lienlaf M, Perez-Villaroel P, Lee C, Cheng F, Knox T, Woods DM, Barrios K, Powers J, Sahakian E *et al* (2015) Targeting histone deacetylase 6 mediates a dual anti-melanoma effect: Enhanced antitumor immunity and impaired cell proliferation. *Mol Oncol* 9: 1447-1457
- Xie N, Shen G, Gao W, Huang Z, Huang C, Fu L (2023) Neoantigens: promising targets for cancer therapy. *Signal Transduct Target Ther* 8: 9
- Xie Z, Bailey A, Kuleshov MV, Clarke DJB, Evangelista JE, Jenkins SL, Lachmann A, Wojciechowicz ML, Kropiwnicki E, Jagodnik KM *et al* (2021) Gene Set Knowledge Discovery with Enrichr. *Curr Protoc* 1: e90
- Yan S, Michael WM (2009) TopBP1 and DNA polymerase alpha-mediated recruitment of the 9-1-1 complex to stalled replication forks: implications for a replication restart-based mechanism for ATR checkpoint activation. *Cell Cycle* 8: 2877-2884
- Yu M, Yang W, Ni T, Tang Z, Nakadai T, Zhu J, Roeder RG (2015) RNA polymerase II-associated factor 1 regulates the release and phosphorylation of paused RNA polymerase II. *Science* 350: 1383-1386
- Zatreanu D, Han Z, Mitter R, Tumini E, Williams H, Gregersen L, Dirac-Svejstrup AB, Roma S, Stewart A, Aguilera A *et al* (2019) Elongation Factor TFIIIS Prevents Transcription Stress and R-Loop Accumulation to Maintain Genome Stability. *Mol Cell* 76: 57-69 e59
- Zhang H, Christensen CL, Dries R, Oser MG, Deng J, Diskin B, Li F, Pan Y, Zhang X, Yin Y *et al* (2020) CDK7 Inhibition Potentiates Genome Instability Triggering Anti-tumor Immunity in Small Cell Lung Cancer. *Cancer Cell* 37: 37-54 e39
- Zhang Y, Liu T, Meyer CA, Eeckhoute J, Johnson DS, Bernstein BE, Nusbaum C, Myers RM, Brown M, Li W *et al* (2008) Model-based analysis of ChIP-Seq (MACS). *Genome Biol* 9: R137
- Zhu B, Mandal SS, Pham AD, Zheng Y, Erdjument-Bromage H, Batra SK, Tempst P, Reinberg D (2005) The human PAF complex coordinates transcription with events downstream of RNA synthesis. *Genes Dev* 19: 1668-1673

References

Zhu G, Pan C, Bei JX, Li B, Liang C, Xu Y, Fu X (2020) Mutant p53 in Cancer Progression and Targeted Therapies. *Front Oncol* 10: 595187

Ziv Y, Bielopolski D, Galanty Y, Lukas C, Taya Y, Schultz DC, Lukas J, Bekker-Jensen S, Bartek J, Shiloh Y (2006) Chromatin relaxation in response to DNA double-strand breaks is modulated by a novel ATM- and KAP-1 dependent pathway. *Nat Cell Biol* 8: 870-876

Zumer K, Maier KC, Farnung L, Jaeger MG, Rus P, Winter G, Cramer P (2021) Two distinct mechanisms of RNA polymerase II elongation stimulation in vivo. *Mol Cell* 81: 3096-3109 e3098

7 Appendix

7.1 Table of figures

Figure 1. 1: Mechanisms describing how MYCN prevents TRCs.....	14
Figure 1. 2: Protein domains of MYC and their canonical function.....	16
Figure 4. 1: MYC prevents DNA damage during S-phase.....	57
Figure 4. 2: MYC prevents transcription replication conflicts.....	59
Figure 4. 3: Scheme illustrating siRNA targets and their function.	60
Figure 4. 4: Example hits from the siRNA screen.....	61
Figure 4. 5: siRNA screen hits	63
Figure 4. 6: Validation of siRNA screen hits	65
Figure 4. 7: siRNA screen targeting PAF1c downstream factors.	67
Figure 4. 8: Effect of PAF1c depletion on MYC-dependent transcription.	68
Figure 4. 9: PAF1c is required for the transcription of long DNA repair genes.....	70
Figure 4. 10: PAF1c balances the transcriptional output of short and long genes.	72
Figure 4. 11: PAF1c and MYC repress the transcription of MHC class I genes.	74
Figure 4. 12: Characterization of chromatin occupancy of different elongation factors upon CTR9 depletion.....	76
Figure 4. 13: SPT6 recruitment to MHC class I genes is required for their expression upon CTR9 depletion.....	77
Figure 4. 14: Genome-wide analysis of SPT6 chromatin binding.....	79
Figure 4. 15: Effects of CTR9 depletion in several PDAC cell lines	81
Figure 4. 16: Effect of CTR9 depletion <i>in vivo</i>	83
Figure 4. 17: Characterization of DNA damage induction <i>in vivo</i> upon CTR9 depletion and ATR inhibition.	84

Appendix

Figure 4. 18: Inhibition of ATR does not potentiate the survival benefit of CTR9 or MYC depletion compared to control.	85
Figure 4. 19: Characterization of tumor immune cell infiltration upon CTR9 depletion..	86
Figure 4. 20: Characterization of CTR9 depletion effect in tumors grown in immunodeficient mice.	87
Figure 5. 1: Model summarizing the findings.	96

7.2 Summary of the siRNA screen

SIRNA	EDU INCORPORATION			NO ATRI			PLUS ATRI		
	Percent	Z-score	P-value	Percent	Z-score	P-value	Percent	Z-score	P-VALUE
<i>AQR</i>	1,305	-1,099	0,005	15,017	6,385	0,018	16,192	3,959	0,028
<i>ATM</i>	4,321	-0,171	0,065	0,315	-0,871	0,947	0,680	-0,746	0,906
<i>ATR</i>	13,464	2,641	0,524	8,504	3,171	0,011	22,601	5,902	0,010
<i>BCAS2</i>	6,742	0,573	0,134	0,605	-0,728	0,884	3,186	0,014	0,283
<i>BCLAF1</i>	6,275	0,430	0,373	0,696	-0,683	0,828	0,948	-0,664	0,894
<i>BRCA1</i>	4,030	-0,261	0,066	5,445	1,660	0,140	2,917	-0,068	0,414
<i>BRD3</i>	2,428	-0,754	0,012	0,946	-0,560	0,651	1,866	-0,386	0,686
<i>BRD4</i>	5,318	0,135	0,032	2,213	0,065	0,172	1,683	-0,442	0,677
<i>CDC73</i>	4,601	-0,085	0,016	3,424	0,663	0,037	12,379	2,802	0,013
<i>COPS3</i>	1,773	-0,955	0,003	5,556	1,715	0,155	2,731	-0,124	0,261
<i>CPSF1</i>	7,602	0,838	0,208	3,234	0,569	0,239	1,822	-0,399	0,685
<i>CPSF2</i>	5,081	0,062	0,018	4,723	1,304	0,019	3,150	0,003	0,170
<i>CPSF3</i>	11,285	1,971	0,457	1,173	-0,448	0,465	3,806	0,202	0,233
<i>CPSF4</i>	6,551	0,514	0,055	0,600	-0,731	0,886	2,743	-0,120	0,270
<i>CPSF6</i>	7,102	0,684	0,323	0,920	-0,573	0,612	1,626	-0,459	0,669
<i>CPSF7</i>	8,937	1,249	0,539	1,493	-0,290	0,349	1,696	-0,438	0,749
<i>CSTF1</i>	10,434	1,709	0,541	1,036	-0,516	0,541	2,410	-0,221	0,464
<i>CSTF2</i>	17,999	4,036	0,073	0,613	-0,724	0,884	1,871	-0,385	0,623
<i>CSTF3</i>	11,083	1,909	0,452	0,821	-0,622	0,695	2,687	-0,137	0,285
<i>CTR9</i>	3,997	-0,271	0,015	1,258	-0,406	0,353	4,520	0,419	0,073
<i>DCP1A</i>	3,111	-0,544	0,007	1,100	-0,484	0,507	3,276	0,041	0,306
<i>DCP2</i>	4,459	-0,129	0,013	0,506	-0,777	0,913	0,863	-0,690	0,892
<i>DDX23</i>	4,982	0,032	0,025	1,757	-0,160	0,338	2,950	-0,057	0,264
<i>DHX16</i>	2,533	-0,721	0,005	2,378	0,147	0,234	1,347	-0,543	0,837
<i>DIS3</i>	1,119	-1,156	0,005	1,438	-0,317	0,317	1,334	-0,547	0,839
<i>DROSHA</i>	3,097	-0,548	0,022	2,597	0,255	0,108	1,100	-0,618	0,859
<i>EDC3</i>	1,310	-1,098	0,008	1,378	-0,347	0,330	1,864	-0,387	0,663
<i>EDC4</i>	4,578	-0,092	0,013	1,968	-0,056	0,234	1,064	-0,629	0,863
<i>EFTUD2</i>	1,909	-0,913	0,003	3,000	0,454	0,023	5,336	0,666	0,032
<i>ELF3</i>	3,871	-0,310	0,123	1,110	-0,479	0,503	2,947	-0,058	0,203
<i>ELL</i>	6,105	0,377	0,366	0,885	-0,590	0,682	2,149	-0,300	0,526

Appendix

EXOSC1	3,970	-0,279	0,038	1,783	-0,147	0,222	1,679	-0,443	0,755
EXOSC10	0,567	-1,326	0,009	0,584	-0,739	0,864	1,707	-0,434	0,654
EXOSC2	3,111	-0,544	0,005	1,952	-0,064	0,295	0,886	-0,683	0,877
EXOSC3	0,686	-1,289	0,007	1,033	-0,517	0,562	1,809	-0,403	0,708
EXOSC4	2,691	-0,673	0,005	1,184	-0,443	0,431	2,341	-0,242	0,470
EXOSC5	1,139	-1,150	0,002	2,055	-0,013	0,036	2,626	-0,156	0,396
EXOSC7	3,062	-0,559	0,005	1,155	-0,457	0,463	1,283	-0,563	0,843
EXOSC8	1,044	-1,179	0,003	2,445	0,180	0,127	1,835	-0,395	0,699
EXOSC9	4,083	-0,245	0,010	1,279	-0,396	0,345	1,511	-0,494	0,668
FIP1L1	13,052	2,514	0,277	1,879	-0,099	0,161	4,589	0,440	0,239
GTF2F1	1,691	-0,980	0,003	0,765	-0,649	0,800	1,321	-0,551	0,837
LEO1	4,031	-0,261	0,021	2,443	0,179	0,171	4,880	0,528	0,198
NCBP1	2,872	-0,617	0,005	1,420	-0,326	0,352	1,520	-0,491	0,794
NONO	5,632	0,232	0,063	0,852	-0,606	0,707	2,335	-0,244	0,466
NTC 1	10,717	1,796	0,419	1,066	-0,501	0,540	2,081	-0,321	0,561
NTC 2	8,887	1,233	0,731	1,442	-0,315	0,355	1,778	-0,413	0,548
NTC 3	9,305	1,362	0,882	0,835	-0,615	0,700	2,828	-0,094	0,335
NUDT21	5,811	0,287	0,175	0,623	-0,719	0,880	1,787	-0,410	0,689
PAF1	2,077	-0,862	0,010	1,239	-0,415	0,388	3,988	0,257	0,272
PAPOLA	7,066	0,673	0,108	5,675	1,774	0,217	7,104	1,202	0,247
PCF11	2,304	-0,792	0,005	5,633	1,753	0,016	6,955	1,157	0,053
POLR2M	9,709	1,486	0,952	0,811	-0,627	0,697	1,921	-0,369	0,612
PRMT5	2,851	-0,624	0,007	2,308	0,112	0,190	1,606	-0,465	0,776
PTBP1	1,085	-1,167	0,005	1,351	-0,360	0,371	3,177	0,011	0,194
RAD50	3,875	-0,309	0,011	1,487	-0,293	0,259	2,729	-0,125	0,380
RBFOX2	1,802	-0,946	0,003	1,377	-0,347	0,353	2,201	-0,284	0,506
RBM7	7,505	0,808	0,482	1,575	-0,249	0,241	0,752	-0,724	0,889
RECQL5	3,848	-0,317	0,038	0,943	-0,562	0,674	1,198	-0,589	0,863
RPAP2	6,538	0,511	0,053	0,826	-0,619	0,771	1,070	-0,628	0,876
RPRD1B	3,739	-0,351	0,013	1,266	-0,402	0,395	1,365	-0,538	0,821
RTF1	4,286	-0,182	0,096	3,379	0,641	0,016	11,526	2,543	0,147
SETD2	5,746	0,267	0,046	3,800	0,848	0,259	2,270	-0,264	0,490
SETX	9,399	1,390	0,953	1,019	-0,524	0,568	2,724	-0,126	0,429
SFPQ	5,924	0,322	0,037	1,130	-0,469	0,485	3,799	0,200	0,081
SMN1	2,401	-0,762	0,004	1,594	-0,240	0,287	1,269	-0,567	0,850
SNRNP70	3,409	-0,452	0,007	1,347	-0,362	0,380	2,967	-0,052	0,393
SNRPE	3,741	-0,350	0,017	3,975	0,935	0,122	5,040	0,576	0,267

Appendix

SRSF1	1,662	-0,989	0,011	2,625	0,269	0,236	2,417	-0,219	0,421
SSU72	7,821	0,905	0,410	1,349	-0,361	0,305	1,694	-0,438	0,747
SUPT6	1,786	-0,951	0,004	4,172	1,032	0,024	3,250	0,034	0,243
SYMPK	5,993	0,343	0,049	2,086	0,003	0,166	8,642	1,669	0,157
TCEA1	1,344	-1,087	0,008	3,328	0,616	0,245	1,546	-0,483	0,766
TCEA2	4,246	-0,195	0,028	1,479	-0,297	0,333	2,433	-0,214	0,397
TCEA3	5,764	0,272	0,231	1,845	-0,116	0,313	1,179	-0,594	0,864
TCEAL1	6,237	0,418	0,147	0,640	-0,711	0,874	1,684	-0,441	0,752
TCERG1	2,826	-0,631	0,005	1,988	-0,046	0,260	2,064	-0,326	0,552
THOC1	4,917	0,012	0,024	0,982	-0,542	0,582	1,804	-0,405	0,702
THOC2	5,558	0,209	0,145	0,960	-0,553	0,641	2,271	-0,263	0,493
TTF2	5,311	0,133	0,037	1,552	-0,261	0,341	1,741	-0,424	0,625
TUT1	2,950	-0,593	0,010	1,141	-0,464	0,474	2,582	-0,169	0,318
U2AF1	2,608	-0,698	0,006	3,832	0,865	0,053	5,446	0,700	0,229
U2AF2	1,670	-0,987	0,003	0,895	-0,585	0,722	1,153	-0,602	0,869
WDR33	8,652	1,161	0,430	2,436	0,176	0,123	7,801	1,414	0,047
WDR61	2,250	-0,808	0,004	0,898	-0,584	0,725	1,966	-0,356	0,586
XAB2	2,055	-0,868	0,006	5,668	1,771	0,047	6,697	1,079	0,204
XRN1	7,002	0,653	0,111	2,136	0,027	0,295	1,392	-0,530	0,828
XRN2	2,401	-0,762	0,035	2,104	0,012	0,264	2,411	-0,221	0,459
ZMYND11	4,070	-0,249	0,013	0,815	-0,625	0,742	1,019	-0,643	0,865

7.3 Acknowledgement

I would like to thank my mentor and primary supervisor, Prof. Dr. Martin Eilers for giving me this wonderful opportunity to do my Ph.D. in his laboratory. His faith and trust in me from the very first days gave me not only confidence but also endless motivation to do my best.

I would also like to thank my thesis committee members Prof. Dr. Stefan Gaubatz and Prof. Dr. Martin Sos for their time, valuable advice and support that I needed to go through my PhD project.

Special thanks go to Dr. Anneli Gebhardt-Wolf for performing all the *in vivo* experiments described in my thesis. Her key contributions have given this project an important therapeutic relevance and have greatly increased the impact of these findings.

In the new office, right next to the kitchen, I found wonderful colleagues to talk to, share ups and downs and get advice from, thanks to my office mates Markus Dehmer, Raphael Vidal and Stefanie Ha.

Thanks to Dr. Bastian Krenz for not only guiding me in the lab during the early days of my master's thesis, but also for always being open to discuss science, even during his typical large-scale experiments.

Thanks to Dr. Steffi Herold and Dr. Giacomo Cossa for taking the time and effort to proofread this thesis and for giving advice on how to improve it.

Finally, I would like to thank my family. My wife Noha, who has always supported me and provided the perfect environment for me to do my best. It wouldn't have been easy to be a father while doing my Ph.D. without a wonderful wife like you. Thanks to my children Mohammad and Nora, even if you don't know it yet, you have given me a lot of motivation to do my best in my work. None of this would have been possible without the unconditional love and support in all forms from my beloved mother, father and two brothers.

7.4 Publications

Gaballa, A.*, Gebhardt-Wolf, A.*, Krenz, B., Andreani, S., Schülein-Völk, C., Kastner, C., Ade, C., Gallant, P., Rosenfeldt, M., Eilers, M. Competition for transcription elongation factors links MYC-dependent S-phase progression to immune evasion in pancreatic carcinoma, *Manuscript under consideration* (*Authors contributed equally).

Solvie, D., Baluapuri, A., Uhl, L., Fleischhauer, D., Endres, T., Papadopoulos, D., Aziba, A., **Gaballa, A.**, Mikicic, I., Isaakova, E., Giansanti, C., Jansen, J., Jungblut, M., Klein, T., Schulein-Volk, C., Maric, H., Doose, S., Sauer, M., Beli, P., . . . Eilers, M. (2022). MYC multimers shield stalled replication forks from RNA polymerase. *Nature*, 612(7938), 148-155.

Papadopoulos, D., Solvie, D., Baluapuri, A., Endres, T., Ha, S. A., Herold, S., Kalb, J., Giansanti, C., Schulein-Volk, C., Ade, C. P., Schneider, C., **Gaballa, A.**, Vos, S., Fischer, U., Dobbstein, M., Wolf, E., & Eilers, M. (2022). MYCN recruits the nuclear exosome complex to RNA polymerase II to prevent transcription-replication conflicts. *Mol Cell*, 82(1), 159-176 e112.

Krenz, B., Gebhardt-Wolf, A., Ade, C. P., **Gaballa, A.**, Roehrig, F., Vendelova, E., Baluapuri, A., Eilers, U., Gallant, P., D'Artista, L., Wiegering, A., Gasteiger, G., Rosenfeldt, M. T., Bauer, S., Zender, L., Wolf, E., & Eilers, M. (2021). MYC- and MIZ1-Dependent Vesicular Transport of Double-Strand RNA Controls Immune Evasion in Pancreatic Ductal Adenocarcinoma. *Cancer Res*, 81(16), 4242-4256.

7.5 Affidavit

I hereby confirm that my thesis entitled: “PAF1c drives MYC-mediated immune evasion in pancreatic ductal adenocarcinoma” is the result of my own work. I did not receive any help or support from commercial consultants. All sources and/or materials are listed and specified in the thesis.

Furthermore, I confirm that this thesis has not yet been submitted as part of another examination process neither in identical nor in similar form.

Place, Date

Eidesstattliche Erklärung

Hiermit erkläre ich an Eides statt, die Dissertation: “ PAF1c treibt die MYC-vermittelte Immunevasion im duktalem Adenokarzinom der Bauchspeicheldrüse an” eigenständig, d.h. insbesondere selbständig und ohne Hilfe eines kommerziellen Promotionsberaters, angefertigt und keine anderen als die von mir angegebenen Quellen und Hilfsmittel verwendet zu haben.

Ich erkläre außerdem, dass die Dissertation weder in gleicher noch in ähnlicher Form bereits in einem anderen Prüfungsverfahren vorgelegen hat.

Ort, Datum

7.6 Curriculum vitae